University of Central Florida
STARS

Electronic Theses and Dissertations | Doctoral Dissertation (Open Access)

Nanoscale Spectroscopy in Energy and Catalytic Applications

2019

Yi Ding
University of Central Florida

Find similar works at: https://stars.library.ucf.edu/etd

University of Central Florida Libraries http://library.ucf.edu

Part of the Engineering Science and Materials Commons

STARS Citation

Ding, Yi, "Nanoscale Spectroscopy in Energy and Catalytic Applications" (2019). *Electronic Theses and Dissertations*. 6603.
https://stars.library.ucf.edu/etd/6603

This Doctoral Dissertation (Open Access) is brought to you for free and open access by STARS. It has been accepted for inclusion in Electronic Theses and Dissertations by an authorized administrator of STARS. For more information, please contact lee.dotson@ucf.edu.

University of Central Florida
STARS
Showcase of Text, Archives, Research & Scholarship

NANOSCALE SPECTROSCOPY IN ENERGY AND CATALYTIC APPLICATIONS

by

YI DING
M.S Loughborough University, 2012
B.E Northwestern Polytechnical University, 2011

A dissertation submitted in partial fulfillment of the requirements
for the degree of Doctor of Philosophy
in the Department of Materials Science and Engineering
in the College of Engineering and Computer Science
at the University of Central Florida
Orlando, Florida

Fall Term
2018

Major Professor: Laurene Tetard

© 2018 Yi Ding

ABSTRACT

Emerging societal challenges such as the need for more sustainable energy and catalysis are requiring more sensitive and versatile measurements at the nanoscale. This is the case in the design and optimization of new materials for energy harvesting (solar cells) and energy storage devices (batteries and capacitors), or for the development of new catalysts for carbon sequestration or other reactions of interest. Hence, the ability to advance spectroscopy with nanoscale spatial resolution and high sensitivity holds great promises to meet the demands of deeper fundamental understanding to boost the development and deployment of nano-based devices for real applications.

In this dissertation, the impact of nanoscale characterization on energy-related and catalytic materials is considered. Firstly an introduction of the current energy and environmental challenges and our motivations are presented. We discuss how revealing nanoscale properties of solar cell active layers and supercapacitor electrodes can greatly benefit the performance of devices, and ponder on the advantages over conventional characterization techniques.

Next, we focus on two dimensional materials as promising alternative catalysts to replace conventional noble metals for carbon sequestration and its conversion to added-value products. Defect-laden hexagonal boron nitride (*h*-BN) has been identified as a good catalyst candidate for carbon sequestration. Theoretically, defects exhibit favorable properties as reaction sites. However, the detailed mechanism pathways cannot be readily probed experimentally, due to the lack of tools with sufficient sensitivity and time resolution.

A comprehensive study of the design and material processes used to introduce defects in *h*-BN in view of improving the catalytic properties is presented. The processing-structure-property

relationships are investigated using a combination of conventional characterization and advanced nanoscale techniques. In addition to identifying favorable conditions for defect creation, we also report on the first signs of local reactions at defect sites obtained with nanoscale spectroscopy. Next, we explore avenues to improve the sensitivity and time-resolution of nanoscale measurements using light-assisted AFM-based nanomechanical spectroscopy. For each configuration, we evaluate the new system by comparing its performance to the commercial capabilities.

Lastly, we provide a perspective on the opportunities for state-of-the-art characterization to impact the fields of catalysis and sustainable energy, as well as the urge for highly sensitive functional capabilities and time-resolution for nanoscale studies.

to my beloved Winston, my parents and my grandparents

ACKNOWLEDGMENTS

There are many people that deserve my sincere gratitude for their contribution to my growth at UCF. I would like to thank those people, without whom this dissertation would not be possible.

First and foremost, I would like to thank my advisor, Dr. Laurene Tetard, for being tremendous mentor for me throughout my entire journey to pursue this degree. Dr. Laurene Tetard has spent endless time and energy in teaching me the detailed fundamentals of conducting scientific research. Under her guidance, I gradually learned how to address a scientific question in a constructive way and grow as a good researcher and life-long learner. Thank you, Laurene, for being the female version of “Driss” and your “intouchable” kindness to all of people live around you. You have inspired to become another Driss who really cares and respects others. Thank you, Laurene, for being my family member here in the USA and constantly provide support to me from all aspects that I can think of. I thank all the non-linear interactions I have had with you that have polished me to be better myself.

I would also like to thank my committee members, Dr. Suryanarayana Challapalli, Dr. Lei Zhai, Dr. Richard Blair Dr. Jayan Thomas and Dr. Arkadiy Lyakh. Thank you for the encouragement, the support, time and attention. I would like to express my deep gratitude to Dr. Suryanarayana Challapalli for the inspiration that I received from him to be a serious researcher. I also thank Dr. Michael Molinari for his good advices and kind help in my research. I also would like to thank our collaborator Dr. Talat S. Rahman. I also want to thank Dr. Anton Ievlev from Oak Ridge National Laboratory. I would also like to thank Dr. Anirban Roy for all the kind help, advices and interesting conversations.

I am so grateful to Dr. Mikhael Soliman, who has been my brother to me and support me during happy and difficult times throughout these years. I also want to thank my colleagues and friends: Chao Li, Karima Lasri, Raphael Coste, Fernand Torres, Chance Barrett, Briana Lee, Ahmad Khater, David Nash, Katerina Chagoya, Tianyu Zheng, Hao Chen and Caicai Zhang.

I would like to thank my husband for your love, support and patience that keep me strong even during the frustrating times of the study. I am blessed to have you as my friend and my partner.

I am truly indebted to my parents and my grandparents whose love constantly supports me and I could not have done without their love.

Last but not least, I give thanks to the almighty God for choosing me as your loved daughter and for loving me.

TABLE OF CONTENTS

LIST OF FIGURES xi
LIST OF TABLES xv
1 INTRODUCTION 1
1.1 Motivations 1
1.2 Outline of the Present Work 3
2 NANOSCALE IMAGING AND SPECTROSCOPY IN ENERGY APPLICATIONS 5
2.1 Background 5
2.2 Methods 8
2.2.1 Background and Motivation 8
2.2.2 Methods 15
2.2.3 Results and Discussion 19
2.2.4 Conclusions 26
2.3 Nanoscale Imaging and Spectroscopy for Energy Storage Materials 27
2.3.1 Background and Motivation 27
2.3.2 Methods 30
2.3.3 Results and Discussion 34
2.4 Conclusions 37
2.5 Summary and Future Perspectives 37
3 SPECTROSCOPY IN CATALYSIS DEVELOPMENT 40
3.1 Background 40
3.1.1 Better catalyst 41
3.1.2 h-BN as heterogeneous catalyst 41
3.2 Motivation 44
3.3 Case Study One: Defect engineering in h-BN powder samples and subsequent property characterization for catalytic applications 45
3.3.1 Methods 46
3.3.2 Results and Discussion 50
3.3.3 Conclusions 61
3.4 Case Study Two: Study the effect of different ball milling on the effectiveness of defect creation for CO_2 gas molecule uptake 62

3.4.1 Background and Motivation 62
3.4.2 Methods 63
3.4.3 Results and Discussion 65
3.4.4 Conclusions 69
3.5 Case Study Three: Study of oxygen uptake on defect-laden hexagonal boron nitride through time-dependent fluorescence spectroscopy measurement 69
3.5.1 Background and Motivation 69
3.5.2 Methods 71
3.5.3 Results and Discussion 72
3.5.4 Conclusions 82
3.6 Summary and Future Perspectives 83
4 NANOSCALE SPECTROSCOPY FOR CATALYSIS APPLICATIONS 85
4.1 Background and Motivation 85
4.2 Case Study One: Heat treatment-assisted defect engineering in h-BN flake samples and subsequent property characterization for catalytic applications 88
4.2.1 Background and Motivation 88
4.2.2 Methods 89
4.2.3 Results and Discussion 95
4.2.4 Conclusions 106
4.3 Case Study Two: Laser-assisted defect engineering in *h*-BN flake samples and subsequent property characterization for catalytic applications 107
4.3.1 Background and Motivation 107
4.3.2 Methods 108
4.3.3 Results and Discussion 110
4.3.4 Conclusions 116
4.4 Summary and Future Perspectives 116
5 ADDING TO EXISTING AFM MODULES FOR ENERGY AND CATALYTIC STUDIES 118
5.1 Background 118
5.2 The development of light-assisted AFM-based nanomechanical spectroscopy with a case study of light-matter interaction of nanoparticles 119
5.2.1 Background and Motivation 119
5.2.2 Methods 122

5.2.3 Results and Discussion 124
5.2.4 Conclusions 135
5.3 Multifrequency AFM and its combination with NanoIR spectroscopy 135
5.3.1 Background and Motivation 135
5.3.2 Methods 137
5.3.3 Results and Discussion 138
5.3.4 Conclusions 143
5.4 Summary and Future Perspectives 143
6 CONCLUSION 145
6.1 Summary and Future Perspectives 145
APPENDIX A: BACKGROUND FOR AFM, FORCE CURVE MEASUREMENT AND PFM 147
APPENDIX B: BACKGROUND FOR MODE SYNTHESIZING AFM (MSAFM) 152
APPENDIX C: COPYRIGHT PERSIMISSIONS FOR FIGURE 2-5, 2-6 155
APPENDIX D: COPYRIGHT PERMISSION FOR FIGURE 3-1 157
APPENDIX E: COPYRIGHT PERMISSION FOR FIGURE 4-9 159
LIST OF REFERENCES 161

LIST OF FIGURES

Figure 1–1 Summary of the potential relationships between intrinsic properties of nanomaterials on their catalytic activity. 2
Figure 2–1 Schematic illustration of basic working principle of an atomic force microscope (AFM) representing the cantilever engaged with the sample surface, the laser read-out laser system to the detector, and the feedback controls to control the piezo for X-Y-Z motion during imaging. 6
Figure 2–2 Schematic illustration of the key nanoscale processes that determine the performance of the BHJ solar cells. BHJ from (a) bulk to (b) nano to (c) charge carrier transfers illustrated with the energy levels of the hole transport layer (gray), HOMO and LUMO of the electron donor (red) and electron acceptor (pink), and electron transport layer (blue). 12
Figure 2–3 (a) Chemical structure of PTB7 and ICBA used as electron donor and acceptor, respectively; (b) Representative energy-level diagram of the fabricated device, including electrode materials (Ir and ITO) and electron donor (PTB7) and acceptor (ICBA). 15
Figure 2–4 Schematic diagram of top illumination configuration for local current spectroscopy with pc-AFM. 18
Figure 2–5 Various imaging modes of the active layer. (a) Height image (b) Tapping mode amplitude AFM image (c) Tapping mode phase AFM image (d) MSAFM amplitude image. Image size for all AFM images is 2×1 μm [31]. 20
Figure 2–6 Nanoscale characterization of PTB7:ICBA blend films prepared by binary (a-c) and ternary (d-f) mixture of solvents. (a,d) AFM adhesion maps extracted from PFM measurements; (b, e) correlative cluster analysis maps for AFM adhesion maps with ICBA and PTB7 domain identified; (c, f) MSAFM maps. Image size for all AFM images are 2×2 μm [31]. 21
Figure 2–7 Dark and photocurrent densities measured by pc-AFM (DC bias at -4V) for PSCs with active layers prepared with binary (a, c) and ternary solvents (b, d). Inset images on (a) and (b) are the morphology images showing the regions where the respective histograms of current values are extracted. Figure 2-7 (c and d) show the line profiles of the current change across the sample as a result of white light illumination (red curves) [31]. 23
Figure 2–8 Dark current responses (a) averaged I-V curve, current mapping at bias (b) 1.5 V (c) 3.0 V and (d) 4.5 V (Scan Size: 500 nm) 24
Figure 2–9 Photo-current responses (a) averaged I-V curve, current mapping at bias (b) 1.5 V (c) 3.0 V and (d) 4.5 V (Scan Size: 500 nm) 25
Figure 2–10 Schematic illustration of the fabrication process [62] 31
Figure 2–11 Schematic of Kelvin probe force microscopy [64] 33
Figure 2–12 AFM topography of the WO_3/WS_2 electrode before (a, c) and after cycling (b, d). (e,f) KPFM maps of the same region presented in (c, d). The average V_{CPD} is indicated on each image. 35
Figure 2–13 AFM morphology (a) and V_{CPD} values measured by KPFM (b) for RGO before cycling. (c, d) corresponding AFM morphology (c) and KPFM (d) after cycling. (e) Histogram of measured V_{CPD} values for RGO before and after cycling 36
Figure 3–1 CO_2 hydrogenation process with an example of added value by-products formation [67] 41
Figure 3–2 (a) Illustration of formation of *dh*-BN from pristine *h*-BN through ball milling, (b) SEM image of pristine *h*-BN flakes, (c-j) SEM image of *dh*-BN flakes after ball milling with ZrO_2 balls for 30 min (c, d), 60 min (e, f), 90 min (g, h), and 120 min (i, j). The SEM images presented in the right column correspond to a zoom of the images in the left column. 50

Figure 3–3 Zoomed in XRD spectra of pristine *h*-BN (black) and ball milled *dh*-BN (red) powders. The inset provides the XRD spectra with the 2θ ranging from 10 to 90°.....52
Figure 3–4 (a) Raman spectra exhibiting the E_{2g} band ~1370 cm^{-1} of pristine *h*-BN (purple in inset) and *dh*-BN after ball milling with ZrO_2 for 30 min (red), 60 min (orange), 90 min (blue), 120 min (green). (b) Table summarizing the position and FWHM of the E_{2g} band in ball-milled *h*-BN obtained with different durations of treatments with ZrO_2 milling balls.....53
Figure 3–5 (a) FTIR spectra of *h*-BN and *dh*-BN obtained for milling times of 30 min, 60 min, 90 min, and 120 min with ZrO_2. (b) Evolution of E_{1u} (top, black) and A_{2u} (bottom, red) IR bands as a function of milling duration. (c) FTIR spectra of *h*-BN and *dh*-BN obtained after ball milling for 120 min with ZrO_2 (green) milling balls.....54
Figure 3–6 Averaged mass spectra extracted from ball milled dh-BN before (black) and after (red) CO_2 gas molecule update.....57
Figure 3–7 Effect of heat treatment on *h*-BN powders (a) FTIR spectra of BN powders heat treated at different conditions: 800˚C for 2 h (red), 850˚C for 2 h (orange), 850˚C for 12 h (green), 850˚C for 24 h (light green), 900˚C for 2 h (blue), 900˚C for 12 h (brown), 900˚C for 24 h (purple), 950˚C for 2 h (pink), (b) Corresponding Raman spectra representing the E_{2g} mode Raman peak of the heat treated BN powders (c) Raman band corresponding to the B-O bond for oxidized BN powder around 885 cm^{-1}.....58
Figure 3–8 FTIR spectra of ball-milled BN powders before (black) and after pressurization for 48 h under 40 PSI (red) in CO_2 (a) and in propene (b). Insets provide details of the IR bands in the 1500-4000 cm^{-1} region. 60
Figure 3–9 Representation of pristine *h*-BN and various *dh*-BN exhibiting color changes after ball milling with different milling parameters.....65
Figure 3–10 XRF results for *dh*-BN milled by milling balls made of ZrO_2 (red), stainless steel (black) and WC.....65
Figure 3–11 SEM image of *dh*-BN flakes milled for 2 h with milling with bearing of (a-f) ZrO_2; (g-l) stainless steel; (m-r) WC. The bearing diameters are listed on the left. The SEM images presented in the right column correspond to a zoom of the images in the left column.....68
Figure 3–12 Schematic illustration of intra-band energy level addition in *h*-BN bandgap via (a) defect free intrinsic *h*-BN (b) defect laden *h*-BN with impurities or molecules reacting on the defects, exhibiting additional energy levels in the band gap.....72
Figure 3–13 Fluorescence intensity for pristine *h*-BN flakes with corresponding peak deconvolution using 8 Gaussian fits selected based on literature assignments.....73
Figure 3–14 Evolution of the fluorescence intensity spectra for ball milled dh-BN from first exposure to air up to 4320 min (3 days) exposure to air. 75
Figure 3–15 Time dependent fluorescence intensity for the 8 peaks fitted by Gaussian for ball milled *dh*-BN powder.....75
Figure 3–16 (a) Raman spectra for *dh*-BN before and after propene molecule uptake (b) FTIR spectra for *dh*-BN with propene molecule uptake 78
Figure 3–17 Evolution of the emitted fluorescence intensity of ball milled *dh*-BN with propene uptake after exposure to air for 3 days.....80
Figure 3–18 Evolution of the fluorescence intensity for *dh*-BN powder exposed to propene (blue color) and without exposure to propene (red color). The effect of exposure to air on the fluorescence intensity was monitored for 3 days.....80
Figure 3–19 FTIR spectra of *dh*-BN powder with propene uptake before air exposure (blue), *dh*-BN powder with propene uptake after several weeks of exposure to air (pink), and *dh*-BN after several weeks of exposure to air (red).....82

Figure 4–1 Schematic of PFM force-distance curve showing how stiffness and adhesion properties are extracted [165] 91
Figure 4–2 Schematic of LCR[166] 92
Figure 4–3 Schematic of electrostatic force microscopy [168] 93
Figure 4–4 AFM morphology image of BN flake (a) before heat treatment and (c,e) after heat treatment; (b,d,f) cross section profiles for lines indicated in (a,(c,e), respectively; (g) single Raman spectra for BN flake before and after heat treatment; (h) TEM image of wrinkle cross-section with a schematic illustration of heat treatment and subsequent quenching for wrinkle formation; (i) peaks extracted from ToF-SIMS spectra 96
Figure 4–5 Nanoscale functional imaging to of heated-treated h-BN (a) AFM morphology and corresponding (b) EFM phase image with +3V tip bias, (c) EFM phase image with -3V tip bias 98
Figure 4–6 (a) AFM morphology and corresponding (b) KPFM image 100
Figure 4–7Nanoscale mechanical imaging of heat-treated h-BN (a) AFM morpology of BN flake (b) LCR spectra for point selected from different regions (c) LCR frequency mapping (d) Kelvin–Voigt mechanical equivalent model for LCR 102
Figure 4–8 Crystal structure of (a) graphite and (b) MoS_2; (c) and (d) AFM morphology image for heat treated few layer graphite flakes; (e) Optical images for MoS_2 flakes before (upper) and after (lower) heat treatment; (f) AFM image for heat treated MoS_2 flakes; (g) Raman spectra of heat treated HOPG flake (h) PL spectra for heat treated MoS_2; (i) D band and (j) G band Raman mapping for heat treated HOPG flakes; (k) PL intensity and (l) PL position maps for heat treated MoS_2 flakes 104
Figure 4–9 Schematic of the AFM-IR configuration on the NanoIR2 platform[198] 109
Figure 4–10 (a) AFM topography image of two exfoliated h-BN flakes with different thicknesses; (b) An NanoIR spectrum from center region on pristine h-BN flake with the single point indicated by the black cross in (a); c) Nano IR amplitude image recorded at 1365 cm-1; (d) Four NanoIR spectra obtained from edge region on pristine h-BN flakes, their positions are indicated by the red crossed in (b); (e) NanoIR spectra obtained from SiO_2 substrate 110
Figure 4–11 Laser-induced defect formation on *h*-BN flake. (a) AFM topography image of *h*-BN flake surface after laser induced defect creation (b-h) NanoIR amplitude maps obtained at wavenumbers; (i) NanoIR spectra acquired with laser power 3.97% (red), 2.36% (orange), 1.91% (yellow), 1.84% (green), 1.1% (blue), 0.99% (wine); (j) Frequency spectra acquired after laser was on for 30 sec at laser power 3.97% and 7.52%; (k) NanoIR spectra from flat region, edge region, wrinkle region and laser-induced defect region. 113
Figure 4–12 Reactions over laser induced defect sites. (a) AFM topography image of BN flake with laser induced defect sites; (b-f) NanoIR amplitude maps obtained at different wavenumbers; (g) Time-dependent NanoIR spectra acquired from the same position; (f) Contact resonant frequency of the AFM cantilever showing the frequency shift 115
Figure 5–1(a) Custom AFM platform for photo-induced nanoscale measurement with 532 nm laser illumination, (b) UV-Vis absorption spectra of Au nanoislands annealed at 473 K (black), 573 K (red) and 673 K (blue), (c) AFM topography image of the nanoislands annealed at 673 K. 124
Figure 5–2 Photothermal expansion of the nanoislands detected in contact mode. (a,b) Deflection map with laser off (a) and on (b). (c) Deflection profile of the nanoislands indicated by the light blue mark in (a) and (b). (d) Histogram representing the deflection measured across the image with laser off (black) and on (red). 125
Figure 5–3 3D representation of Au nanoislands topography for laser off (a, c) and on (b, d). The area at the center in (a) and (b) corresponds to the Au islands with the largest photothermal expansion. (c) and (d)

show the respective high resolution morphology in (a) and (b) with selected height contours. (e) and (f) are the profiles for the two selected contours with laser off (black) and laser on (red). 127
Figure 5–4 Photo-induced change in mechanical property measured with PFM. (a) PFM platform customized for photo-induced laser at 532 nm. Standard PFM force curve is depicted. (b, c) represent the maps reconstructed by calculating the slope of the PFM curve at each point of the image, with laser is off (b) and on (c). (d) PFM profiles extracted from maps in (a) and (b), respectively. (e) Histogram of the stiffness distribution for laser off (black) and on (red) 129
Figure 5–5 Laser power-dependent PFM measurements on Au. (a) Slope of the approach curve measured with PFM at increasing laser power. (b) First-derivative of the curves presented in (a). (c) Temperature dependent stiffness of glass substrate (black) and Au (red). 131
Figure 5–6 Liquid skin melting mechanism model illustrating the temperature dependent softening of Au nanoparticles shell at $T_1<T_m$ before complete melting of the structures at or above T_m. 133
Figure 5–7 Nanoscale thermal analysis of Au nanostructure softening. (a) AFM height image of Au nanoparticles deposited on glass substrate. (b) Deflection vs temperature plots at positions marked in (a). 134
Figure 5–8 Schematic of one configuration of multi-frequency AFM, called mode-synthesizing AFM principles [234]. By applying multiple excitations to the tip-sample system, it is possible to synthesize new modes (difference and sum frequencies) operational for imaging and spectroscopy measurements. These are yet to be fully evaluated to determine the benefits and limitations of the approach. 136
Figure 5–9 MSAFM with two mechanical actuations. (left) topography of the xx calibration sample, (center) traditional LCR amplitude map indicating a change in mechanical properties in the two regions, (right) MSAFM map obtained at f_p = 100 kHz, f_s = 305 kHz and monitoring the sum mode at 100 + 305 = 405 kHz. LCR and MSAFM images are amplitude images. 139
Figure 5–10 MSAFM with one mechanical actuation on the sample and one photothermal actuation on the tip using the infrared QCL laser. (Top) waterfall display of the frequency spectra generated over time as the driving frequency of the sample (f_s) is spanned from 200 kHz to 170 kHz. The laser excitation (f_p) was fixed at 178.76 kHz. (Bottom) frequency spectra of the tip-sample system for selected sample frequencies, f_p-f_s = +4 kHz, f_p-f_s = +0.3 kHz, f_p-f_s = 0 kHz, f_p-f_s = -2 kHz, f_p-f_s = -4 kHz, and f_p-f_s = -9 kHz. 142
Figure 5–11MSAFM images at two different f_p resulting from one mechanical actuation on the sample and one photothermal actuation on the tip using the infrared QCL laser, and comparison to the conventional NanoIR map. (top) f_p is very close to f_s (bottom) f_p is larger than f_s. 143

LIST OF TABLES

Table 2-1 Photovoltaic results of PSCs with active layers prepared by different solvents 19
Table 3-1 Summary of the flake size distribution percentage for the different ball-milled *dh*-BN powders 51
Table 3-2 Absorption (A_{2u})/ Absorption (E_{1u}) ratio in the IR spectrum of pristine *h*-BN and ball milled *dh*-BN 55
Table 3-3 Summary of the position and FWHM of the E_{2g} band in heat treated *dh*-BN 58
Table 3-4 Ball milling parameters including milling media, milling time, ball size, number of ball used, and resulting mass uptake in propene. 63
Table 3-5 Averaged FWHM values of BN E_{2g} mode Raman peak for *dh*-BN powders 67
Table 3-6 Fluorescence peak intensity fitting results for pristine *h*-BN 74
Table 3-7 Fluorescence peak intensity fitting results for *dh*-BN exposed to air for different durations..... 76
Table 3-8 Fluorescence peak intensity fitting for *dh*-BN with propene uptake exposed to air for 3 days.. 81
Table 5-1 Summary of calculated laser power density P, laser peak power density I_P and particle temperature T_P 132

1 INTRODUCTION

1.1 Motivations

Sustainability, through a more efficient use of natural resources to meet the growing demands in energy worldwide is a focus of research with strong research, economy, societal and cultural impacts. Despite the ongoing debates on climate change or the increasing need to become independent from fossil fuels, fundamental science pertaining to energy constitute a safe and exciting investment for the future.

Fossil fuels supply the majority of the energy needs of the world to date. However the processes involved in the production of these non-renewable resources are often toxic and contribute to global warming gas CO_2. To achieve a sustainable society, scientists and researchers have a responsibility to create and propose new environmental acceptable and technologically promising energy alternatives that would benefit real life applications. This quest is multi-pronged. The ability to harvest and convert energy efficiently constitute an important pillar of this problem. A second pillar is the ability to store energy. This applies to small gadgets and devices, as well as large scale structures, such as buildings or transportation infrastructures. A third important pillar is the ability to capture emissions of harmful gases with opportunities to transform them into value-added products – catalysts have a significant role to play in these activities.

Catalysis already plays an important role in industrial chemical conversion, transportation fuel production from fossil fuel and environmental pollution (water or air) control. However new needs for long term sustainable energy and for a cleaner and safer environment call for new catalysts to capture and convert molecules such as CO_2, methane, etc.

Nanotechnologies, through nanoscale instrumentation and nanomaterials, have emerged as critical tools to address this ambitious challenge. During the past few decades, the society has seen an exponential growth of nanoscience and nanotechnology, with which scientists and engineers can design, synthesize and control nanomaterials that offer advanced material properties for novel applications.

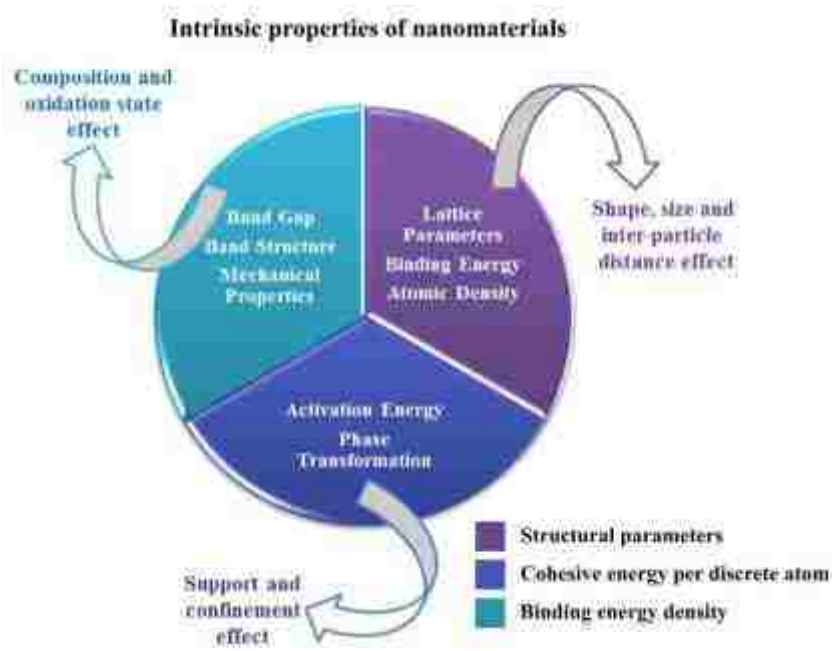

Figure 1–1 Summary of the potential relationships between intrinsic properties of nanomaterials on their catalytic activity.

Controlled synthesis of nanomaterials such as tuning the microstructure and chemical composition calls for detailed studies of the morphology, microstructure and the chemical composition at the nanoscale. Thus, for strong material synthesis achievements, tools offering high spatial resolution for morphological and functional studies are highly desired. Hence, the

development and implementation of multifunctional nanoscale characterization tools has become one important technical foundation of material by design.

1.2 Outline of the Present Work

The primary aim of this dissertation is to bring to light how powerful nanoscale functional imaging and spectroscopy can become to advance the development of renewable energy and catalysis systems.

In Chapter 2, we first focus on energy. Using atomic force microscopy (AFM), Kelvin probe force microscopy (KPFM), photoconductive AFM (pc-AFM), and nanomechanical modes, we show how relationships between the nanoscale properties of materials – such as the active layer of a solar cell or the electrode of a supercapacitor – and the corresponding device performance can be drawn.

In Chapter 3, we shift the focus to catalysis. Our work is illustrated with three case studies. First, using conventional imaging and spectroscopy we study the effectiveness of ball milling and heat treatment on introducing catalytically active defect in a two dimensional (2D) material-based material, hexagonal Boron Nitride (*h*-BN). Second, we study the effect of changing bearings media, size, number and the duration of the milling process on the performance of the catalyst. Third, we exploit infrared and fluorescence spectroscopy to evaluate the nature and density of the defects introduced in the flakes during ball milling.

In Chapter 4, we explore the nanoscale properties of the *h*-BN as a catalyst using AFM and AFM-based functional measurements to determine the changes in electrical and mechanical properties accompanying the reactivity of the flakes. We illustrate this through two case studies on heat treated flakes and laser-induced defect creation.

In Chapter 5, we build on the instrumentation limitations we have identified though the course of our studies and we present selected examples of proof-of-concept studies that aim at advancing the state of nanoscale instrumentation. Firstly, we discuss the implementation of light-assisted AFM-based nanomechanical spectroscopy for studying minute nanomechanical responses of Au nanoislands resulting from the light-matter interaction in nanostructures. Secondly, we discuss the implementation of multifrequency AFM to further our understanding of material structure-property-performance relationships.

Chapter 6 concludes with a discussion based on our results and observations throughout Chapters 2 to 5. We provide a broader perspective on future needs for nanoscale spectroscopy technology to benefit the field of energy and catalysis.

2 NANOSCALE IMAGING AND SPECTROSCOPY IN ENERGY APPLICATIONS

2.1 Background

Since first invented in the 1986 by Binning et al.[1], atomic force microscopy (AFM) has been regarded as the milestone instrument in the development of nanoscience and nanotechnology [1] as well as for material sciences, revolutionizing our understanding of materials and accelerating the development of new systems with improved performance. Basic AFM modes provide the morphological information of a sample surface, while the more advanced AFM modes allow the probing of electrical, magnetic, mechanical, chemical, thermal and opto-electronic properties of complex material devices. As shown in Figure 2-1, a typical AFM system consists of a microscale cantilever/probe with a sharp tip at/near the end of the cantilever (tip radius ranges from 1 to 100 nm). For imaging, the tip is engaged in contact (contact mode) or in the vicinity of the sample surface (tapping mode or non-contact mode). An AFM measurement is a reflection of the interactions between the AFM tip and the sample surface. AFM is sensitive to forces in the range of pico-newton (pN). The tip-sample interactions can be monitored using a read-out laser aligned on the top side of the cantilever, which gets reflected to the position sensitive photodetector (PSD). As the PSD outputs a deflection signal in Volts, the AFM needs to be calibrated to transform Volts readings into a suitable height measurement in nanometers. The spatial resolution is mainly limited by the radius of the tip, which can go down to few nanometers. This provides an imaging method with lateral resolution well beyond the optical diffraction limit of optical microscopy. Additionally, the relative height of features can be resolved, as detailed as atomic steps. A piezoelectric scanner (PZT) is used to raster the position

of the sample with respect to the tip, and feedback loop can be optimized for the cantilever to sense variations in sample surface topography precisely. For instance, to maintain a constant force between the tip and the sample, the piezo component can adjust the Z-displacement according to the error signal received from the deflection signal of the detector. In the case of sharp changes in height, feedback gains can be increased to improve the response of the piezo. We note that there is a fine balance between all imaging parameters in order to reach high resolution images. Overall, short (Van der Waals, capillary) and long range (electrostatic, magnetic) forces rule the tip-sample interaction. By controlling the tip-sample distance, it is thus possible to place the system in a regime in which short or long range force become preponderant. Each one of these special regime has been coined with a specific name, as described in a review by Gerber et al. [2].

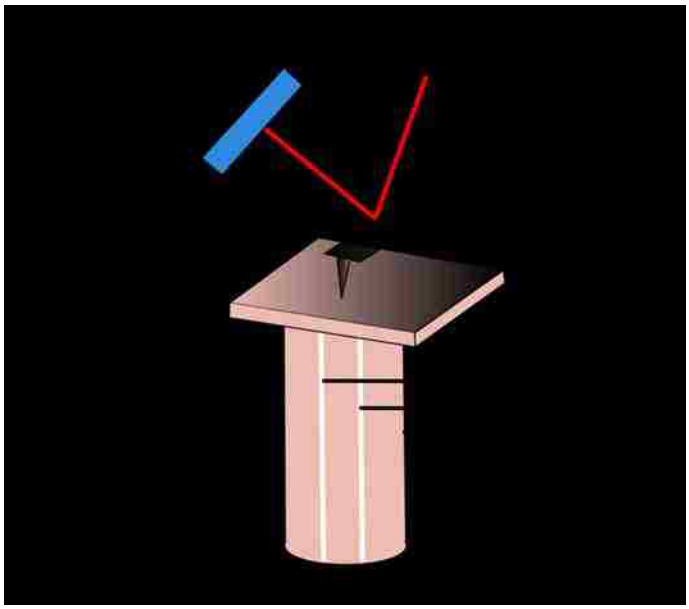

Figure 2–1 Schematic illustration of basic working principle of an atomic force microscope (AFM) representing the cantilever engaged with the sample surface, the laser read-out laser system to the detector, and the feedback controls to control the piezo for X-Y-Z motion during imaging.

In this chapter, we will focus on how morphological and functional AFM characterization can advance our understanding of the processing-structure-property-performance relationships in novel materials used for energy applications, specifically for energy harvesting and energy storage. Understanding how the local (i.e., sub-100 nm) morphology and other properties of active materials affect the performance of a device is important to achieve an efficient functionality-by-design development of materials for energy devices. This, in turn, will be enabling in delivering new materials for the next generation of energy harvesting or energy storage systems. The intricate micro/nanoscale morphological features of active materials and electrodes in these systems especially call for AFM characterization to establish new connections between the core principles (morphology, electronic properties, chemical composition, and phase transition) and device performance [3-5].

Since its introduction in the 1980s, AFM has supported the detailed understanding of functional materials such as those used in energy devices. Beyond morphology, forces relevant to chemical processes and electrical paths in active layers of a solar cell or electrodes of an energy storage device can be probed to pinpoint the limiting factors of energy conversion [6]. Such studies have been reported *ex situ* (the materials are characterized outside of the device) as well as *in operando* (as the device is operated in close to real conditions). The versatility and non-destructive nature of AFM measurements are key to identifying important bottleneck in material structures and compositions. For energy harvesting, the overlay of morphology and composition of the active layer with the photovoltage, photon-induced currents, and charge carrier lifetimes are of prime importance. For energy storage, electrochemical stain in systems such as batteries and evolution of electrodes work function upon cycling in supercapacitors constitute important factors impacting device performance. The most common modes of AFM to probe such

phenomena include photo-conductive AFM (pc-AFM)[6] and Kelvin probe force microscopy (KPFM) [7]. However, less exploited capabilities such as subsurface nanoscale imaging [8,9], nanomechanical and nano-infrared (nanoIR) spectroscopy measurements [10] have the potential to reveal important details of the structures and composition of the systems.

In this chapter, we will demonstrate how pc-AFM and KPFM can be used to extract important properties of energy harvesting (organic solar cells) and energy storage (electrode material for supercapacitors) materials. In each case, the instrumentation and image formation mechanisms will be carefully described. In a study focused on organic bulk heterojunction for a solar cell active layer, we will compare nanomechanical capabilities to differentiate polymeric components which cannot be resolved by conventional topography to elucidate important changes in the device performance. We will investigate how the structure and composition of the active layers relate to the local dark current and photo-currents. Next we will illustrate how nanoscale measurements, using KPFM, can support the development of electrode materials for supercapacitors. Lastly, we will discuss the current technical limitations, potential experimental pitfalls and perspectives of applying AFM-based nanoscale characterization techniques for the benefit of energy materials and devices.

2.2 Methods

2.2.1 Background and Motivation

The energy provided by sunlight strikes on the Earth is estimated as 4.3×10^{20} J per hour, which is larger than the total amount of current world demand of energy in a year (4.3×10^{20} J)[11]. By 2050 the yearly energy consumption is projected to reach 8×10^{20} J, with represents a two-fold increase of today's consumption. This is expected to more than triple by the end of this century [11]. To overcome the massive challenge of meeting the demand in energy production in a sustainable

manner, alternatives, such as solar energy harvesting devices, are being considered. Photovoltaic materials (also known as solar cell materials) hold great potential although the power conversion efficiency (PCE) reached with current devices remains in the ~20 % range, which suggests that opportunities for improvements remain. Historically, silicon has been the material of choice in the solar cell industry. However, in recent years, new configurations such as polymer solar cells (PSCs) and perovskite solar cells [12,13] have received a lot of attention because of the source material/reagents low cost ($/kW) [7], facile fabrication processes [3], as well as their ability to retain performance in a flexible device – of major interest for wearable fabric [14]. Among PSCs, bulk-heterojunctions (BHJs) have been actively considered before the emergence of perovskite materials. BHJs consist in combining electron donor (conjugated polymer) and acceptor (fullerenes derivatives) materials in a solution that is cast as single thin film active layer which will be sandwiched between an indium tin oxide (ITO) positive electrode and a low work function metal electrode. As in other solar cells, PCE is considered the most important parameter to assess device performance. PCE is determined by several key photo-physical processes taking place in the active layer of the device: charge carrier (electrons and holes) generation, transportation and collection [15].

It is now generally accepted that exciton generation, charge separation and charge transport after exciton dissociation [16-21] can be greatly impacted by the morphology and chemical composition of organic active layers of the BHJs. It was shown that structuring the materials is critical to maintaining the donor to acceptor length below 20 nm for efficient diffusion of excitons to interfaces [17,22,23]. In inorganic solar cells, p-n or p-i-n junctions with a planar structure are most commonly used. In this case, the selection of the p-type (p), n-type (n) and intrinsic (i) semiconductor layers is critical. In perovskite solar cells, the best configuration of the solar cell

has not yet been agreed upon. At the grain level, it is known that the exciton diffusion length in perovskite can range from a few hundreds of nanometers to several micrometers [24,25]. However, a detailed understanding of the effect of intragrain defects, grain boundary defects and intergrain interactions on the mechanisms of charge transport in perovskites is still in its infancy [26].

Beyond the work that will be discussed in this section, a number of recent reports suggest the need to explore properties of solar cell materials at the nanoscale. In the span of a few years, proof of concepts using photo-conductive AFM (pc-AFM) [27-32], Kelvin Probe Force Microscopy (KPFM) [26,32-34] and nanoscale infrared (nanoIR) spectroscopy [32,35,36] have unveiled some properties of active layers of solar cells at the nanoscale, well beyond the typical morphology imaging obtained with AFM. For instance, methyl-ammonium lead triiodide perovskite, one of the most common soft perovskite used for solar cell research to date due to its facile and low cost solution processing, has been receiving enormous interest. Variability of crystallinity and high defect concentrations inside the grains have affected the local efficiency of the material, thus limiting PCE of the solar cells. Kutes et al. used pc-AFM to study the local photovoltaic performance of the material [27]. By mapping the conductance across the material with nanoscale spatial resolution under dark conditions and under visible illumination, it is possible to assess the photovoltaic properties such as short-circuit current (J_{sc}), open-circuit voltage (V_{oc}) and maximum power point. J_{sc} maps indicate an increase from a mean 0.06 pA to a mean 41.8 pA with hot spots reaching 100 pA upon illumination (broad range in the visible) representing less than 20% of the area scanned. Despite the disparities observed, solar cells made of these films exhibited PCE close to 15%. Interestingly several regions showed unexpectedly high (or low) J_{sc} at the grain boundary. However, the origin of these behaviors remains unclear: the physical traits, composition, orientation can influence the current pathways but the current AFM

platforms cannot provide such a broad array of functional mapping. Besides the origin of these variations, the correlation the different functions of the device is not straightforward – statistical analysis of the data will likely be required to unveil correlations. More recent work by Yuan et al. [34] suggests that local interfacial ion accumulations could be responsible for increase in open circuit voltage of the device, and is highly dependent on the distance between the electrodes, on the electric field applied for poling and on time. Furthermore, studying the local carrier dynamics *in operando* has also been demonstrated using KPFM [26,33] by mapping the internal electrical potential (electric field) across the stacks of layers of the device-like structure fabricated for the study. The results were used to determine the nature of the junction formed by the electron transport layer, active layer and hole transport layer. New opto- and electronic developments for AFM methods now also extend the photocurrent and surface potential capabilities to quantify the energy dissipation related to carrier transport [29], carrier lifetime [29,37,38], charge extraction [33] and ionic transport [29] using time resolved measurements [37,39].

Nonetheless, despite a recent surge in this line of work, overall, the paucity of studies using nanoscale functional probing to interrogate the material locally for simultaneous structural, chemical and electrical properties, in a form that can establish relationships to devices performance greatly hinders the optimization of the materials, including their composition, fabrication and processing, to achieve higher efficiency and stability.

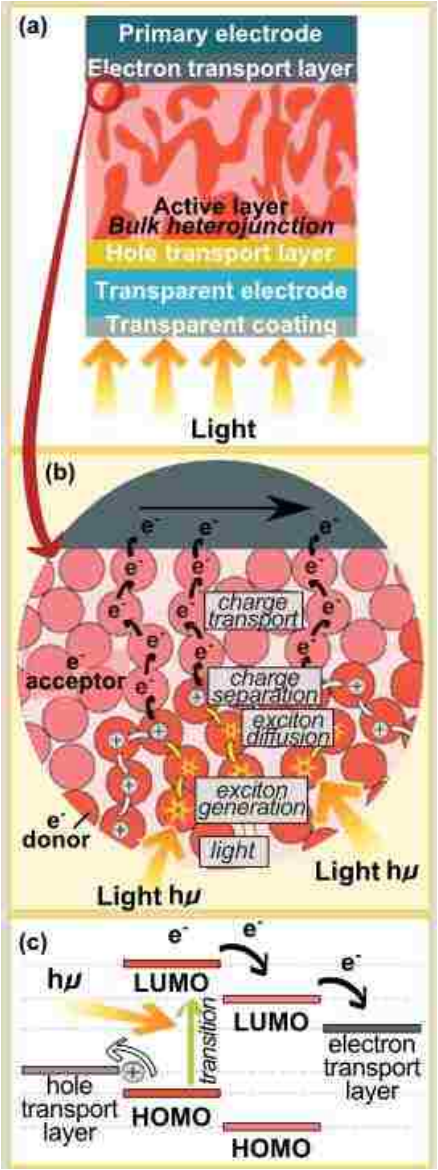

Figure 2–2 Schematic illustration of the key nanoscale processes that determine the performance of the BHJ solar cells. BHJ from (a) bulk to (b) nano to (c) charge carrier transfers illustrated with the energy levels of the hole transport layer (gray), HOMO and LUMO of the electron donor (red) and electron acceptor (pink), and electron transport layer (blue).

Active layers used in PSCs are designed, as shown in Figure 2-2, so that when light travels through the transparent ITO electrode layer, photons with energies in the absorption band of

donor materials will be absorbed and generate excitons (electron-hole pairs), then diffuse to the donor-acceptor interface junction. At the junction, excitons generated by donor materials will separate into holes and electrons, which will diffuse from the lowest unoccupied molecular orbital (LUMO) of the donor material to the LUMO of the acceptor material and finally to the electron transport layer. Meanwhile, holes will transfer from the highest occupied molecular orbitals (HOMO) of the acceptor material to the HOMO of the donor material at the donor-acceptor interface [40] to be collected for the hole transport layer. The ability for charge carriers to efficiently reach the electrodes without recombination constitutes a major challenge to the efficiency. Recent studies reveal that the processes determining ultimate device performance are dependent on material morphology [16,18-20,41]. Hence the device performance improvements are limited by a morphology-related dilemma: charge carriers (excitons) can only diffuse for a maximum of 20 nm [41,42] but large donor-acceptor interfacial areas should be provided, while the donor or acceptor rich phases should form interconnected pathways for the free electrons/holes to diffuse freely to the respective electrodes. In bulk heterojunctions (BHJs), acceptor (fullerene derivatives) and donor materials (conjugated polymers) are mixed to form a single active layer with nanoscale phases of acceptors and donors, in which the diffusion of the charge carrier are expected to take place in a more optimized manner. BHJs current PCE is still limited to ~11.2%, much lower than their inorganic counterparts (up to 26.7% for Si crystalline cell)[43]. This low power conversion efficiency is thought to be directly related to the discrepancies in the film morphology at the nanoscale because the BHJs consist of various phase domains surrounded by complex interfaces that can introduce undesirable charge carrier recombinations. The theoretical formulation of a solar cell PCE can be expressed as

$$PCE = J_{SC} V_{OC} FF / P_{in} \quad (1)$$

Where $\boldsymbol{J_{SC}}$ is the short circuit current, which depends on the light absorption efficiency of the active layer, exciton diffusion and dissociation, charge transportation and collection,

$\boldsymbol{V_{OC}}$ is the open circuit voltage, which is determined by energy level difference between the acceptor LUMO level and donor HOMO level,

$\boldsymbol{FF}$ is the fill factor determined by the resistance of the whole device and P_{in} is the power of the incident radiation [44].

It has been established that a detailed understanding of the multiscale structure-properties-performance relationships of BHJs is required to overcome their current limitations. In particular, we are interested here in a non-invasive characterization that would reveal the dynamic physical, chemical and electrical processes at the nanoscale to identify more precisely the key mechanism of how photo-to-electron conversion is affected by the disordered BHJ active layer morphology.

In this section, we will describe our study aiming at understanding the nanoscale morphology-related electrical and opto-electrical properties ruling BHJ performance through our customized AFM-based nanoscale functional mapping platforms. More specifically, we will study the effect of solvent and film formation processes on the local morphology, phase separation, dark current and photo-current generation. This work was carried out in collaboration with Dr. Thomas' group at UCF. The material synthesis and active layer processing were performed by Dr. Thomas and Dr. Li, and are summarized here for completeness.

2.2.2 Methods

2.2.2.1 Sample preparation

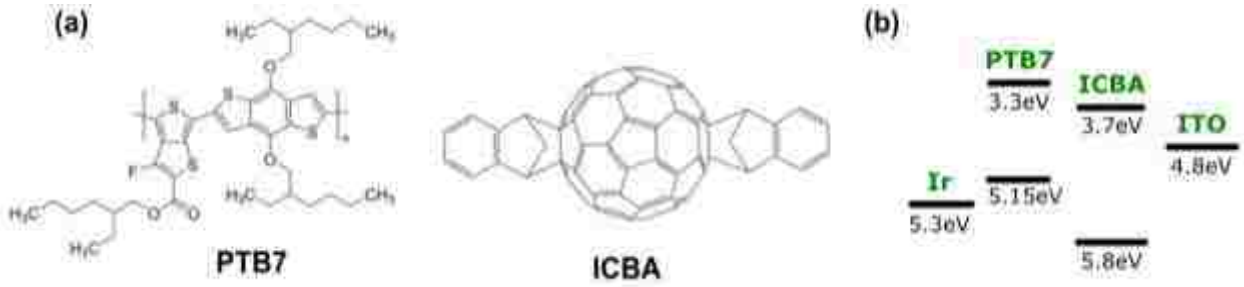

Figure 2–3 (a) Chemical structure of PTB7 and ICBA used as electron donor and acceptor, respectively; (b) Representative energy-level diagram of the fabricated device, including electrode materials (Ir and ITO) and electron donor (PTB7) and acceptor (ICBA).

The material was prepared by our collaborators (Dr. Thomas' group at UCF NSTC) as described in [30]. In short, ITO covered glass substrates were cleaned by detergent, deionized water, acetone and isopropanol under sonication for 15 min, respectively. The ITO substrates were then exposed to UV–ozone for 15 min.

A 40 nm layer of poly (ethylenedioxythiophene): poly (styrenesulfonic acid) (PEDOT:PSS) was spin-coated on the ITO substrate. The PEDOT:PSS-coated samples were then baked at 120 °C for 20 min before transferring into a nitrogen-filled glovebox. Next, blends of thieno[3,4-b]thiophene/benzodithiophene (PTB7): indene-C60 bisadduct (ICBA) (12.5 mg/mL for PTB7, 12.5 mg/mL for ICBA) prepared in a mixture of solvent were spin-coated on the PEDOT:PSS layer to form the active layer. In this study, we studied the effect of different solvents on the resulting local material morphology, properties and performance. Two different mixtures of solvents, which we will refer to as "binary" (chlorobenzene (CB)/1,8-diiodooctane (DIO) with volume ratio CB/DIO 97:3) and "ternary" (chlorobenzene (CB)/chloroform (CF)/1, 8-

diiodooctane (DIO) with volume ratio 78:19:3) were considered to prepare the PTB7:ICBA active layers.

2.2.2.2 Photovoltaic property characterization

A solar simulator with a 300 W Xenon lamp and AM1.5G global filter was used as radiation source. The light intensity was calibrated using a silicon photovoltaic reference cell (Newport, 91150 V) to achieve a value of 100 mW cm^{-2}. Current–voltage characteristic curves were measured with a Keithley 2635A source measurement unit. J_{SC} and V_{OC} values were extracted directly from the J-V curves and FF and PCE values.

2.2.2.3 Morphology measurement using AFM-based modules

Several modes of AFM have been introduced to quantify the nanoscale mechanical properties of materials to overlay with morphological AFM images. Here we consider a mode called Pulse Force Microscopy (PFM). The detailed description of PFM is provided in Appendix 1. In short, the tip-sample distance can be modulated to produce a force curve at each pixel of the image. AFM force curves are commonly used to determine the stiffness of a material, as well as the energy dissipated during the tip-sample interaction and the tip-sample adhesion (see Appendix 1 for schematics and details). PFM was conducted on a WITec Confocal Raman-AFM system using a Mikromasch cantilever (HQ:CSC38/AL BS, tip B).

The films were also characterized with multifrequency AFM, a technique called Mode Synthesizing AFM (MSAFM). In MSAFM, the AFM cantilever is excited at a frequency f_c by a piezo-ceramic component mounted on the cantilever holder while the sample is actuated at another frequency f_s using a piezo-ceramic disc placed underneath the sample. Due to nonlinear tip-sample interaction, the two waves (f_s and f_c) are mixed to generate new modes at sum ($f_s + f_c$)

and difference $|f_s - f_c|$ frequencies. The synthesized modes have been demonstrated to be very sensitive in materials variations in density or mechanical property [45,46].

2.2.2.4 Dark current and photocurrent measurements

pc-AFM was carried out to study the electrical/opto-electric properties of the BHJ active layers. Tapping mode AFM (AFM, Dimension 3100, Veeco) was first used to characterize surface morphology of all samples. The ITO layer was glued to a metallic sample holder using conductive silver paste to apply the DC bias directly on the sample. The conductive platinum-coated probes with tip radius of 10-20 nm (MikroMasch XSC11/Pt) were used to measure the current through the sample at local regions across the film. In this way, the sample disc and the AFM cantilever tip mimic the two electrodes of a PSC device. pc-AFM (Multimode AFM from Veeco) measures the current flow at nanoscale size regions where the AFM cantilever is in contact. The current was collected at a fixed bias and mapped across the region of interest, or the bias was swept to obtain an I-V curve at a fixed location. The current sensitivity of the pc-AFM module used in this study was in the range of pico-ampere (pA). To protect the PSCs from degradation introduced by oxidation and humidity, we placed the microscope in a glove bag, which was first purged and then filled with nitrogen gas prior to imaging. Without illumination, these constituted our dark field measurements. Photocurrents were evaluated by illuminating the sample with an optical module mimicking solar source. The light intensity was 100 mA/cm^2. The current levels were recorded with light off and light on to compare the response of binary and ternary materials under visible light illumination. With this approach, the morphology, electrical properties and opto-electrical performances were evaluated simultaneously with nanoscale spatial resolution.

2.2.2.5 Bias-dependent photocurrent measurements

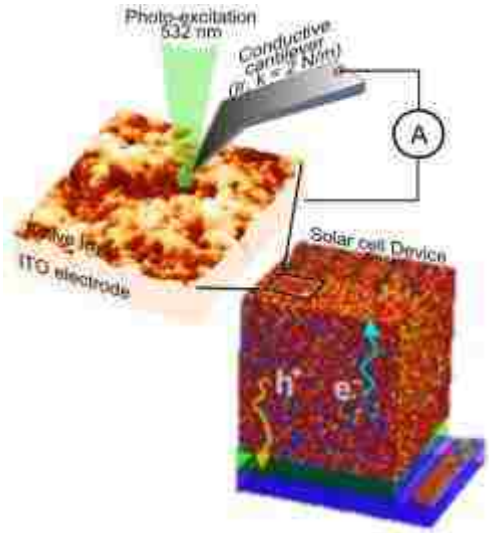

Figure 2–4 Schematic diagram of top illumination configuration for local current spectroscopy with pc-AFM.

Bias-dependent pc-AFM measurements were performed at The Center for Nanophase Materials Sciences (CNMS) at Oak Ridge National Laboratory (ORNL) on a NTEGRA Spectra (NT-MDT) AFM equipped with a conductivity measurement module, as shown in the Figure 2-4. Soft conductive AFM cantilevers with Iridium coating were used for all conductivity measurements. A 532 nm green laser was focused to the very end of an AFM tip through a long working distance 100X objective lens. Dark current and photo-induced current were acquired simultaneously with morphology.

I-V curves were acquired at 10X10 points i.e., with 50 nm resolution step. At each pixel the bias applied was ramped through Labview program from 0 V to 4.5 V to record I-V curves, both in the dark-current (light off) and in the photo-current (light on) conditions.

2.2.3 Results and Discussion

2.2.3.1 Device Evaluation

The evaluation of the devices assembled with the aforementioned materials was carried out by assembling a solar cell. All of this work was performed by Dr. Thomas' group. The results obtained, as reported in [30], are summarized in Table 2-1, for the sake of discussion. As can be seen, by using the ternary solvent, the performance of the solar cell could be improved with a PCE of 6.3% instead of 5.2% with the film resulting from the binary solvent mixture. The V_{OC}, J_{SC} and FF were also higher when using the ternary solvent. The aim of the nanoscale study was to help the device experts in pinpointing the origin of these changes.

Table 2-1 Photovoltaic results of PSCs with active layers prepared by different solvents

Processing solvent	**V_{OC} (V)**	**J_{SC} (mA cm^{-2})**	**Calculated J_{SC} (mA cm^{-2})**	**FF (%)**	**PCE (%)**
CB/DIO (97:3 v/v)	0.91 (0.91)	12.79 (12.93)	12.71	45 (46)	5.24 (5.48)
CB/CF/DIO (78:19:3 v/v/v)	0.93 (0.93)	13.91 (14.23)	13.84	49 (50)	6.34(6.61)

2.2.3.2 Morphology and nanomechanical measurements

In our study, donor and acceptor materials are blended in the film, making distinguishing the two domains from AFM topography difficult. However, because the two polymeric materials are very different in mechanical property (ICBA-rich domains are expected to be stiffer than PTB7-rich domains because of the rigid carbon framework of ICBA) our evaluation of the nanoscale properties of the two PTB7:ICBA films was first focused on the morphology and nanomechanical properties of the films.

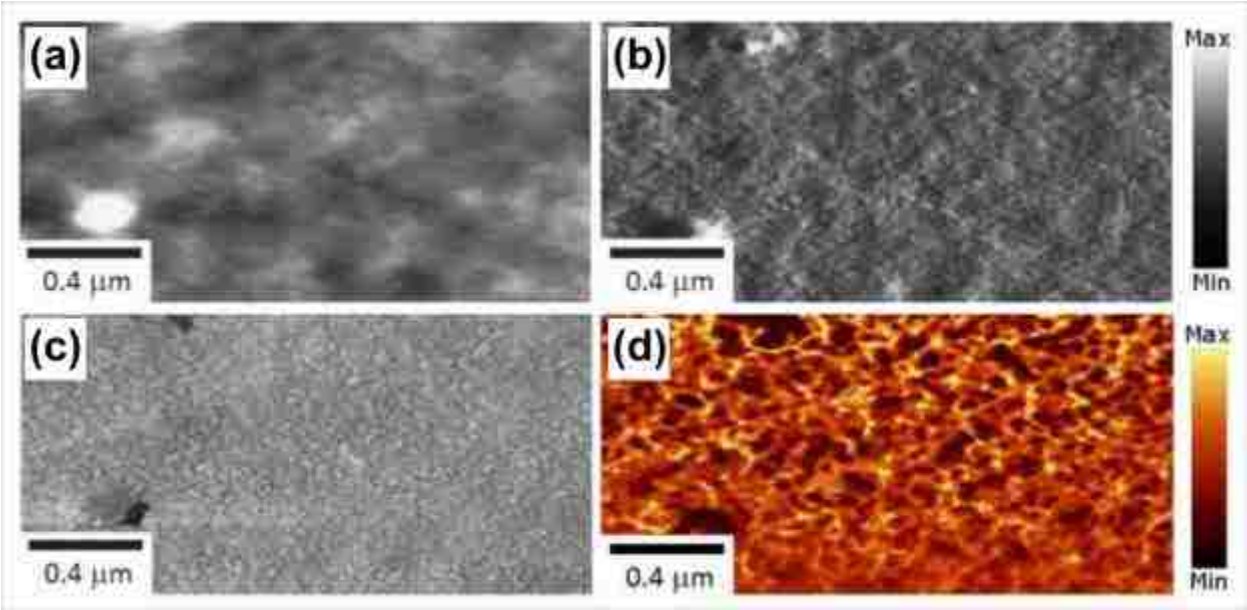

Figure 2–5 Various imaging modes of the active layer. (a) Height image (b) Tapping mode amplitude AFM image (c) Tapping mode phase AFM image (d) MSAFM amplitude image. Image size for all AFM images is 2×1 μm [30].

In Figure 2-5, we compare the details obtained from topography AFM and MSAFM imaging for the same regions of the film obtained with the binary solvent. Tapping mode has been used for its ability to differentiate regions of different chemical composition[47] via phase imaging. However, this this case, neither the topography (Figure 2-5 (a)), nor the amplitude (Figure 2-5 (b)), nor the phase (Figure 2-5 (c)) images could distinctively reveal the PTB7 or ICBA regions. MSAFM (Figure 2-5 (d)) obtained offered higher contrast so the domains and even interstitial regions could be identified. After establishing that MSAFM could be used in lieu of topography maps, we carried out a comparison of the two films using MSAFM and PFM (for nanomechanical details).

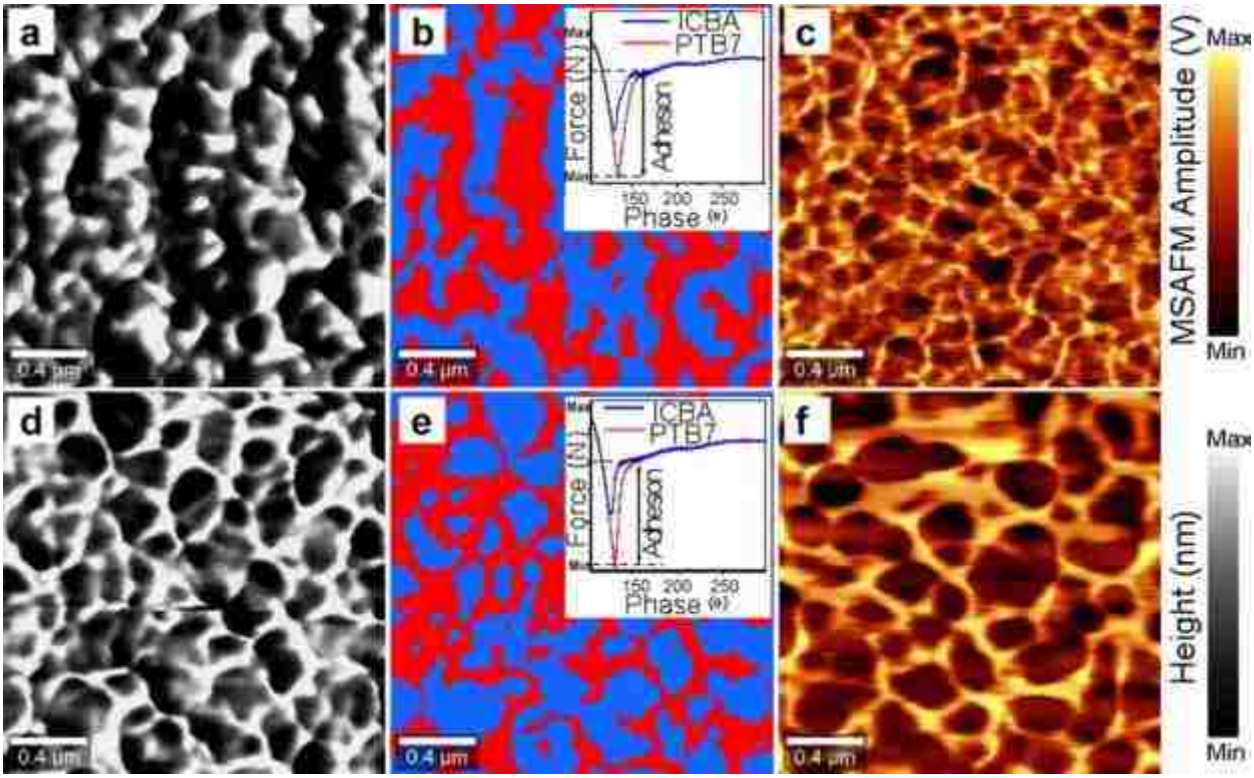

Figure 2–6 Nanoscale characterization of PTB7:ICBA blend films prepared by binary (a-c) and ternary (d-f) mixture of solvents. (a,d) AFM adhesion maps extracted from PFM measurements; (b, e) correlative cluster analysis maps for AFM adhesion maps with ICBA and PTB7 domain identified; (c, f) MSAFM maps. Image size for all AFM images are 2×2 µm [30].

Figure 2-6 (a) and (d) are the adhesion maps for the two PTB7:ICBA films obtained with PFM. By doing k-mean cluster analysis on the dataset, the PTB7-rich and ICBA-rich domains were successfully distinguished with red-colored regions corresponding to PTB7-rich domains and blue-colored region corresponding to ICBA-rich domains. The two inset figures of Figure 2-6 (b) and (e) represent the adhesion profiles at a selected point of the image. The PFM maps reveal that the domain size and the distribution of the two domains are very different for the films prepared by binary and ternary solvents but further differentiations of the domain sizes and distribution are difficult from the PFM results.

In order to better resolve the two domains, MSAFM measurements were conducted. By comparing the MSAFM maps (Figure 2-6 (c) and (f)) to PFM maps (Figure 2-6 (a) and (d)), it became clear that MSAFM can provide a better contrast for the two domains. The micro-structured domain-domain boundaries could also be resolved. In the MSAFM maps, the bright color regions are identified as PTB7-rich domains while as the dark color regions are identified as ICBA-rich domains. As shown in Figure 2-6 (c), for active layer prepared by binary solvent, the ICBA-rich domains sizes were smaller than the ones obtained with the ternary solvent (Figure 2-6 (f)). One would expect the performance of the former active layer would be improved with smaller domains, corresponding to interfacial surface areas and smaller distances to travel for excitons. However, for the active layer prepared with the binary solvent, the high resolution MSAFM amplitude maps indicate that the ICBA-rich interstitial regions are highly discontinuous. This lack of continuous pathways would critically hinder the charge carriers travel to the electrodes. Furthermore, the existence of the color changing gradients within each domain suggests non-homogeneities in each phase. This would also be definitely detrimental to the ultimate device performance. In comparison, as shown in Figure 2-6 (f), the active layer prepared by ternary solvent gives larger ICBA-rich domain sizes with very continuous interfacial pathways. A more homogeneous material was indicated by the even distribution in colors for each phase.

2.2.3.3 Dark field and photocurrent measurements

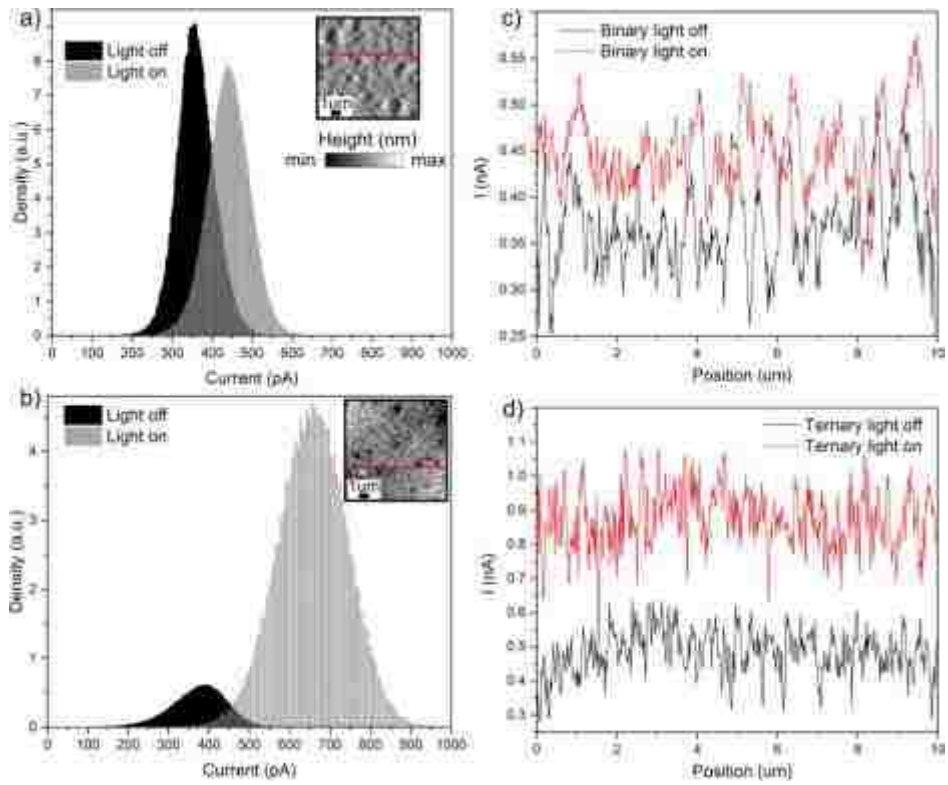

Figure 2–7 Dark and photocurrent densities measured by pc-AFM (DC bias at -4V) for PSCs with active layers prepared with binary (a, c) and ternary solvents (b, d). Inset images on (a) and (b) are the morphology images showing the regions where the respective histograms of current values are extracted. Figure 2-7 (c and d) show the line profiles of the current change across the sample as a result of white light illumination (red curves) [30].

As shown in Equation 1, PCE is proportional to the close circuit current density (J_{SC}) thus current density is a very important parameter to assess the PSCs performance. From the photovoltaic property characterization results listed in Table 2-1, we can see that the increased current density value was the main contributor of the improved PCE for the active layer prepared by ternary solvent. In this section, pc-AFM was used to map the distribution of current reaching the AFM tip in contact with a film deposited on an ITO electrode. In Figure 2-7, the current

levels were recorded with light off (black curves) and light on (gray and red curves) to compare the response of binary and ternary materials to visible light illumination.

The current density levels with light on and light off were measured on the two films. The results are presented in the form of a histogram in Figure 2-7 (a) and (b). The selected region is a 10 × 10 μm area. The respective morphology AFM images are shown as the inset in Figure 2-7 (a) and (b). For the active layer prepared by ternary solvent, its overall current distribution (Figure 2-7 (a)) and the mean current line profile Fig 2-7 (b) were both higher than those extracted from the active layer prepared with the binary solvent (Figure 2-7 (c) and (d)). Our nanoscale characterization results are consistent with the photovoltaic properties characterization results listed in Table 2-1.

2.2.3.4 Bias-dependent photocurrent measurement

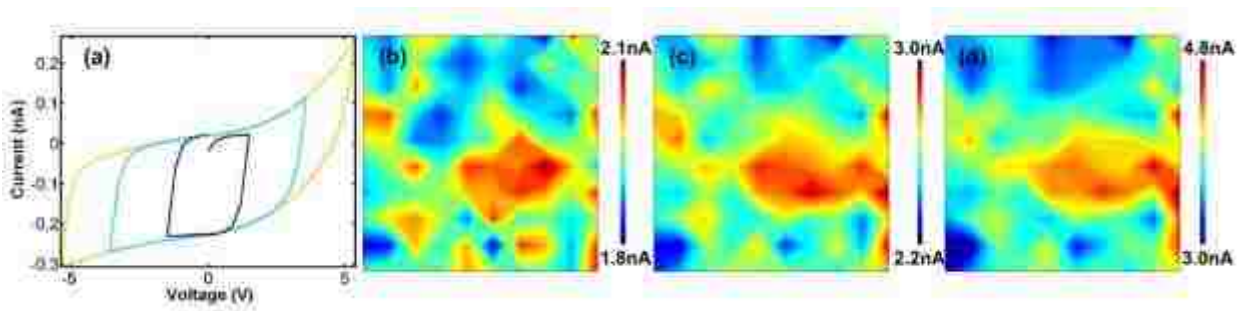

Figure 2–8 Dark current responses (a) averaged I-V curve, current mapping at bias (b) 1.5 V (c) 3.0 V and (d) 4.5 V (Scan Size: 500 nm)

Next, we evaluated the behaviour of the films under cycling biases (Figure 2-8 and 2-9). In this approach, similar setup to the one described in the previous section was implemented, but the bias was varied from 0 to 5 V and back to 0 V for each point of the image. The data was collected in the form of a 3D array, which would be analyzed off line to extract individual I-V

curves (Figure 2-8 (a)) or maps are selected biases (Figure 2-8 (b-d)). In the case of the dark current (Figure 2-8), the maps indicated heterogeneities within the films, and the area of the regions with high current (red) increased with higher biases, as seen in Figure 2-8 (d). Because the work function of Ir-coated tip (5.3 eV) is higher than that for ITO (4.9 eV), holes were injected from the tip and travelled through PTB7 to ITO. Thus the regions with higher current should correspond to PTB7 (donor)-rich domains. This is consistent with the results obtained with PFM and MSAFM, showing a distribution of PTB7-rich and ICBA-rich phases. However, we note that other factors may come into play as the regions revealed by the current maps seemed sometimes larger than the morphology of the phases. We should however underline that the current maps are an indication of the paths of charges in the samples, which is highly dependent of the pathways present in the volume of the material, with complex three-dimensional configurations.

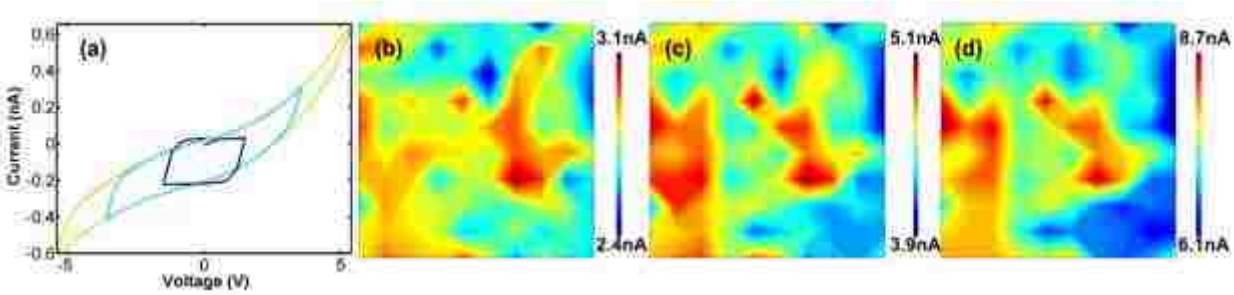

Figure 2–9 Photo-current responses (a) averaged I-V curve, current mapping at bias (b) 1.5 V (c) 3.0 V and (d) 4.5 V (Scan Size: 500 nm)

Photocurrents lead to a significant increase in the currents measured. At 5 V, the maximum current reached 0.6 nA (Figure 2-9 (a)) compared to ~0.25 nA for the dark current. This increase was attributed to the photo-generated holes increasing the charge carrier density upon laser excitation.

The bias sweep for a selected array of points also allowed us to visualize the effect of increasing bias on charge collection by reconstructing the current maps at selected biases. At +1.5 V, only a small fraction of the film generated current (Figure 2-9 (b)), which significantly increased with increasing biases of 3 V and 4.5 V (Figure 2-9 (c) and (d), respectively). Topography images did not reveal any change before and after the measurements, thus we infer that the observed bias-dependent current responses resulted from the charges flow engendered by the illumination of the film.

2.2.4 Conclusions

Overall, the results presented in our study show that using the ternary solvent to form the active layer lead to better defined material domains. The performance of the resulting devices suggests that these clear pathways and homogeneous phases promote better performance.

The morphological and mechanical details should be complemented with dark current and photo current maps together with I-V spectroscopy, as the surface topography alone cannot explain all the variations in the films. The bias-dependent measurements constitute a nice add-on that enables the visualization of the behavior of the same region at increasing biases. We note that hysteresis loops have been observed in the I-V curves, which have not been reported on this type of materials in the literature. It has been widely observed in organic perovskite solar cell materials and recent studies have attributed the hysteresis behavior to the crystalline structure inside the organic perovskite materials[48,49]. More studies will be required to figure out the origin of the hysteresis loops.

Lastly, a very important point from the instrumentation perspective, is that the measurements reported here, as well as the ones presented in all the reports described in the background,

correspond to surface measurements by the cantilever tip. The increase in photocurrent indicates the formation of exciton and subsequent movement of electrons and holes to the electrodes. However, a tool to directly probe these phenomena in the volume of the sample is not readily available. Although challenging, this would constitute a transformative approach for the study of three dimensional functional materials such as BHJs. We note that the use of subsurface nanoscale imaging could potentially be of interest in the future, to reconstruct a three dimensional nanoscale rendering of the composite and ideally of its functions.

2.3 Nanoscale Imaging and Spectroscopy for Energy Storage Materials

2.3.1 Background and Motivation

The ever-increasing demand for energy to satisfy the needs for worldwide consumption and the global environmental concerns caused by depleting the non-renewable fossil fuels, not only bolster the research for energy harvesting systems but also for efficient energy storage systems. The society has witnessed an explosive growth in an interest in the development of high energy density storage systems, such as supercapacitors, particularly to reliably cater the residential and commercial energy needs. Though batteries especially rechargeable batteries such as lithium-ion batteries have been widely used as dominant energy storage systems for various electronic devices and electronic vehicles, their wider applications are limited by their limited life cycle and low power performance [50].

Supercapacitors, also known as ultracapacitors, offer key technical characteristics such as high power density, long cycle life and rapid charging-discharging rate [51-54]. A typical supercapacitor consists of two electrodes: an electrolyte which is used to separate the two electrodes and a

separator which allows the transfer of ions and electrically insulates the two electrodes. Based on their working mechanisms for energy storage, supercapacitors can generally be classified into three types [55,56]. The first type is known as electrical double-layer capacitors (EDLCs or EDLs) in which the energy is stored through the electrostatic charges accumulated on the electrode-electrolyte interface. The performance of EDLCs relies on the electrode specific surface areas and electrode surface porosity for electrolyte ions and their current drawbacks include low energy density. The second type is referred to as pseudo-capacitors, also known as electrochemical capacitors (ECs). ECs store power through fast and reversible faradaic (oxidation/reduction) reactions that occur on the surface or near-surface of electrodes [57]. Though the energy density that can be achieved by ECs is higher than that by EDLCs, their widespread application is limited by their poor cycle stability and low electrical conductivity [58]. The third type of capacitors, coined hybrid capacitors, combines an EDLC and an EC.

Important factors related to supercapacitors performance include:

The energy density: This is defined as the amount of energy that can be stored per unit weight. What can be achieved by supercapacitors to date is significant lower than that can be achieved by the state-of-art batteries, therefore the improvement of energy density is of great importance for supercapacitors[59]. In fact, the energy density is given by

$$E = \frac{1}{2} C V^2 \tag{2}$$

where E represents energy density, C represents the capacitance and V is the operation voltage [59]. This indicates that the operation voltage should be maximized in order to improve a higher energy density. Meanwhile the operation voltage window is determined by the electrode materials. At the moment there is no complete understanding of different methods of widening

operation voltage window. Previous studies revealed that electrode materials with the largest work function difference can provide the largest operation voltage window [59,60], i.e. in an asymmetric capacitor.

The electrodes: Electrodes play an important role in the performance of supercapacitors and represent an area of active research, especially in terms of nanomaterials. Depending on the selection of electrode materials, supercapacitors can be classified as symmetric (two electrodes are identical) and asymmetric (two electrodes are made of different materials) capacitors. The work function of the electrodes comes into play in the working potential, expressed as

$$E = E_0 + \Delta E_1 + \Delta E_2 = 1/F\ (\omega^{\beta}-\omega^{\alpha})\ N_A + \Delta E_1 + \Delta E_2 \qquad (3)$$

where ΔE_1 and ΔE_2 are the surface potential of positive and negative electrodes, respectively, ω^{α} and ω^{β} are the work function of positive and negative electrodes, respectively, and N_A is the Avogadro's number. It is important to note that the work function values of the two electrodes can be modified by various factors including the change of electrode material morphology as well as the adsorption of ions on the surface of electrodes [60].

The development of stable, long-lasting and high energy density supercapacitors necessarily entails the understanding of the systems' electrochemical performance. Significant progress has been made to investigate the effect of different electrode materials and various fabrication methods on the performance of supercapacitors at the device level. Yet, comprehensive investigations of the structure-properties-performance relationships for supercapacitors at the nanoscale are still lacking.

In this section, we will describe a detailed study in characterizing the change of morphology and work function values for supercapacitor electrode materials after cycling through the application of KPFM.

KPFM, the principle of which will be described in detail in the Methods, measures the work function difference between a conductive AFM probe and the sample surface through the direct measurement of contact potential difference (V_{CPD}). In KPFM, maps of topography and contact potential differences across sample surfaces can be acquired simultaneously. Since the work function of the AFM probe is either known or can be calculated from calibration steps, the morphology-related work function distribution can then be extracted. In addition, we will also demonstrate the application of KPFM in imaging the voltage response of the electrode material before and after specific cycling steps.

Finally, we will highlight the protocols we have developed for sample preparation and KPFM measurements in order to get repeatable and reliable KPFM data, and discuss some configuration modifications that should be considered for more quantitative evaluation.

2.3.2 Methods

2.3.2.1 Sample fabrication

All samples were prepared by Dr. Thomas' group at UCF NSTC. Specifically, we studied two kinds of supercapacitors.

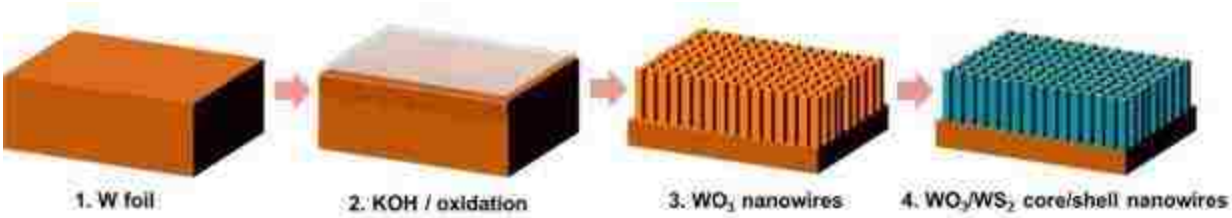

Figure 2–10 Schematic illustration of the fabrication process [61]

WO_3/WS_2 core/shell nanowire supercapacitor: Figure 2-10 illustrates the key steps of the fabrication of core/shell nanowire supercapacitor. First a thin tungsten (W) foil with the thickness of 100 μm was cleaned in an ultrasonic bath using acetone, hydrochloric acid, ethanol and DI water, respectively. Then a layer of KOH was prepared on top of the dried cleaned W foil surface through drop cast and subsequent spin coating of a 10 wt. % KOH solution. The W foil with KOH layer was kept in a furnace at atmospheric pressure at 650 ˚C for 2 h to allow the growth of the vertically aligned h-WO_3 nanowires. The furnace then cooled down naturally to the room temperature. The sample was cleaned using DI water and dried. In order to convert the outmost surface of h-WO_3 to WS_2, the nanowires sitting on the W foil were then placed in a quartz tube CVD (chemical vapor deposition) furnace which was heated to 850 ˚C in a heating rate of 20 ˚C/min and kept at 850 ˚C for 40 min. The pressure of the furnace tube was maintained at 10^{-3} Torr and Argon gas was constantly sent into the tube.

RGO/Nickel foam supercapacitor: Sample preparation was conducted according to Yang's method [57], the deposition of reduced graphene oxide flakes on Ni foams were conducted through a three-electrode systems where the Ni foam worked as a working electrode, a Pt wire worked as counter electrode and Ag/AgCl worked as a reference electrode. A mixed solution of 0.15 M $LiClO_4$ and 7.5 mg mL^{-1} was employed as the electrolyte.

2.3.2.2 Charge-discharge cycling

All samples were cycled by Dr. Thomas' group at UCF NSTC. The charge-discharge cycling was applied through the electrochemical measurement platform, where a 0.1 M $NaSO_4$ solution was used as the electrolyte. The electrochemical measurements were conducted through a three electrode test configuration. The supercapacitor sample on a W foil with ~1cm^2 area was used as the working electrode, a Ag/AgCl was used as the reference electrode and a Pt foil was used as the counter electrode. For all samples, 10000 charge-discharge cycling were performed.

2.3.2.3 Sample mounting for KPFM measurement

The WO_3/WS_2 core/shell nanowire supercapacitor samples obtained as synthesized and after charge-discharge cycling were mounted on a metallic AFM sample disc using silver paste (PELCO® Conductive Graphite, Isopropanol base, TED PELLA) for KPFM measurements.

For RGO/Nickel supercapacitor samples as synthesized and after charge-discharge cycling, the RGO flakes deposited in the nickel foam network were carefully collected using fine tweezers. A tiny drop of silver paste was spread on top of the metallic AFM sample disc. Before the silver paste fully dried, the RGO flakes were individually transferred. The transfer was performed using a fine wet toothpick to adhere the flakes without contamination or damage. Great care was taken to avoid any contamination on the top surface of the RGO flakes from silver paste and the transfer was done very gently to avoid any mechanical damage of the RGO flakes.

2.3.2.4 KPFM characterization

KPFM module is an AFM-based advanced module that is commonly used to characterize electrical properties of materials with KPFM through the measurement of the work function difference between a sample and a conductive probe. Tip-sample work function difference is also

known as contact potential difference (V_{CPD}). The work function of a material is known to affect different surface properties [62].

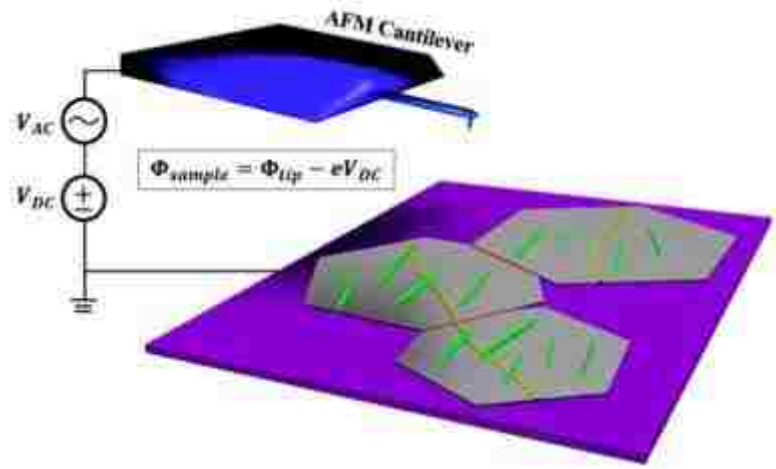

Figure 2–11 Schematic of Kelvin probe force microscopy [63]

As shown in Figure 2-11, KPFM signals are normally acquired using a two-pass method. During the first pass, the cantilever is mechanically driven at its resonant frequency, i.e. in tapping mode, to determine the topography of the sample. During the second-pass scan, the cantilever is lifted up by a fixed distance (30 nm in this case) to minimize the effect of short range van der Waals forces and maximize the effect of long range forces. A bias is applied (ΔV) which includes a DC and an AC components to the cantilever, i.e., $\Delta V=V_{DC}+V_{AC}$. The AC component is used to electrically vibrate the cantilever at its resonant frequency while V_{DC} is chosen by the AFM controller to null the force gradient resulting from the differences between the tip work function (φ_{tip}) and the sample work function (φ_s). V_{DC} (referred to here as V_{CPD}) is recorded and plotted as KPFM mapping. They follow the relationship $\varphi_s = \varphi_{tip} - EV_{CPD}$. φ_{tip} is usually a given value thus the sample work function φ_s can be obtained by acquiring the V_{CPD}.

KPFM was conducted on the AFM NanoIR2 platform (Anasys Instrument, Inc., Santra Barbara, CA) equipped with a KPFM module. KPFM probes (PR-EX-KPFM-5; typical resonant frequency ~55 kHz; Anasys Instrument, Inc.) were used. The sample was grounded and the bias (ΔV) was applied to a conductive AFM cantilever.

Each of the KPFM probe was calibrated to determine the work function. Calibration consisted in obtaining a KPFM measurement on a fresh-exfoliated HOPG flake using $\Phi_{HOPG} = \varphi_{tip} - e\ V_{CPD}$, where Φ_{HOPG} is an known value 4.6 +/- 0.1 eV, and V_{CPD} is extracted by averaging the values of the KPFM map. For each kind of supercapacitor sample (before and after cycling), at least 3 sets of samples were characterized. On each sample, at least 3 positions were selected to justify the repeatability of the results.

2.3.3 Results and Discussion

Figure 2-12 shows the topography (Figure 2-12 (a-d)) and corresponding contact potential difference maps for WO_3/WS_2 electrode (Figure 2-12 (e) and (f)) before (left column) and after electrochemical cycling (right column). A careful comparison of electrode material surface morphology reveals a large increase in grain size from few hundred nanometers before cycling, to micrometer sizes after cycling. In addition, the average V_{CPD} increased from 0.052V to 0.12V after cycling.

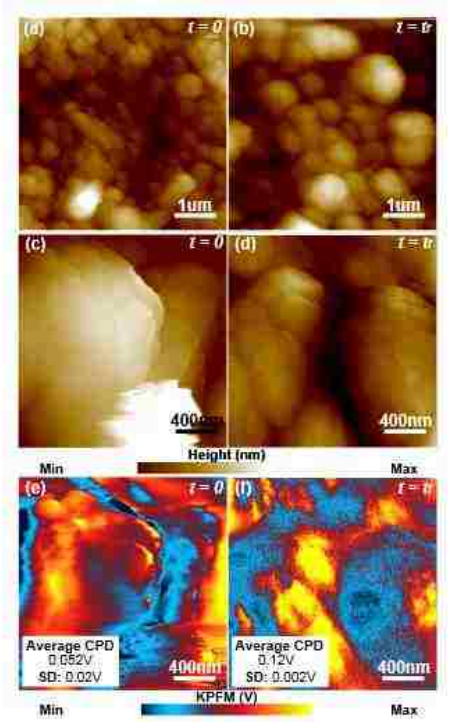

Figure 2–12 AFM topography of the WO_3/WS_2 electrode before (a, c) and after cycling (b, d). (e,f) KPFM maps of the same region presented in (c, d). The average V_{CPD} is indicated on each image.

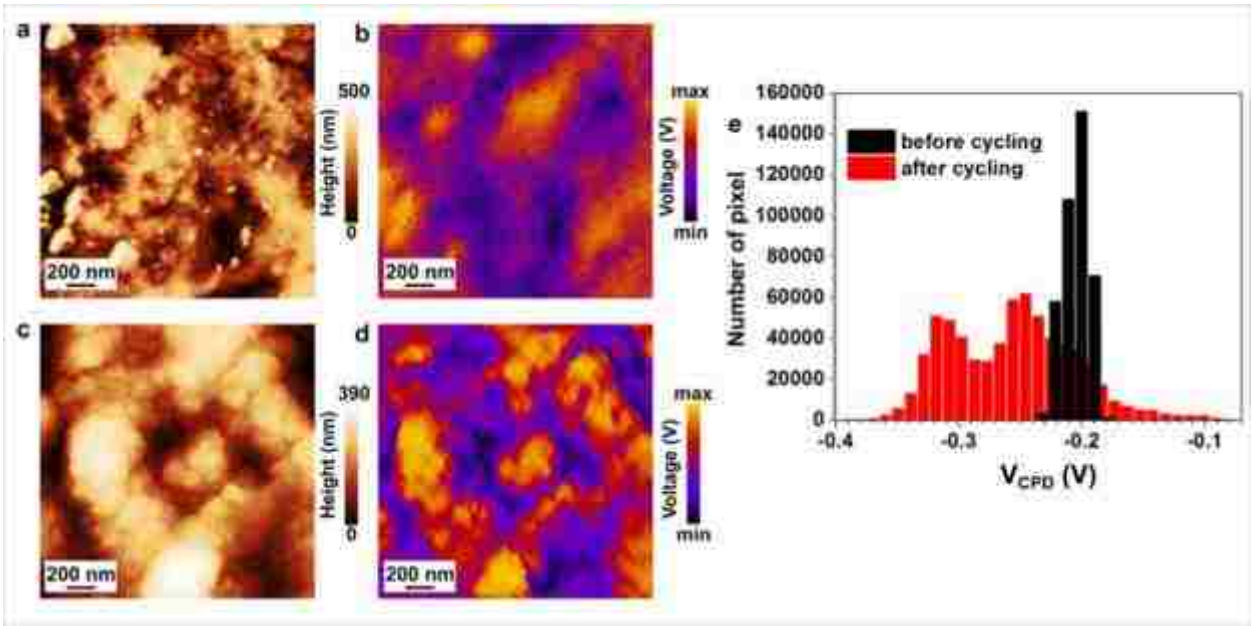

Figure 2–13 AFM morphology (a) and V_{CPD} values measured by KPFM (b) for RGO before cycling. (c, d) corresponding AFM morphology (c) and KPFM (d) after cycling. (e) Histogram of measured V_{CPD} values for RGO before and after cycling

Figure 2-13 shows the topography (Figure 2-13 (a) and (c)) and corresponding contact potential difference maps for the collected flakes (Figure 2-13 (b) and (d)) before (top) and after electrochemical cycling (bottom). A careful comparison of electrode material surface morphology reveals the increased grain size for the material after cycling. In addition, the histogram (Figure 2-13 (e)) indicates an overall decrease of the V_{CPD} after cycling with a mean V_{DC} around -0.25 V before cycling compared to the mean around -0.21 V prior to cycling. The broad distribution of the histogram (from -0.35 V to -0.1 V) after cycling indicates that a number of regions remained unaffected by the cycling, which could not readily be determined from the images. The images with lowest V_{DC} did not seem to match with any particular consistent topographical feature.

We note that the KPFM configuration used in our system is mostly suitable for qualitative evaluations of the work function.

2.4 Conclusions

With KPFM measurements here, although semi-qualitative, we have demonstrated that nanoscale measurements can be used to monitor key parameters of the evolution of the electrodes which will affect the performance of the device over time. We emphasize here that single point or single area measurements in this line of work may provide erroneous results, and great care should be taken to acquire datasets that will be statistically representative of the device. In addition, the visualization of the KPFM images alone does not suffice to extract usable information. Extracting the V_{CPD} in forms of histograms, bar plots or mean value switch standard variations is more useful to establish connections to the device performance. Nonetheless the nanoscale maps can inform on the changes in grain sizes and the distribution of the changes in work function across the electrodes to eventually identify regions where the decays are predominant.

2.5 Summary and Future Perspectives

In this chapter, we presented a selection of work we have carried out using AFM-based advanced imaging and spectroscopic methods (pc-AFM, PFM, MSAFM and KPFM) to deepen the understanding of the influence of electrical, opto-electrical and chemical properties of the materials used in energy harvesting and storage on the performance of the corresponding devices. Revealing the fundamental processing-structure-property relationships is of great importance to identify the underlying mechanism(s) that ultimately determine device performance. We envision that the high resolution functional imaging and spectroscopy has the potential to revolutionize the current understanding of the materials and devices if explored to its

full potential. The capabilities could also accelerate the optimization of materials synthesis and processing to achieve the performance requirements for the next-generation energy harvesting and storage devices.

In addition, we would also like to provide an outlook on how the current understanding can be strengthened by including other existing AFM-based methods or by developing new modules tailored for the scientific questions under investigation.

For energy harvesting materials, as discussed by our case study on organic solar cell device material, pc-AFM is a powerful tool to elucidate dark currents and photocurrents in traveling through the material. While this is a great and versatile platform to directly extract current generated from the energy harvesting material much care should be taken during characterization. Environmental control should be in place to slow down the humidity-induced and oxidation-induced degradation of the devices. The force applied to the sample surface by the AFM cantilever tip should be large enough to allow the good tip-sample contact, but a strong contact could also damage the conductive coating of the probe rapidly, introducing major variations in the signals collected

For materials used for energy storage devices, current KPFM can provide a qualitative to quantitative aspect of the work function of the electrode materials, and the evolution through cycling. Great care should be taken to allow repeatable and reliable measurements – *a single point measurement is not appropriate*. Sample preparation requirements may vary from one type of device to the next, but development of sample preparation protocols are critical. This can be pretty challenging for devices such as supercapacitors that are fabricated using complex material

networks. During KPFM measurement, environmental control chamber is required to control the humidity as humidity can impede the reliability of the measurements.

We foresee the development of AFM systems to allow the *in situ* characterization of morphology, electrical and electrochemical properties of energy storage materials. To achieve this, environmental cells that would enable *in situ* cycling is required to achieve a characterization of materials' response close to the real device. We also envision that the current understanding can be further improved by the implementation of AFM based platforms which would be capable of getting correlative chemical and electrical maps simultaneously and by the implementation time-resolved nanoscale measurements to advance the understanding the materials' dynamic responses upon excitation, or over time. Time-resolved AFM measurements are in fact a very active area of research currently.

3 SPECTROSCOPY IN CATALYSIS DEVELOPMENT

3.1 Background

Related to the need for cleaner energy described in Chapter 2, recent alarming calls from the scientific community warn against the repercussions of our current contributions to global climate change and atmospheric warming. These evolving global environmental conditions lead to the relentless rise of greenhouse gas CO_2. They cause serious concerns for sustainable energy, food and water production, as well as for human health and environmental pollution. In fact, the atmospheric CO_2 concentration has surpassed 400 ppm in 2013, which is the highest this level has ever been in the past 400,000 years [64]. In order to achieve the long term goal of building and developing a sustainable society, a recent "Lima call for climate action" [65] emphasizes the importance of achieving near-zero or even negative anthropogenic CO_2 emission by the end of this century. In considering science-driven solutions to respond to this, the valorization of the abundant CO_2 gas is receiving great attention in the political, industrial, scientific and technological societies. With CO_2 no longer being considered as a waste product, but rather as an alternative carbon feedstock to produce fuels renewable or as a reagent to form molecules with high commercial values, the opportunities to replace fossil fuels in a sustainable scheme are becoming exciting.

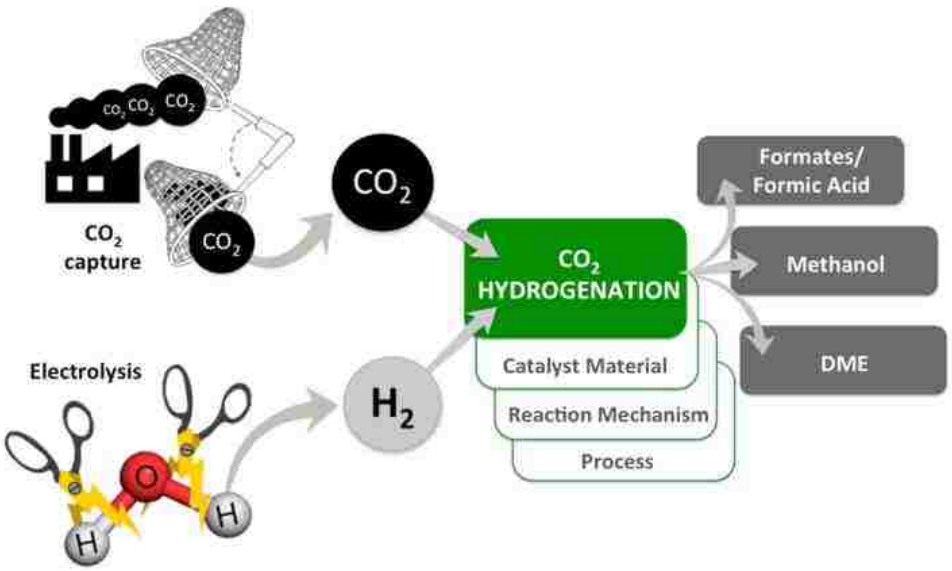

Figure 3–1 CO_2 hydrogenation process with an example of added value by-products formation [66]

3.1.1 Better catalyst

The development of nanotechnology has accelerated the design, modeling and synthesis of a new generation of functional nanomaterials [67]. To achieve sustainability, catalysts with higher activity and selectivity are desired [68]. Especially for heterogeneous catalysis, recent studies have shown that the catalytic activity and selectivity can be affected by atomic or molecular level of structural changes.

3.1.2 h-BN as heterogeneous catalyst

Hexagonal boron nitride (*h*-BN) has long been used in applications requiring dry lubricants. In addition, its excellent electrical resistivity (with a dielectric strength of 80 $kV.mm^{-1}$), high thermal conductivity (71 $W.m^{-1}.K^{-1}$) and low thermal expansion (less than $1x10^{-6}$ K^{-1}) have made it a material of choice in industrial processes, such as for supports and cells used in chambers for high temperature materials growth [69] or for large scale exothermic reactions [70].

Remarkably, a recent body of work overhauls the conventional outlook on *h*-BN by suggesting that atomic arrangements in individual layers can be engineered to introduce a new generation of versatile catalysts [71-75]. This application has long been overlooked, partly due to the high chemical and thermal stability [69] together with the wide band gap of *h*-BN, estimated to be between 3.6 [76] to 7.1 eV [77]. Instead, immediate applications of *h*-BN monolayers following the advent of two-dimensional (2D) materials have been in providing atomically thin and flexible insulating layers for nanoelectronics [78] and far-ultraviolet sources for optoelectronics [79]. However at this time, all fields are converging toward the need for a deeper understanding of defects [80-82], their formation and their effects on 2D materials properties, to reach more prevailing rules for material design in the foreseeable future.

Boron and nitrogen vacancies, together with Stone-Wales (SW) defects have been shown to be the most common defects found in individual *h*-BN layers [71,83], beside edge defects. In multi-layered materials or heterostructures stacking becomes another distinction that has to be taken into account [84]. All can significantly impact the optical [85], electrical and magnetic properties of *h*-BN [82]. In addition, doping or impurities in place of the defects have led to interesting properties [83]. However, the characterization of the nature of the defects remains challenging [83]. Secondary ion mass spectrometry (SIMS) can provide some insight on the carbon and oxygen content but the association to a particular defect is not straightforward [83]. Nanoscale imaging techniques including scanning probe microscopy and transmission electron microscopy (TEM) have revealed the presence of defects, in particular vacancies, but the incident beam such as in TEM could itself affect the nature of the defects. X-ray spectroscopy, electron energy loss spectroscopy and electron-paramagnetic resonance (EPR)[82] can also provide complementary information regarding the nature of the defects and the bond energies resulting from the presence

of defects or impurities. Overall, this exercise remains challenging.

It has now been confirmed that defect-laden *h*-BN (*dh*-BN) can facilitate hydrogenation and olefin bond activation [71,86]. The experimental findings and conceptual predictions have been supplemented by density function theory (DFT) calculations. The results show that the olefin bond are more likely to be activated over four types of defect sites in *h*-BN: boron substitution for nitrogen (B_N), nitrogen (V_N) or boron (V_B) vacancies, and Stone–Wales (SW) defects [71]. Subsequent solid-state NMR experiments identified nitrogen vacancies as the most probable active sites for olefin hydrogenation [71]. Hence, the effect of introducing defects in *h*-BN, taking the form of *dh*-BN, in view of forming a new metal-free heterogeneous catalytic candidate should be investigated further.

Furthermore, to date, the specific defects created and their role in the reactions have mostly been examined locally through gas chromatography–mass spectrometry (GC-MS) analysis, solid state Nuclear magnetic resonance (NMR), and supported by quantitative measurements of binding energies such as with X-ray Photoelectron Spectra (XPS) and DFT calculations [71]. In other 2D materials, Raman spectroscopy has been a powerful tool for identifying defects, particularly in graphene due to the disorder related D band [87]. In MoS_2, defects have been identified using the LA (M) band at ~ 227 cm^{-1}. LA(M) originates from the first-order Raman mode due to the LA phonons at the M point in the Brillouin zone [88,89]. The apparition of oxidation signs in the form of MoO_3 has also been used as an indicator of defect creation [89].

In *h*-BN, identifying defect-induced properties is more challenging [90]. While scanning tunnelling microscopy (STM) and TEM an offer high resolution images of the atomic defects in 2D materials [91,92], the requirement to deposit *h*-BN on a non-metallic substrate to study its metal-free

catalytic properties makes it impractical for STM imaging. TEM is also challenging due to the thickness of the flakes in the powders used for ball-milling (sometimes greater than 50 layers). Thus, identifying defects in *dh*-BN to establish correlations with its catalytic properties is quite challenging for samples obtained from a large scale reactor, such as powders obtained from mechanochemistry. However, comparing the effect of these defects on the reactivity of the formed *dh*-BN powders can provide valuable information for process optimization.

3.2 Motivation

Motivated by the potential of *dh*-BN as a heterogeneous catalyst and driven by the need to better understand the role defects play during the catalytic reactions, we investigate in this chapter the effect of defects introduced in pristine *h*-BN samples through various defect creation methods. Three case studies, focusing on the defect formation for catalytic activities, are reported as follows. We note that in all case studies, the ball milling and mass uptake measurements were carried out by our collaborator, Dr. Blair and his group.

In **case study One**, we consider the effect of ball milling and heat treatment the formation of defects in layered hexagonal boron nitride (*h*-BN). Using ball milling, the defects formed have been assigned as active sites for catalysis for the hydrogenation and activation of olefin bonds. Here, we compare the lattice changes introduced by ball milling and by heat treatment in *h*-BN. We show how the material properties can be modified by varying the treatment conditions. We evaluate the effect of milling conditions on the mass uptake of the *dh*-BN after pressurization with propene and CO_2. Our results highlight how high-resolution imaging, infrared spectroscopy and time-of-flight mass spectroscopy can be exploited to assess the potential catalytic activity of *dh*-BN for heterogeneous catalysis.

In **case study Two**, we conduct a comprehensive study to compare the effectiveness of different ball milling media in the introduction of defects in *h*-BN.

In **case study Three**, we investigate the effect of ball milling induced defects and subsequent reactions with oxygen and propene molecules on the *h*-BN signatures in Raman, infrared and fluorescence spectroscopies. Our results indicate that the comprehensive spectroscopic study can serve as an indirect measure for defect characterization. We also highlight how time dependent fluorescence intensity spectra can reveal the density of defects and the kinetics of reaction of the defects with molecules of interest in the catalytic studies.

3.3 Case Study One: Defect engineering in h-BN powder samples and subsequent property characterization for catalytic applications

Here we consider the effect of ball milling and heat treatment on the formation of defects laden hexagonal boron nitride (*dh*-BN). The ball milled and heat treated *dh*-BN are termed as BM-*dh*-BN and HT-*dh*-BN, respectively.

Ball milling is a commonly used top-down approach to produce nanomaterials or to facilitate chemical reactions in the absence of solvents [93,94]. This has been described for numerous applications including the realization of heterogeneous catalytic CO oxidation over metal oxide catalysts, such as NiO and Cr_2O_3, [93,95] and non-metal catalyst, such as *h*-BN [71]. During ball milling, the flakes are mechanically exfoliated into thinner layers and reduced to smaller flakes through comminution, therefore increasing the surface area of the catalytic material [71,96,97]. Furthermore, it has been demonstrated that ball milling can introduce different types of defects, including edge defects and stacking disorder into *h*-BN flakes [64,98]. The nature and the density of defects may be controlled by varying operating parameters, i.e., milling intensity, duration and

media composition. Nash et al. [71] further demonstrated that *dh*-BN produced through high energy ball milling can be utilized as a catalyst suitable for the hydrogenation of olefins in bulk-scale chemical experiments. Heat treatment, also known as thermal annealing, has been employed to introduce defects in 2D materials. Lattice point defects (vacancies) and/or cracks can be introduced depending on the heat treatment conditions [99-101]. It has been reported that heat treatment at sub-decomposition temperatures can introduce anion vacancies in 2D materials such as MoS_2, $MoSe_2$, and WSe_2 and the density of induced vacancies can be tuned by using different heat treatment temperatures. But the application of heat treatment in defect creation in *h*-BN has not been explored at all.

3.3.1 Methods

3.3.1.1 Sample preparation

The pristine *h*-BN powder was obtained from Saint-Gobain Ceramic Materials (Grade PCTF5). To remove moisture, the powder was dried at 180 ˚C in vacuum overnight before transferring to a glovebox filled with argon for ball milling.

3.3.1.2 Ball milling for defect introduction

Ball milling was employed for flake size reduction and defect creation. Zirconia was used as milling media and vials (ZrO_2, 12.7 mm in diameter, approximately 5.97 g in weight). For each treatment, 3 g of dry *h*-BN powder were sealed in a 65 mL milling vial and four milling balls were employed to supply kinetic energy. After sealing the vial, the powder was processed with a mixer/mill (8000M SPEX CertiPrep). The powders were milled for 30 min, 60 min, 90 min and 120 min. After milling, the *dh*-BN powder was stored in the glovebox until characterization.

Upon transfer for spectroscopy measurements, the powder was sealed in a custom-made contained to minimize exposure to air before characterization.

3.3.1.3 Heat treatment for defect introduction

Heat treatments were initially conducted in air in a Thermolyne Small Benchtop Muffle Furnace (Type 1400, Thermo Scientific) for optimization. The parameters identified for defect creation were used to recreate the treatment in controlled environment under glovebox conditions filled with argon. In both cases, pristine *h*-BN flakes from Saint-Gobain Ceramic Materials (Grade PCTF5) were transferred into the furnace, after the temperature was stabilized. At the end of the treatment, the samples were rapidly taken out from the furnace for fast cooling (or quenching) to room temperature. The detailed parameters used for heat treatment are listed in Table 3-3.

3.3.1.4 Structural property characterization

Structural property characterization of pristine *h*-BN, BM-*dh*-BN and HT-*dh*-BN were characterized by SEM in order to evaluate the defects introduced inside the material and determine the effectiveness of defect introduction through ball milling and heat treatment.

Scanning electron microscopy (SEM): The morphology of *h*-BN and *dh*-BN powders, including shape and size, were studied using SEM equipped with a field emission gun (Zeiss ULTRA-55 FEG), all SEM images were acquired using secondary electrons. For each powder sample, 0.1 g powder was first dissolve in 5 mL water. The solution was then drop-casted on the surface of silicon wafer. To avoid charging problems during SEM characterization, the samples were coated with a thin layer of conductive gold-palladium via a sputtering coater. The working

distance for the secondary detector was 5.7 mm, the beam energy was 5 kV and the electromagnetic lens aperture of 20 μm.

X-ray diffraction (XRD): The crystalline structure of *h*-BN and *dh*-BN powders were studied using XRD (PANalytical Empyrean Multi-Purpose X-Ray Diffractometer) using a copper source (Cu Kα = 1.5405 Å). Diffractograms were collected from 10 to 90° 2θ using 0.05° steps.

3.3.1.5 Elemental and chemical characterization

Raman spectroscopy: Raman spectra were acquired by using a confocal Raman microscope (WITec Alpha 300RA) with a 532 nm laser excitation. Raman spectra were collected with a 50X objective lens (Zeiss, numerical aperture of 0.7) and a spectrometer with an 1800 lines/mm grating, evaluated to provide a 0.9 cm^{-1} spectral resolution. For all spectra acquired, settings were maintained at laser power of 5.7 mW and integration time of 1 s. Raman spectra from pristine *h*-BN powder and heat-treated *dh*-BN powder prepared outside of the glovebox were acquired in air. Ball milled *dh*-BN and heat-treated *dh*-BN powders prepared in the glovebox were sealed in a custom-made chamber with a sapphire window (transparent for Raman measurements) inside the glovebox to prevent exposure to ambient conditions (H_2O, O_2, N_2, and CO_2).

Fourier transformed infrared spectroscopy (FTIR): FTIR spectra were acquired in air, immediately after opening the sealed powder container. The PerkinElmer FTIR spectrometer (Perkin Elmer Corp, Spectrum 100 series) used for the measurements was equipped with an attenuated total reflection (ATR) sampling accessory unit with a single reflection diamond/ZnSe crystal plate. Because of the properties of the ATR windows, the wavelength range was restricted to 4000-650 cm^{-1}. The spectral resolution was set to 4 cm^{-1} with iris aperture of 8.9 mm for all measurements. Four scans were collected and averaged for each powder sample.

3.3.1.6 Catalytic property characterization

Gas exposure and mass uptakes: *dh*-BN powders from ball milling and heat treatment were pressurized with CO_2 or propene (C_3H_6) molecules and respective mass uptakes were determined. An initial measurement of the sample mass was obtained in the glovebox under argon before the sample was placed in a pressure cell for exposure to propene (40 PSI of propene for a minimum of 48 h). The mass of the pressurized dh-BN was then recorded.

Time-of-flight secondary ion mass spectroscopy (ToF-SIMS): Samples for ToF-SIMS measurements were prepared at UCF. Pellets of ball milled *dh*-BN powder before and after CO_2 exposure were prepared using a pellet maker inside a glovebox. The pellets were about 8 mm in diameter and 3 mm in height. All pellets were sealed individually inside a glass container during transportation.

ToF-SIMS measurements were conducted at The Center for Nanophase Materials Sciences at Oak Ridge National Laboratory. ToF-SIMS spectra for ball milled *dh*-BN powder before and after CO_2 exposure were performed in negative ions detection mode using a TOF-SIMS 5 instrument (ION-TOF GmbH, Germany) equipped with a Bi liquid metal ion gun (LMIG) as the primary ion source delivering Bi^{3+} ion clusters onto sample surfaces. The vacuum level of the chamber was maintained at ~ 5×10^{-9} mbar during the measurements. The primary ion clusters bombarded sample surfaces at an accident angel of 45˚ with a kinetic energy of 30 keV. Secondary ions were accelerated and collected though a time-of-flight analyser. A low energy electron flood gun was employed to neutralize sample surface charges. In order to eliminate the contribution of potential surface contamination due to sample exposure to air during the loading process, the top surface of the pellet was removed and depth profiling was conducted using a Ar^+ gas cluster ion-sputtering source (GCIS) operated at 10 eV and 5.7 nA. The sputter beam was

scanned over a 600×600 μm^2. For data acquisition, the depth profiling was performed across an area of 300×300 μm^2 scan size with a resolution of 256×256 points.

3.3.2 Results and Discussion

3.3.2.1 Size, shape and dimensions

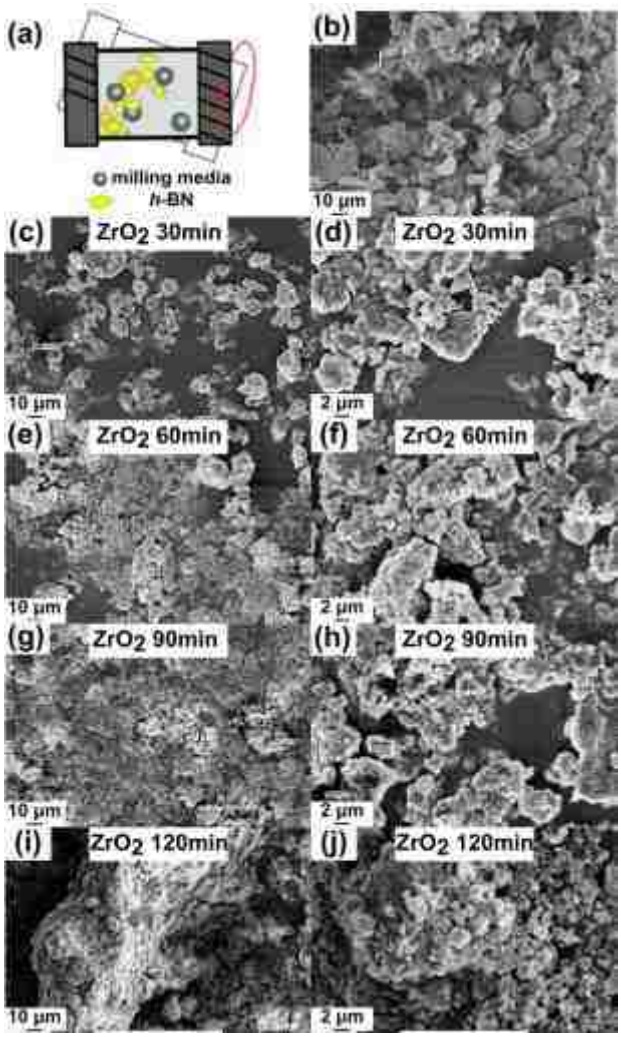

Figure 3–2 (a) Illustration of formation of *dh*-BN from pristine *h*-BN through ball milling, (b) SEM image of pristine *h*-BN flakes, (c-j) SEM image of *dh*-BN flakes after ball milling with ZrO_2 balls for 30 min (c, d), 60 min (e, f), 90 min (g, h), and 120 min (i, j). The SEM images presented in the right column correspond to a zoom of the images in the left column.

Table 3-1 Summary of the flake size distribution percentage for the different ball-milled *dh*-BN powders

	>5 μm	2-5 μm	<2 μm
ZrO_2 30 min	**17.9**	**52.2**	**29.9**
ZrO_2 60 min	**12.2**	**76.4**	**11.4**
ZrO_2 90 min	**13.5**	**18.9**	**67.6**
ZrO_2 120 min	**0**	**15.8**	**84.2**
WC 120 min	**4.8**	**47.6**	**47.6**

We first investigated the effect of ball milling on the properties of *h*-BN. The morphology of the BN powders was studied using SEM to understand the effectiveness of ball milling in terms of exfoliation and size reduction of the flakes. The morphology of the pristine *h*-BN flakes and the resulting *dh*-BN after ball milling are presented in Figure 3-2 (b) and (c-l), respectively. Analysis of the SEM images suggests that before treatment, the flakes were ~ 6-10 μm in size, in agreement with the product specification sheet (mean value of diameter: ~7 μm). The pristine flakes exhibited irregular edges but smooth surfaces and few folds. After 30 min of milling with the ZrO_2 media, SEM images reveal flakes with smaller dimensions though large and intact flakes could still be observed (Figure 3-2 (c, d)). This is attributed to the high-energy impact between the flakes, the milling balls and the vial walls during the treatment. As can be seen in Table 3-1, after the first 30 min, the large pristine flakes were mostly fragmented with flakes lateral dimensions in the 2-5 μm range. The number of 2-5 μm flakes increased until 60 min of treatment (Figure 3-2 (e, f)). After 90 min and 120 min, the dimensions decreased further, with a large number falling below 2 μm (Figure 3-2 (g-j)). The SEM images also show that after 120 min of ball milling, the lateral dimensions and thickness of the flakes decreased dramatically to nano-sized flakes and a significant agglomeration of the smaller flakes could be observed, which is in agreement with prior findings by Torii et al. [102]. As a result, the percentage of edge defects

in the volume of powder in the reactor increased for the first 120 min of milling with ZrO_2.

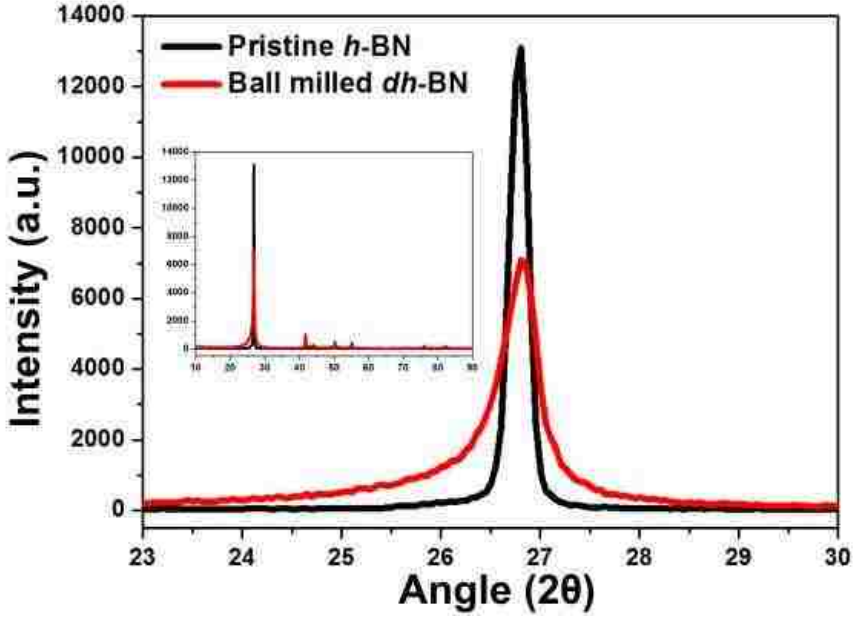

Figure 3–3 Zoomed in XRD spectra of pristine *h*-BN (black) and ball milled *dh*-BN (red) powders. The inset provides the XRD spectra with the 2θ ranging from 10 to 90°.

Powder XRD spectra were also acquired to evaluate the effect of ball milling on the crystalline structure of *h*-BN. As shown in Figure 3-3, a XRD peak at the 26.8 ˚ was identified as the (002) diffraction peak of h-BN [71]. The broadening as well as the peak shape changing from symmetric to asymmetric indicated a decrease in the crystallinity order inside *dh*-BN powder, as well as an increased inter-plane spacing for a fraction of the *dh*-BN powder after ball milling.

3.3.2.2 Elemental and chemical properties characterization

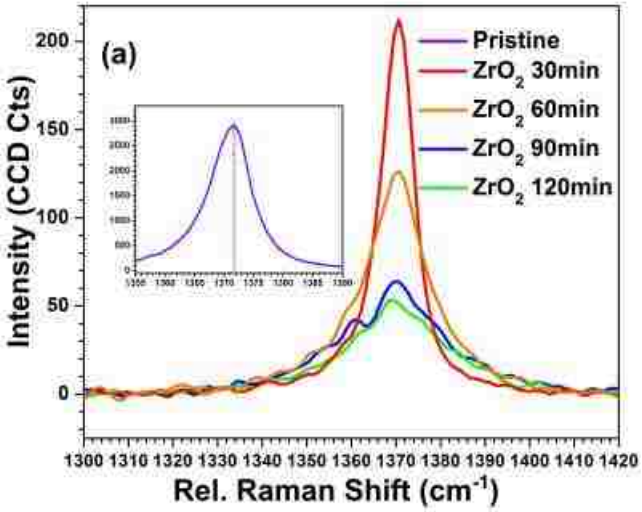

(b)

Sample	Position (cm^{-1})	FWHM (cm^{-1})
Pristine	1371	8.0
ZrO_2 30min	1370	8.5
ZrO_2 60min	1370	16.6
ZrO_2 90min	1370	24.6
ZrO_2 120min	1370	24.5

Figure 3–4 (a) Raman spectra exhibiting the E_{2g} band ~1370 cm^{-1} of pristine *h*-BN (purple in inset) and *dh*-BN after ball milling with ZrO_2 for 30 min (red), 60 min (orange), 90 min (blue), 120 min (green). (b) Table summarizing the position and FWHM of the E_{2g} band in ball-milled *h*-BN obtained with different durations of treatments with ZrO_2 milling balls.

For all *dh*-BN powders considered in Figure 3-2, the Raman and mid-infrared fingerprints of *h*-BN were collected. As both spectroscopies constitute measures of the molecular vibrations of chemical bonds in the material, the energy of the B-N lattice vibration likely holds some information on the density and types of defects present in the flakes. Raman spectra of the *h*-BN and *dh*-BN powders collected for the different durations of milling are presented in Figure 3-4. The positions and full width at half maximum (FWHM) of the BN mode at 1371 cm^{-1} were extracted using a Lorentz fit. A summary of the values is provided in Figure 3-4 (b). The band at 1371 cm^{-1} corresponds to the E_{2g} phonon vibrational mode originating from the in-plane vibration of B and N atoms in opposite directions [90]. After the first 30 min of ball milling, a large

decrease of the band intensity and broadening were apparent. Extending the ball milling process intensified this effect. This can be attributed to the disorder introduced along the basal plane as the flakes get smaller. A slight red shift of the E_{2g} band from 1371 cm^{-1} for pristine *h*-BN powder to 1370 cm^{-1} was observed within the first 30 min of ball milling. No further peak shift was measured despite the confinement of flake size as the milling duration increased from 30 min to 120 min. Similar strain-induced red shifts of the analogous Raman G mode in graphene have previously been observed [87,92]. Based on these, we attribute the shift in *dh*-BN to the strain induced upon initial ball milling. FWHM exhibited a stronger dependence on milling duration as it increased gradually from 8.0 cm^{-1} to 8.5 cm^{-1} after 30 min of treatment, and reached 24.5 cm^{-1} after 90 min. It remained constant for longer treatments. This significant increase in FWHM can be attributed to a complex contribution from both the increase in the strain or defect density inside the material with stronger surface scattering and the distribution of *dh*-BN clusters with different dimensions compared to the pristine *h*-BN flakes [78].

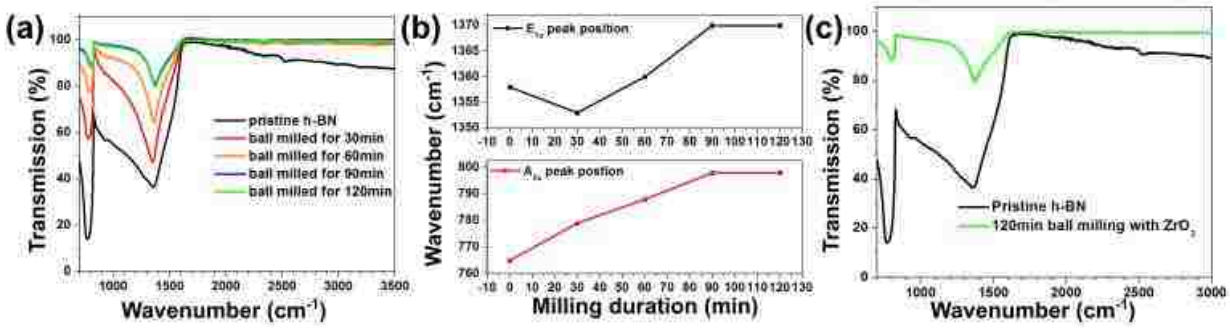

Figure 3–5 (a) FTIR spectra of *h*-BN and *dh*-BN obtained for milling times of 30 min, 60 min, 90 min, and 120 min with ZrO_2. (b) Evolution of E_{1u} (top, black) and A_{2u} (bottom, red) IR bands as a function of milling duration. (c) FTIR spectra of *h*-BN and *dh*-BN obtained after ball milling for 120 min with ZrO_2 (green) milling balls.

Table 3-2 Absorption (A_{2u})/ Absorption (E_{1u}) ratio in the IR spectrum of pristine *h*-BN and ball milled *dh*-BN

	Absorption(A_{2u})/ Absorption(E_{1u})
Pristine	**1.36**
ZrO_2 30 min	**0.81**
ZrO_2 60 min	**0.58**
ZrO_2 90 min	**0.55**
ZrO_2 120 min	**0.55**

Next, we compared the IR fingerprint of the *h*-BN powders obtained with FTIR spectroscopy (Figure 3-5). *h*-BN exhibits two primary bands around 763 cm^{-1} and 1358 cm^{-1}. The vibrational mode near 763 cm^{-1} corresponds to A_{2u} out-of-plane bending vibration of B-N-B, while the peak near 1358 cm^{-1} represents the E_{1u} in-plane stretching vibration of the B-N bond [103,104]. In addition, we note small bands around 2342 and 2542 cm^{-1} for pristine the *h*-BN powder. These have previously been attributed to small molecules and impurities adsorbed on the pristine *h*-BN in air [105,106]. The first 30 min of ball milling seemed to remove contamination as the bands above 2000 cm^{-1} disappeared and the E_{1u} in-plane stretching band became narrower. Another weak band around 925 cm^{-1}, previously reported [107] as a B-O or B-N-O stretching mode in pristine BN [107,108], disappeared after 30 min of ball milling. This indicates that some oxidation of *h*-BN or oxygen adsorption may take place in storage, but can be reversed by ball milling. This is in agreement with the induction period, i.e., the time required for *h*-BN to be processed in the ball milling reactor before any catalytic activity can take place, which has been observed in our measurements.

After increasing ball milling treatment durations, the intensities of the two *h*-BN characteristic bands were found to decrease. The quantity of powder and the force applied on the ATR crystal were maintained constant for all measurements. Based on our XRD data shown in Figure 3-3, we

attribute the smaller IR band intensities to the reduction in size of the BN flakes, leading to smaller crystalline regions to absorb light.

Another interesting phenomenon is that the ratio of Absorption($_{A2u}$)/ Absorption($_{E1u}$) was only above 1(1.36) for pristine *h*-BN and continuously decreased from 0.81 at 30 min ball milling to 0.55 as 90 min and 120 min (Table 3-2). This may suggest that the out-of-plane bending vibrations decreased as the exfoliation of the flakes progressed. Next, we considered the position of the two bands. As shown in Figure 3-5 (b), the two bands shifted to higher wavenumber with increasing milling duration. For the A_{2u} peak, the position moved from 765 cm^{-1} for pristine *h*-BN to 779 cm^{-1} after 30 min milling before reaching a maximum at 798 cm^{-1} after 90 min milling. Similarly, the position of the E_{1u} band shifted from 1358 cm^{-1} to 1370 cm^{-1} as the milling time increased from 0 to 90 min. No additional changes were found between 90 min and 120 min. Lastly, we compared the effect of milling with ZrO_2 balls for 120 min on the IR fingerprint of the *dh*-BN powder (Figure 3-5 (c)). We found that the position changes of the A_{2u} and E_{1u} bands were not significant given the 4 cm^{-1} resolution of FTIR system. The results suggest that after 120 min of milling using the ZrO_2 media the conditions were maximal for uptake. This is in agreement with a previous study by Torii et al. [102] in which the surface area available after longer ball milling was found to decrease beyond a threshold, as aggregation of the small flakes became predominant.

3.3.2.3 Catalytic properties characterization

The catalytic performance was evaluated on pellet samples made from *dh*-BN powder before and after CO_2 gas exposure. Ball milled *dh*-BN power was investigated by ToF-SIMS measurement. By sputtering conducted inside ToF-SIMS chamber, superficial layers of materials on top of the

pellets were removed since they were more subject to contamination during sample storage, transportation and loading. The spectra were then acquired. Peaks only present on CO_2 exposed *dh*-BN sample were selected as peak of interest for their identifications. The results are plotted in Figure 3-6. The results seem to confirm a huge increase in the amount of C-H bonds, as well as the increase of alcoholic of carboxylic acid molecules on *dh*-BN powder after CO_2 gas molecule exposure, while as the amount of the aforementioned molecules was much less on *dh*-BN without CO_2 gas exposure. Since the possibility of surface contamination contribution was excluded, here we think those detected molecule fragments most likely belong to those molecules produced from the catalytic reactions on defect sites, which seem to be very promising.

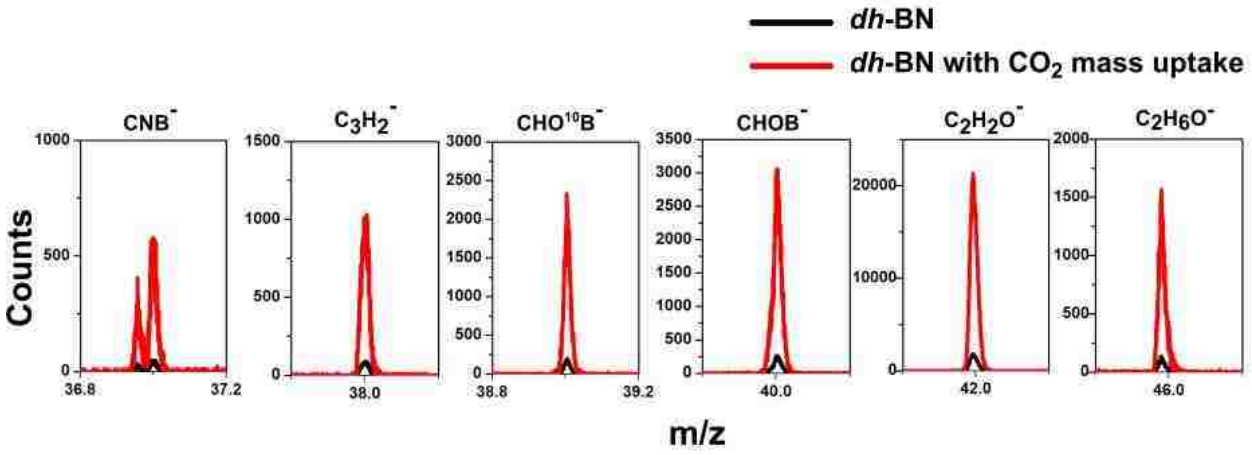

Figure 3–6 Averaged mass spectra extracted from ball milled dh-BN before (black) and after (red) CO_2 gas molecule update

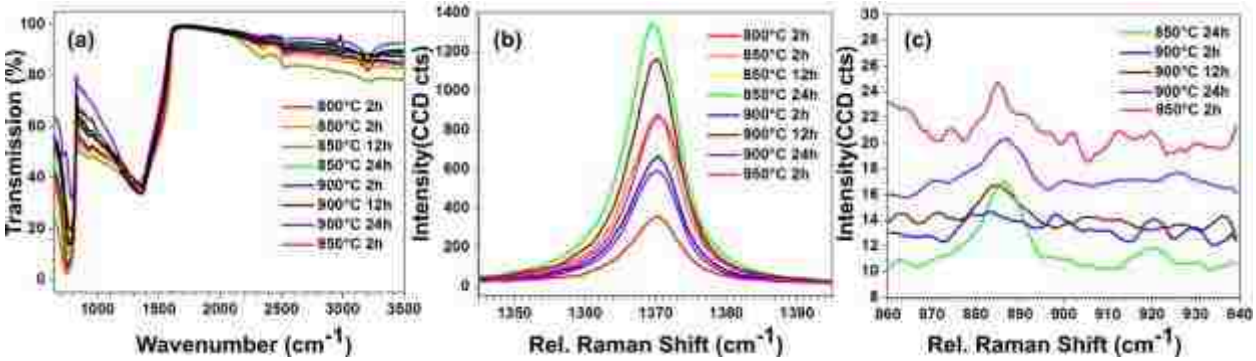

Figure 3–7 Effect of heat treatment on *h*-BN powders (a) FTIR spectra of BN powders heat treated at different conditions: 800˚C for 2 h (red), 850˚C for 2 h (orange), 850˚C for 12 h (green), 850˚C for 24 h (light green), 900˚C for 2 h (blue), 900˚C for 12 h (brown), 900˚C for 24 h (purple), 950˚C for 2 h (pink), (b) Corresponding Raman spectra representing the E_{2g} mode Raman peak of the heat treated BN powders (c) Raman band corresponding to the B-O bond for oxidized BN powder around 885 cm^{-1}.

Table 3-3 Summary of the position and FWHM of the E_{2g} band in heat treated *dh*-BN

Sample	Position (cm^{-1})	FWHM (cm^{-1})
800˚C 2 h	**1371**	**8.2**
850˚C 2 h	**1371**	**8.4**
850˚C 12 h	**1371**	**8.3**
850˚C 24 h	**1371**	**8.3**
900˚C 2 h	**1371**	**8.4**
900˚C 12 h	**1371**	**7.9**
900˚C 24 h	**1371**	**8.1**
950˚C 2 h	**1371**	**8.4**

The effect of heat treatment on *h*-BN was investigated next. As shown in Figure 3-7, no Raman shift or FWHM broadening was observed as a result of treatment in the optimization phase, carried out in air (Table 3-3). This is in agreement with a study by Li et al. [109] in which the Raman E_{2g} band of *h*-BN was left unchanged by heat treatment of bulk material. Based on our SEM images, we estimated the flakes in the powder to be more than 50 layers thick. However,

for powders heat treated with 850˚C for 24 h, 900 ˚C for 12 and 24 h, and 950 ˚C for 2 h, a Raman band centered near 886 cm^{-1} was observed, corresponding to the breathing mode vibration of oxygen atoms within a boroxol ring according to previous reports [110,111]. Based on these observations and various DFT reports [71,82], we infer that the creation of defects, most likely V_N, led to local *h*-BN oxidization into B_2O_3 as a result of the treatment being performed under ambient conditions. After carrying out the measurements in the conditions of defect creation (950˚C for 2 h) in controlled conditions (Argon atmosphere), the Raman signature of the heat treated powder was obtained and indicated no sign of oxidation in the 800 -900 cm^{-1}. The FTIR signatures of the treated *h*-BN flakes exhibited the two bands at around 770 and 1360 cm^{-1} respectively, indicating that the crystal structure remained after heat treatment. This was also confirmed by the SEM image (see Table 3-1). A strong (B-) O - H stretching IR peak near 3200 cm^{-1} [110] appeared for heat treated BN powder treated in air beyond 12 h (850˚C for 12 h, 850˚C for 24 h, 900˚C for 12 h, and 900˚C for 24 h). The powder treated at 900˚C and 950˚C for 2 h exhibited no detectable IR signals from (B-) O - H around 3200 cm^{-1}. However small bands at ~ 925 cm^{-1} and between 2000 – 3000 cm^{-1} previously associated with impurities in the powder [107,108] and, which could be removed with short ball milling, remain on the flake for all heat treated powders. This could have impeded the reactivity of the flakes given our observation of the required induction period to remove impurities in ball milling before reactions can take place.

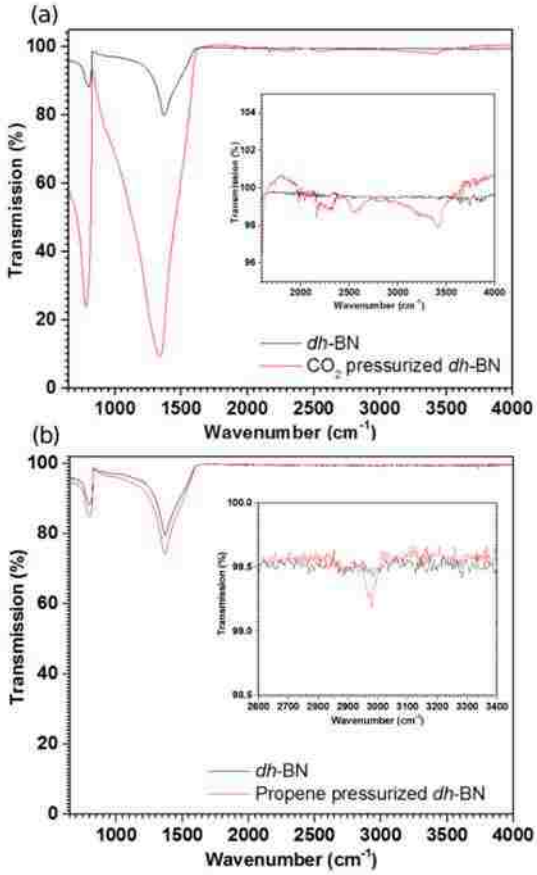

Figure 3–8 FTIR spectra of ball-milled BN powders before (black) and after pressurization for 48 h under 40 PSI (red) in CO_2 (a) and in propene (b). Insets provide details of the IR bands in the 1500-4000 cm^{-1} region.

These results indicate that both treatments affect the vibrational modes of the *h*-BN lattice with signs of defect formation. This is only meaningful if *dh*-BN exhibits catalytic properties for targeted reactions. To evaluate this, we pressurized a representative powder of each treatment, the powder ball-milled with ZrO_2 for 2 h and the powder heat treated at 950 ˚C for 2 h, with molecules of interest. To assess the reaction with olefin, we pressurized the cell at 40 PSI with propene for 48 h, and to study the reaction with CO_2, we pressurized the cell at 40 PSI with CO_2 for 48 h. The largest mass uptake, about 6.8 % increase, was observed for the ball-milled powder

exposed to propene, whereas only a 0.2 % uptake was measured for heat treated powder. After exposure to CO_2, a smaller mass uptake of 3% was found for the ball-milled powder while a 0.4 % uptake was measured for the heat treated powder. The nature of the uptake on the ball-milled flakes was confirmed with FTIR spectroscopy (Figure 3-8). The presence of two bands at ~ 2550 cm^{-1} (B-H stretching) and ~ 3400 cm^{-1} (region for O-H stretch in alcohol R_2CH_2OH or in carboxylic acid R_2COOH) in the CO_2-pressurized *dh*-BN powder (inset in Figure 3-8 (a)) suggested a reaction on the flakes. In addition, the C-H asymmetric stretching mode ~ 2980 cm^{-1} [106], in agreement with the presence of propene or propane, was observed in the propene-pressurized *dh*-BN powder (inset in Figure 3-8 (b)). Neither band was present in the *dh*-BN spectrum acquired prior to placing the powder in the pressure cell. No signal could be detected on the heat treated powders, likely due to the small concentration of molecules.

3.3.3 Conclusions

Ball milling and heat treatment induce different behavior in *h*-BN, likely due to the formation of different defects or density of defects in the flakes. Particularly the microstructure and surface area of the flakes can be controlled by varying the duration of the treatment with ball milling. For heat treatment, varying the temperature and duration of treatment was also found to affect the properties of the flakes. Raman and FTIR spectroscopy can be used to verify the presence of defect, strain induction or oxidation of the sites created, with respect to the conditions of the treatments. For instance, signals from impurities (~ 925 cm^{-1}) could be differentiated from oxidation taking place in the flakes resulting in the stronger band at 3200 cm^{-1}. In addition to deepening the fundamental understanding of processing-structure-property relationship of *h*-BN, our study has practical implications for the induction of catalytic sites in *h*-BN for reaction activation. Initial demonstration of the reactivity of *dh*-BN shows that the reaction is treatment

dependent. The detailed catalytic activity, including the mechanism and the kinetics of the processes taking place after defect induction will be the subject of future studies.

3.4 Case Study Two: Study the effect of different ball milling on the effectiveness of defect creation for CO_2 gas molecule uptake

3.4.1 Background and Motivation

In this case study, with the aim of optimizing the milling efficiency for effective defect creation, we focus on a systematic investigation of the effect of experimental milling conditions (milling time, milling ball material, ball size) on defect creation and subsequent propene mass uptake.

We studied the effect of different mild milling time (from 30 min to 2 h) with ZrO_2 milling on defect creation efficiency in Case Study One. Other parameters such as milling media material, their size and the duration of the milling treatment are expected to affect the density of defects in the system. Zirconia, stainless steel (440C SS) and tungsten carbide (WC) are three widely used materials in commercial milling balls. Previous studies have shown that the properties of flakes/particles milled by different milling media vary, due to the different specific properties (mass, density) of the balls [112]. To identify the most efficient ball milling protocol, we compared the effect of milling parameters on the catalytic properties of the *dh*-BN flakes obtained. We characterized flake morphology and degree of induced disorder after each ball milling treatment. We analyzed subsequent mass uptake after pressurizing the treated powder with propene and CO_2. We also conducted a time-dependent fluorescence study to investigate how different ball milling conditions affect defect creation and subsequent defect-molecule interactions.

3.4.2 Methods

3.4.2.1 Sample preparation

Ball milling was carried out in a mixer/mill (8000M SPEX CertiPrep). The detailed milling parameters considered are listed in Table 3-4. For each treatment, 2 g of dry *h*-BN powder was used. Pressurization and mass uptake measurements were performed with propene, following the procedure described in Section 3.3.

Table 3-4 Ball milling parameters including milling media, milling time, ball size, number of ball used, and resulting mass uptake in propene.

	Identity	**Milling Media**	**Milling Time (h)**	**Ball Size (inch)**	**Ball Number**	**Mass Uptake %**
Group 1-1	1	ZrO_2	4	1/2	4	4.49
	2	ZrO_2	8	1/2	4	4.14
	3	ZrO_2	12	1/2	4	2.30
	4	ZrO_2	16	1/2	4	2.49
Group 1-2	5	ZrO_2	2	1/4	1	2.05
	6	ZrO_2	2	1/2	1	3.64
	7	ZrO_2	2	3/4	1	9.65
Group 2-1	8	440C SS	4	1/2	4	3.49
	9	440C SS	8	1/2	4	2.25
	10	440C SS	12	1/2	4	3.73
	11	440C SS	16	1/2	4	4.67
Group 2-2	12	440C SS	2	1/4	1	4.77
	13	440C SS	2	1/2	1	5.92
	14	440C SS	2	3/4	1	8.17
Group 3	19	WC	2	3/8	1	5.19
	20	WC	2	1/2	1	6.65
	21	WC	2	7/16	1	5.59

3.4.2.2 Sample characterization

Scanning Electron Microscopy: The morphology of milled *dh*-BN powders was characterized by SEM, as described in the previous methods.

Raman spectroscopy: *dh*-BN powders before and after pressurization were characterized using Raman spectroscopy. As discussed in Section 3.3, we have found a correlation between the degree of disorder and the E_{2g} mode (~1371 cm^{-1}) Raman full width at half maximum (FWHM). Raman single spectra were acquired in each sample using the same parameters, on *dh*-BN powders sealed in a customized chamber with Argon environment. For each sample, spectra were collected at a minimum of three positions. The position and FWHM values of the E_{2g} band for each spectrum were extracted using a Lorentz fit. Fitted peak position and FWHM values were then averaged as the representative value for each *dh*-BN powder.

X-ray Fluorescence Spectroscopy (XRF): We used XRF to investigate sample contamination. XRF measurements were carried out on a PANalytical Epsilon 1 Range instrument. The percentage of elements other than B and N were calculated, as well as other elements resulting from contamination. The software was calibrated to get accurate readings when estimating the quantity of each element.

3.4.3 Results and Discussion

3.4.3.1 Ball milling induced contamination

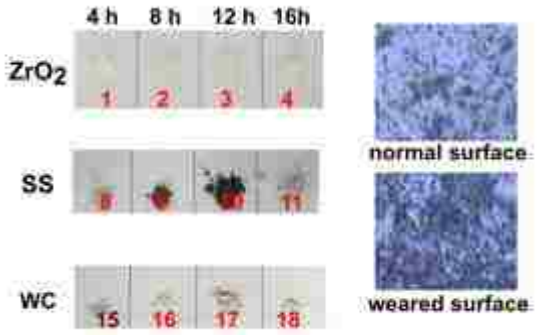

Figure 3–9 Representation of pristine *h*-BN and various *dh*-BN exhibiting color changes after ball milling with different milling parameters.

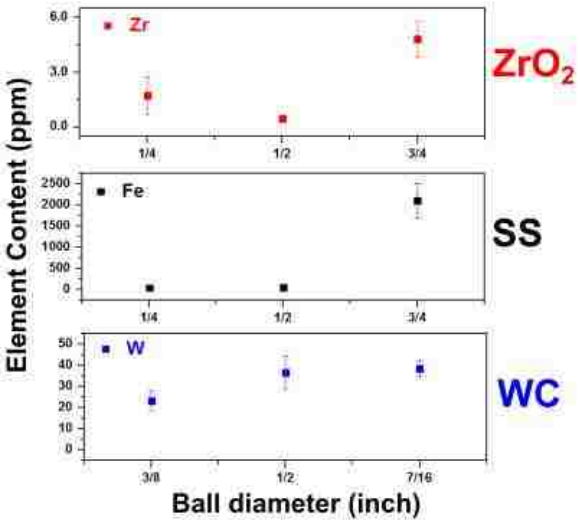

Figure 3–10 XRF results for *dh*-BN milled by milling balls made of ZrO_2 (red), stainless steel (black) and WC.

Our immediate observation was that several of the *dh*-BN milled with for 4 to 16 h, especially when milling with stainless steel balls, the powders were found to change colors (Figure 3-9). XRF measurements revealed high concentrations of Fe and P elements in *dh*-BN powders milled

with stainless steel milling balls. This was not the only case where contamination was revealed as shown in Figure 3-10. In powders treated with the ZrO_2 milling media for 2 h, a small quantity of Zr (up to 5 ppm) was found in the powders while in the powders treated with the WC milling media, W could be found. However the contamination by Fe was found to be much higher than any other with about 2000 ppm in the powder milled with a ¾ inch balls.

Beside contamination of the powder we noted that after milling *dh*-BN milled with ZrO_2 for longer than 8 h, the ZrO_2 balls that is usually ivory in color came out of the reactor with a pink color as shown in Figure 3-8. Optical images of the pink color milling balls revealed high density of surface scratches, resulting from the mechanical impact in the reactor. Although the presence of thin flakes of *h*-BN in the cracks can explain a change in color, the specific pink color remains to be investigated.

In summary, the contamination analysis suggested that to avoid potential ball milling induced contamination in the powder that would interfere with our catalytic processes, milling bearings made of ZrO_2 and treatment times below 2 h should be used to evaluate *h*-BN performances as a catalyst.

3.4.3.2 Effect of bearing size and bearing media

In Case Study One, we identified SEM as an effective characterization tool in assessing the effectiveness of defect creation by characterizing the morphology of *dh*-BN flakes. The SEM images of *dh*-BN flakes milled by ZrO_2, stainless steel and WC balls are presented in Figure 3-11. For each bearing media, the effect of bearing size was studied. We observed that, for all three bearing media, as bearing size increased, flakes were cut to smaller lateral dimensions and exfoliated to thinner thicknesses. This trend is similar to the size-decreasing trend we observed in

case study one as the milling time increased from 30 min to 120 min. For bearings made of the same material, the energy that was supplied by the larger bearings was the highest.

For 1/2 milling, SEM revealed that *dh*-BN flakes milled by stainless steel (Figure 3-11 (i, j)) and WC (Figure 3-11 (o, p)) bearings were finer than those milled by ZrO_2 bearings (Figure 3-11 (c, d)). WC media (14.95 g/cm^3) is known to have the highest specific gravity, followed by stainless steel (7.93 g/cm^3) and ZrO_2 (6 g/cm^3)[113]. Therefore it was expected that *dh*-BN flakes milled by ZrO_2 bearings would have the largest dimensions.

However, no obvious difference in flake size could be distinguished when comparing the effectiveness of stainless steel and WC bearings.

The FWHM values of the Raman E_{2g} mode of *h*-BN were extracted and listed in Table 3-5. In case study one, we found that the FWHM of the Raman E_{2g} mode of *h*-BN increased with longer milling times. As can be seen in this study, FWHM increased with increasing bearing diameter for all three media. In terms of composition of the bearing, the disorder in the lattice was found to be largest after WC impacts, with FWHM of 21.4 cm^{-1} compared to 16.5 cm^{-1} for ZrO_2 and 20.2 cm^{-1} for stainless steel. This is consistent with the SEM results and the specific gravity of the materials.

Table 3-5 Averaged FWHM values of BN E_{2g} mode Raman peak for *dh*-BN powders

	ZrO_2			**Stainless Steel**			**WC**		
Bearing size (inch)	1/4	1/2	3/4	1/4	1/2	3/4	3/8	1/2	7/16
Averaged FWHM (cm^{-1})	10.4	16.5	30.4	11.3	20.2	24.6	16.1	21.4	20.4

The gas molecule uptake values may serve as a good way of evaluating the amount of effective defect sites created by ball milling under different conditions. As can be seen in Table 3-4, with 2 h ball milling duration, increased ball media diameter from 1/4 inch to 3/4 inch improved mass uptake percentage from 2.05 % to 9.65 % after pressurization with propene. Same increasing trend was also observed for *dh*-BN powder milled with stainless steel milling balls. Milled by 3/4 inch milling balls, *dh*-BN powders prepared by stainless steel balls showed a smaller mass uptake (8.17 %) than those prepared by ZrO_2 balls (9.65 %), which could be explained by less effective defect sites due to stainless steel induced contamination. For *dh*-BN powder prepared by 2 h milling with WC balls, mass uptake increased from 5.19% to 6.65 % as milling ball size increased from 3/8 inch to 1/2 inch. However, further increase in ball size from 1/2 inch to 7/16 inch reduced mass uptake percentage to 5.59 %, possibly due to *dh*-BN agglomeration.

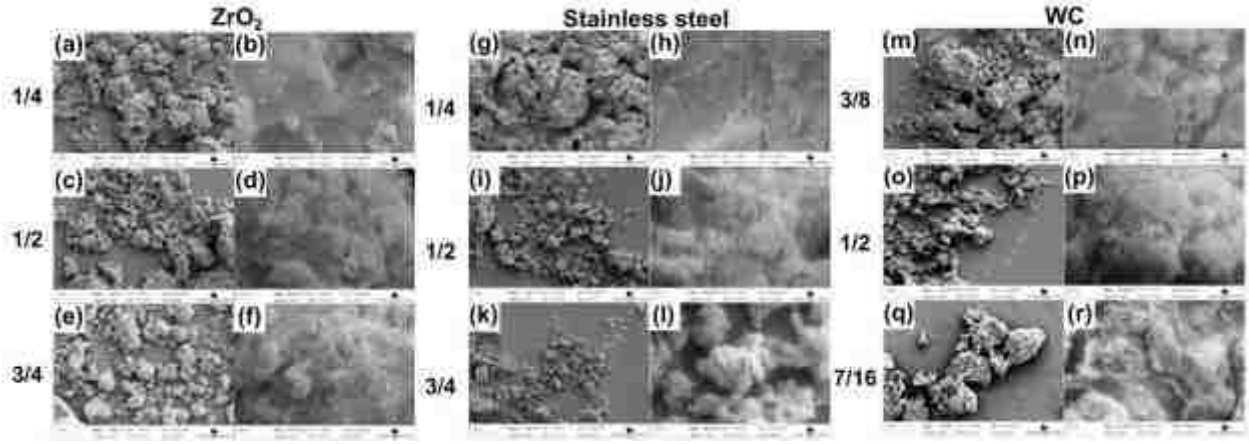

Figure 3–11 SEM image of *dh*-BN flakes milled for 2 h with milling with bearing of (a-f) ZrO_2; (g-l) stainless steel; (m-r) WC. The bearing diameters are listed on the left. The SEM images presented in the right column correspond to a zoom of the images in the left column.

3.4.4 Conclusions

In terms of material purity, defect density and fabrication cost, milling times beyond 2 h were not beneficial. This was evident from the smaller mass uptake for *dh*-BN powder milled for 8 h and beyond. In addition, severe milling induced contamination from the milling media, which seems to interfere with the reaction – particularly for stainless steel. For ball milling time up to 2 h, with same milling time, larger bearing diameters were found to produce more disorder in the flakes. With all other parameters (milling time, milling bearing size) maintained constant, bearings made of WC and stainless steels were more efficient than ZrO_2 in flake size reduction. However, ZrO_2 bearings left the least contaminations after 2 h milling. Hence ZrO_2 bearings and treatment up to 2 h were identified as the most suitable for future studies.

3.5 Case Study Three: Study of reaction of Oxygen on defect-laden hexagonal boron nitride through time-dependent fluorescence spectroscopy measurement

3.5.1 Background and Motivation

Case study one pondered on the effects of ball milling and heat treatments on *h*-BN properties and showed that both can introduce defects in *h-BN* layers, although varying results in terms of mass uptake. We have established that the FWHW of the Raman E_{2g} mode of h-BN can be used as an indicator of lattice disorder. However, direct revelation of defect structure and density remains challenging. Scanning tunneling microscopy (STM) and transmission electron microscope (TEM) are two approaches generally suitable for direct visualization of single-defect sites at the atomic level in catalysts [92,114-116]. However, they cannot readily be used for defect characterization in non-conductive materials such as wide band gap *h*-BN, without the use of a conductive substrate, which is known to interfere with the electronic states of the defects. Thus there is an unmet need to identify and characterize defects in *h*-BN, particularly in conjunction

with this applicability for catalysis.

Fluorescence spectroscopy of *h*-BN has revealed that luminescence traits are indicative of both native defect and doped impurities in *h*-BN lattice [85,117,118]. In *h*-BN, there are possible different kinds of native defects including boron (V_B) and nitrogen (V_N) vacancies and impurity defects such as substitutional carbon (C_N) or oxygen (O_N) atoms at nitrogen vacancy sites. Most of the mentioned defects in *h*-BN are luminescent and have their characteristic luminescence spectra [85]. Museur et al. [117,118] reported that *h*-BN with defects under optical excitation give rise to a complex-shaped photoluminescence (PL) spectra covering a spectral range from ~ 300 nm to visible light region. It has also been demonstrated that though different kinds of defects coexist in *h*-BN, each kind of defects could be distinguished by its characteristic fluorescence spectrum [117]. This assignment can be performed using de-convolution methods to estimate the complex-shaped spectra. In addition, each of the fluorescence bands could be assigned to specific defects or phenomena [85]. A detailed study was conducted on *h*-BN to resolve the different bands, especially those located near 400 nm, namely UV2 (~370 nm), UV1 (300 -350 nm) and V1 bands (below ~400 nm). UV2 band originates was from an impurity band transition and UV1 band was assigned to the formation of boron oxidation layer on the surface of the material. V1 band was attributed to the free oxygen molecule adsorption on the surface nitrogen vacancies (V_N) [117-120].

Based on these considerations, here we create defects in *h*-BN using ball milling and investigate the evolution of their fluorescence spectrum when exposed to air. We first study the optical properties of pristine *h*-BN and *dh*-BN prepared in oxygen-free environment. Next we compare the fluorescence increase to that of *dh*-BN pressurized with propene prior to their exposure to air. Especially, in this present work we study the spectral characteristics of defect induced

fluorescence near 400 nm for pristine *h*-BN and *dh*-BN. As the powders are exposed to different gas molecules, we hope to identify possible differences in the defect-molecule interactions of different powders. We discuss how the findings could be used as a simple assay to identify some properties of the defects introduced in the material.

3.5.2 Methods

3.5.2.1 Sample preparation

Ball milling preparation, gas exposure and mass uptake measurements employed here are described in Section 3.3.1.

3.5.2.2 Sample characterization

Time-dependent fluorescence: Fluorescence emission spectra were obtained using a microplate reader (Tecan Infinite® M200 PRO) with excitation wavelength selected 255 nm and emission scanning window from 280 nm to 850 nm. The same amounts of powders (0.025 g) were transferred to microplate wells (500 µl Nunc™ 96 Well polypropylene black round-bottom). The powders were carefully pressed to have a smooth surface. The measurements were carried out in ambient conditions. Fluorescence emission intensity spectra were captured on *h*-BN and *dh*-BN powders exposed in air for different durations.

Raman spectroscopy: Raman spectroscopy measurements were performed on a confocal microscope (WITec Alpha 300RA) equipped with a 532 nm excitation laser, and a 50X objective lens (Zeiss, N.A.= 0.7) for light focusing and collection. The light collected was filtered with a 532 nm notch filter prior to entering the spectrometer. An 1800 lines/mm grating, offering 0.9 cm^{-1} spectral resolution, was selected in the spectrometer. Photon counts were recorded with a

CCD camera. All Raman spectra were collected with laser power around 5.7 mW and integration time of 1 s.

Fourier transformed Infrared spectroscopy (FTIR): Mid-IR spectra were acquired using a FTIR spectrometer (PerkinElmer Spectrum 100 series, iris aperture 8.9 mm, spectral resolution 4 cm^{-1}) equipped with an attenuated total reflection (ATR) accessory (diamond/ZnSe crystal prism). The FTIR spectra were obtained in air in the 4000-650 cm^{-1} range. Four scans were collected and averaged for each sample group.

3.5.3 Results and Discussion

To explore the details of the defects introduced by ball milling, beyond the effect it has on the vibration of the lattice, we employed fluorescence spectroscopy, collected as successive time points over time.

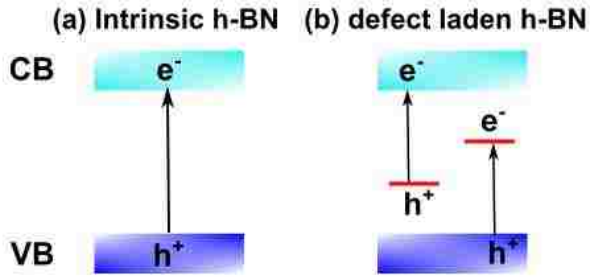

Figure 3–12 Schematic illustration of intra-band energy level addition in *h*-BN bandgap via (a) defect free intrinsic *h*-BN (b) defect laden *h*-BN with impurities or molecules reacting on the defects, exhibiting additional energy levels in the band gap.

The luminescent characteristics of *h*-BN with native defects and impurities have been extensively studied. The luminescence has previously been attributed to the radiative donor-acceptor recombination process [118]. Impurity atoms occupying boron or nitrogen vacancies can

give rise to additional energy levels in the *h*-BN bandgap. For example, C_N defects were found to introduce two energy levels located in the 3.2 – 4.9 eV energy range, which is below the *h*-BN conduction band [121]. As shown in Figure 3-12, the intra-band energy levels can then come into play in the recombination process of the electrons in the system [120,122]. Here we focus on defect- or impurity-related intra-band luminescence of BN.

3.5.3.1 Pristine h-BN

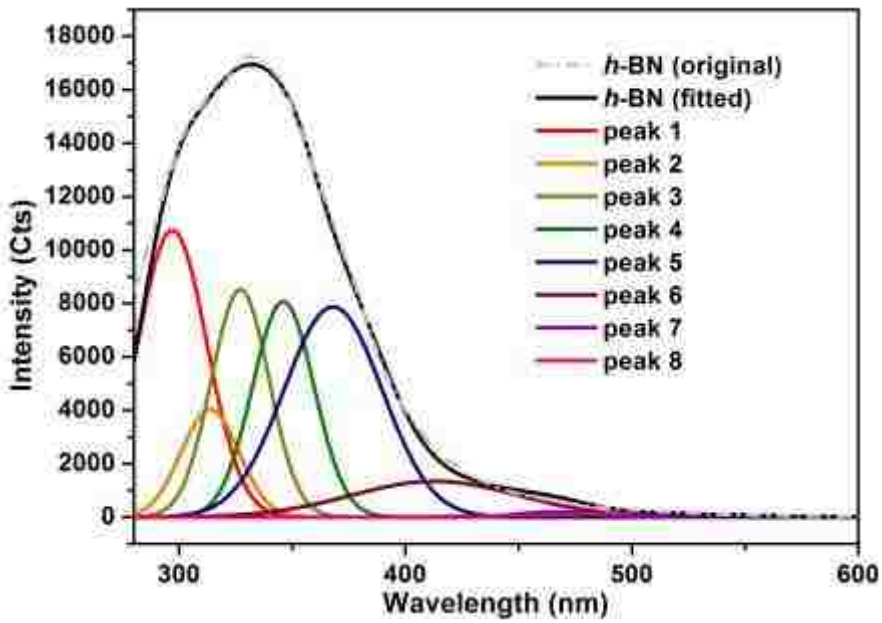

Figure 3–13 Fluorescence intensity for pristine *h*-BN flakes with corresponding peak deconvolution using 8 Gaussian fits selected based on literature assignments.

Table 3-6 Fluorescence peak intensity fitting results for pristine *h*-BN

UV2 band											
Peak 1			Peak 2			Peak 3			Peak 4		
Position (nm)	Intensity (a.u.)	Width (nm)	Position (nm)	Intensity (a.u.)	Width (nm)	Position (nm)	Intensity (a.u.)	Width (nm)	Position (nm)	Intensity (a.u.)	Width (nm)
297	10745	18	313.7	4032	15	327	8507	15	346	8066	16
UV1 band			V1 band								
Peak 5			Peak 6			Peak 7			Peak 8		
Position (nm)	Intensity (a.u.)	Width (nm)	Position (nm)	Intensity (a.u.)	Width (nm)	Position (nm)	Intensity (a.u.)	Width (nm)	Position (nm)	Intensity (a.u.)	Width (nm)
368	7873	25.5	413	1497	43.7	465.7	200	18.7	503.4	130	51

The fluorescence emission of pristine *h*-BN (Figure 3-13) was measured as a function of wavelength at 15 min time intervals upon exposure to air. For pristine *h*-BN, no intensity change was observed. A careful Gaussian fitting was used to estimate the various luminescence peaks previously described by Museur et al. [117,118]. The peaks correspond to: (1) the UV2 band, which includes 4 sub-bands (labeled as peak 1, 2, 3 and 4); (2) the asymmetric UV1 band (labeled as peak 5) located near 370 nm and (3) the broad visible V1 band (peak 6-8) located near 400 nm. For pristine *h*-BN, the intensity and positions of the fitted peaks are compiled in Table 3-6. The UV2 band peaks, as shown in Figure 3-14, our results are consistent with Museur at al. The 4 UV2 band sub-bands were assigned to impurity-band transitions. Peaks 2, 3 and 4 were identified as phonon replicas of the zero phonon line (peak 1) for the TO mode phonons, with 1, 2, 3 phonons emitted [118].

Here we assign the UV1 (peak 5) band luminescence to the transitions between conduction band of *h*-BN and the band introduced by oxygen of inherent defects in the flakes (nitrogen vacancies, oxygen substituted to a nitrogen or carbon substituted to a nitrogen [120-122]. In *h*-BN, we found that the fluorescence remained constant over time as all intrinsic vacancies are likely saturated with O from air (due to storage conditions).

For the V1 (peak 6-8) band, their origin was assigned by Museur [117,118] et al. to be from the surface nitrogen vacancies (V_N) free of oxygen molecule adsorption.

3.5.3.2 Ball milled dh-*BN*

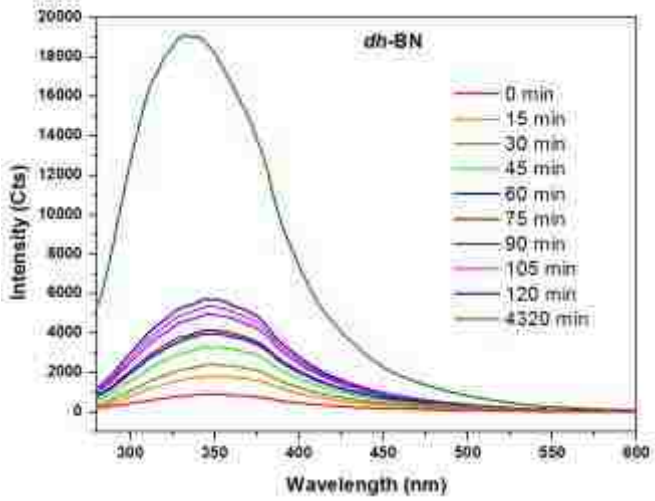

Figure 3–14 Evolution of the fluorescence intensity spectra for ball milled dh-BN from first exposure to air up to 4320 min (3 days) exposure to air.

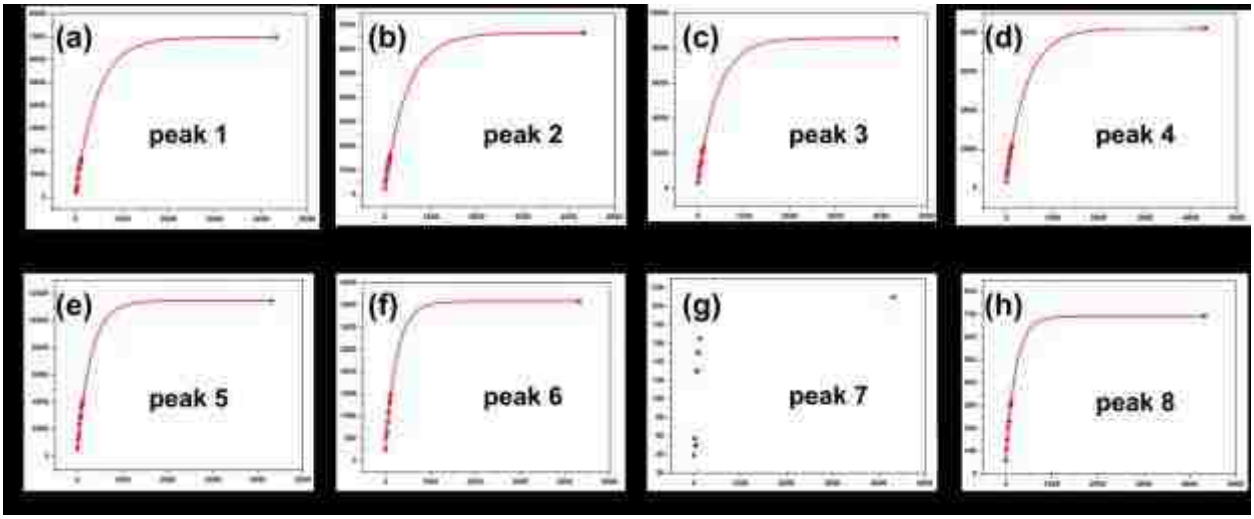

Figure 3–15 Time dependent fluorescence intensity for the 8 peaks fitted by Gaussian for ball milled *dh*-BN powder

Table 3-7 Fluorescence peak intensity fitting results for *dh*-BN exposed to air for different durations.

	UV2 band											
	Peak 1			Peak 2			Peak 3			Peak 4		
Exposure time (min)	Position (nm)	Intensity (a.u.)	Width (nm)	Position (nm)	Intensity (a.u.)	Width (nm)	Position (nm)	Intensity (a.u.)	Width (nm)	Position (nm)	Intensity (a.u.)	Width (nm)
0	297	238	18	313.7	255	15	327	352	15	346	329	16
15	297	360	18	313.7	551	15	327	688	15	346	694	16
30	297	502	18	313.7	655	15	327	911	15	346	932	16
45	297	835	18	313.7	939	15	327	1253	15	346	1225	16
60	297	1220	18	313.7	1157	15	327	1521	15	346	1513	16
75	297	1221	18	313.7	1261	15	327	1521	15	346	1621	16
90	297	1428	18	313.7	1394	15	327	2001	15	346	1860	16
105	297	1534	18	313.7	1500	15	327	2160	15	346	2047	16
120	297	1662	18	313.7	1643	15	327	2346	15	346	2189	16
4320	297	6985	18	313.7	6679	15	327	8583	15	346	8240	16
	UV1 band			V1 band								
	Peak 5			Peak 6			Peak 7			Peak 8		
Exposure time (min)	Position (nm)	Intensity (a.u.)	Width (nm)	Position (nm)	Intensity (a.u.)	Width (nm)	Position (nm)	Intensity (a.u.)	Width (nm)	Position (nm)	Intensity (a.u.)	Width (nm)
0	368	608	26.4	413	259	40.44	465.7	39	18.7	503.4	57.6	51
15	368	1275	26.4	413	525.7	40.44	465.7	57.3	18.7	503.4	108.6	51
30	368	1663	26.4	413	650	40.44	465.7	50	19	494.4	150	51
45	368	2359	26.4	413	871	40.44	465.7	50	19	494.2	200	51
60	368	2843	26.4	413	1100	35	465.7	130	19	494.2	230	51
75	368	3001	26.4	413	1100	35	465.7	130	19	494.2	230	51
90	368	3564	26.4	413	1300	35	465.7	150	19	494.2	300	45
105	368	3816	26.4	413	1380	35	465.7	150	19	494.2	300	45
120	368	4031	26.4	413	1494	35	465.7	165	19	495.2	314	45
4320	368	11480	26.4	413	3584	35	465.7	210	19	495.2	694	45

Next, to better understand the kinetics of defect-molecule interactions, we considered the evolution of fluorescence intensity of *dh*-BN (milled for 120 min) immediately after its exposure to air (*dh*-BN powders were stored in air-free environment prior to the first time point) for 4320 minutes (3 days) of exposure to air. The original time dependent fluorescence intensity spectra are plotted in Figure 3-14. For fluorescence intensity spectra acquired from 0 to 4320 min air exposure time, the same Gaussian peak fittings were applied to obtain 8 bands corresponding to the UV1, UV2 and V1 bands. For each peak (list as peak 1 to peak 8), the evolution of peak intensities as a function of exposure time are plotted in Figure 3-15.

During ball milling, we expect that large amount of edge defect and vacancies were introduced and thus a large amount of dangling bonds was created. In their study, Nash et al. [71] reported that nitrogen vacancies (V_N) are the most favorable defects to be created in *dh*-BN. Thus we expect that the 120 min ball milling treatment increased the presence of V_N defects. As shown in Figure 3-15, during exposure time from 0 to 1000 min, we observed a significant increase in intensities for peak 1, 2, 3 and 4 which all belonged to UV2 band as air interacted with *dh*-BN. The fluorescence intensity saturated after 1000 min, which indicates that almost all V_N defects were occupied.

For the UV1 band peaks (peak 5), as explained earlier, Kanaev et al.[119] assigned the peak to the formation of boron oxidation layer at the surface of the material. We observed an increase of the UV1 band peak intensity upon exposure to air. Furthermore, it has previously been demonstrated that B-O forms a very strong bond, which is thought to be more favorable than adsorption of O_2 on a V_N defect. Theoretical considerations support our experimental interpretation that the molecular oxygen gradually dissociated oxygen molecules to form O_N. As time passes, boron oxidation continues until all nitrogen vacancies are occupied and a saturation of the fluorescence intensity of UV1 band peak is reached. This assignment is also supported by the FTIR spectra of *dh*-BN powder with air exposure (shown in Figure 3-16), where B-O peaks can be observed.

3.5.3.3 dh-BN after propene uptake

Next, we studied the effect of exposing *dh*-BN powders to propene prior to the fluorescence measurement. The mass uptake observed indicated a 7.4% mass uptake upon propene exposure, indicating that some sites are occupied with molecules (carbohydrates) other than oxygen.

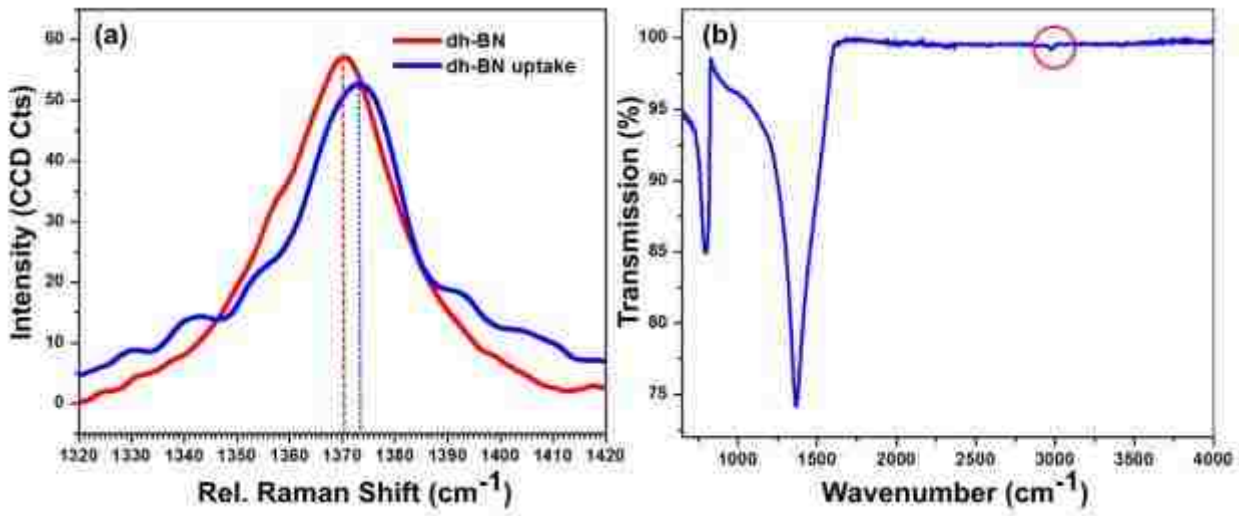

Figure 3–16 (a) Raman spectra for *dh*-BN before and after propene molecule uptake (b) FTIR spectra for *dh*-BN with propene molecule uptake

Raman E_{2g} mode of the propene-exposed *dh*-BN was found to be shifted from 1371 to 1373 cm^{-1}. Exposure to propene also led to the narrowing of the FWHM from 24.5 cm^{-1} to 22.1 cm^{-1}. However, these changes cannot be directly associated with the presence of carbohydrate on the defect sites. The FTIR spectrum of the propene-exposed *dh*-BN with short exposure to air, however, revealed a small band at ~ 2977 cm^{-1} (indicated by the red circle in Figure 3-16 (b)). This band has previously been assigned to the methyl group (CH_3) asymmetric stretch in propane or propene [123] indicative of the propene uptake by *dh*-BN. Mass uptake, Raman and FTIR signature all support the presence of carbohydrate bonds on the *dh*-BN powder.

Using the same protocol as for *h*-BN and *dh*-BN, we found that after exposure to air the fluorescence intensity increased even for the *dh*-BN powder exposed to propene, as shown in Figure 3-17,. The same Gaussian fits were used to monitor the increase in intensities and positions. A summary is provided in Table 3-8. No position shift was observed for UV1 and UV2 band fluorescence peaks. Nash et al. [71] calculated the binding energy for propene on

different types of defects in *h*-BN and the energy for propene to bind to V_B and V_N was found to be -3.69 eV and -1.76 eV, respectively. Assuming that the majority of the defect created during ball milling is V_N, we can infer that propene molecules block the access of oxygen. As shown in Figure 3-18, the fluorescence peak intensity increase followed an exponential trend. However, the rates of increase for UV1 and UV2 bands were lower than for *dh*-BN powder without prior propene uptake. Any propene molecule attached to a V_N hindered the passivation by oxygen. However, it is likely that not all defect sites were occupied upon pressurization with propene. In addition, the molecules resulting from the propene reaction with the defects could get dislodged by oxygen, as the reaction of O with V_N is more energy favorable. The decrease of the free nitrogen vacancies as well as the process of displacement of propene molecules can both slow down the process resulting to fluorescence increase.

Interestingly, even after 3 days the level of fluorescence in the *dh*-BN flakes with propene do not reach the same level of fluorescence as the one observed for *dh*-BN without exposure to propene. This may also suggest that some of the sites reacting with propene may not react with oxygen.

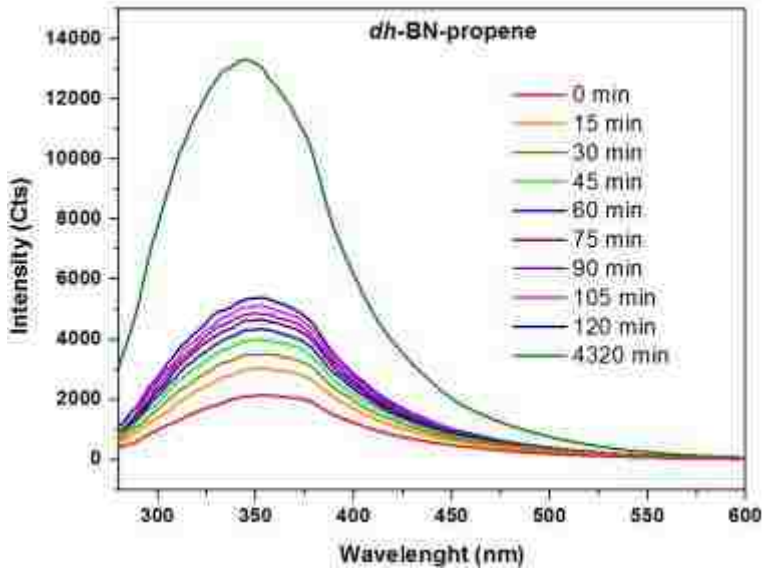

Figure 3–17 Evolution of the emitted fluorescence intensity of ball milled *dh*-BN with propene uptake after exposure to air for 3 days.

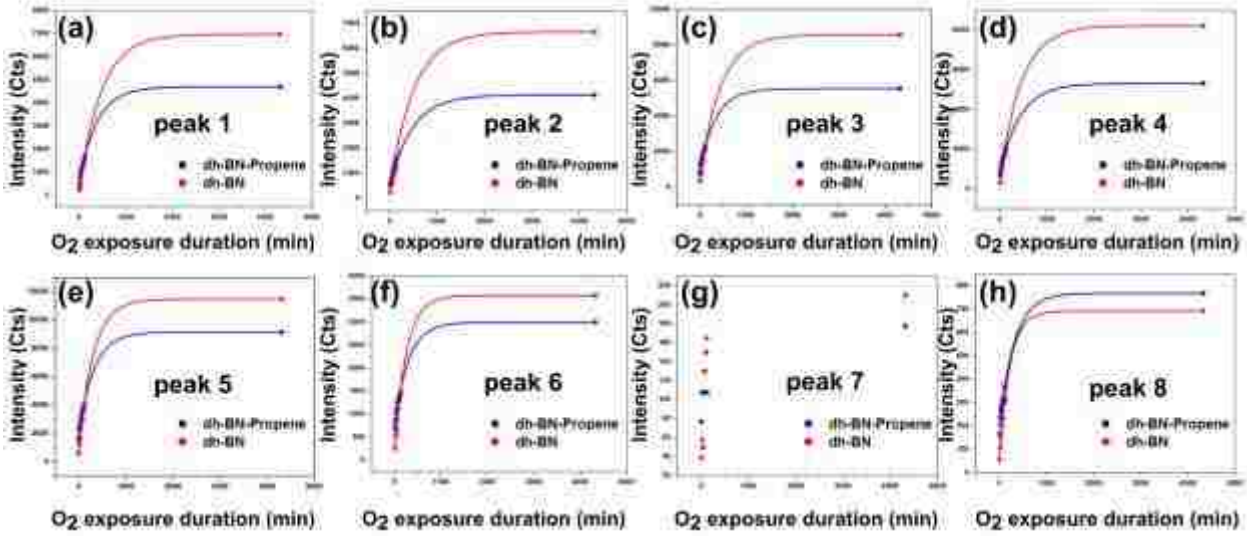

Figure 3–18 Evolution of the fluorescence intensity for *dh*-BN powder exposed to propene (blue color) and without exposure to propene (red color). The effect of exposure to air on the fluorescence intensity was monitored for 3 days.

Table 3-8 Fluorescence peak intensity fitting for *dh*-BN with propene uptake exposed to air for 3 days

Exposure time (min)	UV2 band											
	Peak 1			Peak 2			Peak 3			Peak 4		
	Position (nm)	Intensity (a.u.)	Width (nm)	Position (nm)	Intensity (a.u.)	Width (nm)	Position (nm)	Intensity (a.u.)	Width (nm)	Position (nm)	Intensity (a.u.)	Width (nm)
0	297	516	18	313.7	519	15	327	839	15	346	730	16
15	297	804	18	313.7	656	15	327	1250	15	346	997	16
30	297	1014	18	313.7	762	15	327	1424	15	346	1251	16
45	297	1194	18	313.7	833	15	327	1643	15	346	1371	16
60	297	1280	18	313.7	962	15	327	1730	15	346	1565	16
75	297	1326	18	313.7	1067	15	327	1974	15	346	1600	16
90	297	1486	18	313.7	1103	15	327	2048	15	346	1674	16
105	297	1538	18	313.7	1257	15	327	2177	15	346	1725	16
120	297	1713	18	313.7	1364	15	327	2218	15	346	1940	16
4320	297	4713	18	313.7	4144	15	327	5558	15	346	5330	16
Exposure time (min)	UV1 band			V1 band								
	Peak 5			Peak 6			Peak 7			Peak 8		
	Position (nm)	Intensity (a.u.)	Width (nm)	Position (nm)	Intensity (a.u.)	Width (nm)	Position (nm)	Intensity (a.u.)	Width (nm)	Position (nm)	Intensity (a.u.)	Width (nm)
0	368	1624	26.4	413	731	40.44	465.7	77	18.7	486.6	170	55.5
15	368	2339	26.4	413	875	40.44	465.7	108	18.7	486.6	239	55.5
30	368	2637	26.4	413	1033	40.44	465.7	108	18.7	486.6	266	55.5
45	368	2390	26.4	413	1133	40.44	465.7	108	19	486.6	286	55.5
60	368	3243	26.4	413	1262	40.44	465.7	108	19	486.6	308	55.5
75	368	3466	26.4	413	1344	35	465.7	108	19	485	319	55.5
90	368	3663	26.4	413	1344	35	465.7	108	19	485	319	55.5
105	368	3871	26.4	413	1434	35	465.7	108	19	485	370	55.5
120	368	4032	26.4	413	1434	35	465.7	108	19	485	370	55.5
4320	368	9152	26.4	413	3004	35	465.7	178	19	485	770	55.5

3.5.3.4 Long-term air exposure of dh-*BN powders*

After long term exposure to air (several weeks), the *dh*-BN powder and propene-exposed *dh*-BN powder were characterized again with FTIR spectroscopy. As shown in Figure 3-19, the FTIR spectra of both *dh*-BN powders exhibited similar characteristic peaks for N-B-O bonds at 922 cm^{-1} [124]. As mentioned earlier, this peak was also observed in pristine h-BN powder stored outside of the glove box, which confirms our assumption that oxidation takes place in pristine *h*-

BN. We note that these bands disappeared upon ball milling suggesting that the energy from the mechanochemical treatment is sufficient to break the B-O bonds (dissociation bond energy calculated from enthalpy change in gaseous state at 298 K: ~ 806 kJ/mol). Secondly, there is another peak indicative of B-O bonds at 1067 cm^{-1}. Numerous relatively strong bands appeared in the range 3100 - 3700 cm^{-1}. The bands near 3213 cm^{-1} and 3420 cm^{-1} were assigned to B-OH bonds and the formation mechanism will be explored in forthcoming studies.

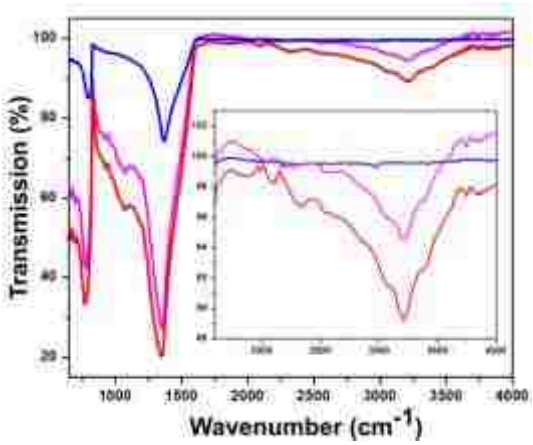

Figure 3–19 FTIR spectra of *dh*-BN powder with propene uptake before air exposure (blue), *dh*-BN powder with propene uptake after several weeks of exposure to air (pink), and *dh*-BN after several weeks of exposure to air (red)

3.5.4 Conclusions

Fluorescence combined with FTIR spectroscopy can be used to gain a deeper understanding of defects and their reactivity traits in presence of air. Our results highlight a time-dependence of fluorescence signature of *dh*-BN powders due to oxygen interacting with the defects. Using previously reported band assignments, deconvolution of fluorescence intensity peaks made it possible to observe the effect of oxygen binding on the energy band traps or oxidation of the

flakes. By comparing flakes with free defect sites and flakes with defect sites occupied by propene (or by-products of their reaction with propene) it was possible to assess a change in density of the oxygen-reactive sites. In the future, this work will be extended to pinpoint the effect of O_2, CO_2 and other molecules on defects. We will also exploit the data produced to back calculate the density of vacancies in the flakes, including the quantification of physisorbed vs. chemisorbed molecules in the flakes, by carrying out the same pressurization measurements on pristine h-BN, as described by Nash et al. The energy levels corresponding to the sub bands observed in fluorescence spectroscopy will also be confirmed using DFT calculations. Finally the FTIR spectra suggest that it is possible to detect signs of oxidation of propene reactions on the flakes after sufficient reaction time is allowed. This in turn suggests that tools with superior sensitivity or spatial resolution would likely provide additional information on these processes.

3.6 Summary and Future Perspectives

In summary, the processes of defect formations and catalytic reactions on a wide bandgap semiconductor in the form of nanoscale flakes/features are difficult to understand. Considering *h*-BN and *dh*-BN under more controlled conditions will be required to further understand how defects influence the structure and performance of the *h*-BN for catalytic applications. To reach more optimal gas molecule mass uptake and avoid potential contamination, ball milling conditions should be carefully optimized. In the case of *h*-BN, ZrO_2 milling at duration below 2 hours will be recommended.

The kinetics and competing processes taking place on defect sites in presence of reactive species should be considered further. All protocols, as well as a reaction chamber with controllable

environment and temperature will be developed in collaboration with Dr. Blair. This will strengthen our future studies on the system.

Lastly, microscale and nanoscale spectroscopy should be considered to further explore local changes in the system.

4 NANOSCALE SPECTROSCOPY FOR CATALYSIS APPLICATIONS

4.1 Background and Motivation

As discussed in Chapter 3, 2D materials are of great interests in catalytic applications for their unique structural and electronic properties that arise, in part, from the absence of the third dimension [125]. The predicted electronic properties of two-dimensional sheets of graphene [126,127] and metal dichalcogenides [128,129] have bolstered the interest in fundamental and applied research for nanoelectronics application. However, challenges associated with the scalability of growth processes [130], variations in band-gap due to intrinsic and extrinsic defects [130,131], and fluctuations in electron mobility in presence of various substrates [130,132] constitute important bottlenecks that continue to impede the full exploitation of 2D materials for nanoelectronics. Meanwhile, a large increase in applications of 2D materials in energy materials for solar cells [133,134], supercapacitors [135,136] and batteries [136,137] indicate enhanced performances relative to the rate of electrochemical reactions in the devices, which has been attributed to the high surface area of the nanomaterials with the active materials [138]. New functionalities can also be conferred to the material while maintaining its merits, as is the case for graphene hybridization. As a result, the performance of energy devices could be improved in terms of charge/discharge efficiency, energy density, and lifetime of the devices.

On the more fundamental aspect, some connections have been established between electronic and catalytic properties of 2D materials [139,140], although the details remain undetermined. Graphene has shown interesting behavior for electrocatalysis [141,142], photocatalysis [143] as well as conventional heterogeneous catalysis [144]. Further investigation of the mechanisms of catalysis of graphene [145,146] and other 2D materials including MoS_2 [139,147], WS_2 [148] and C_3N_4 [149] have outlined the importance of structural imperfections - i.e., vacancies, dislocations, edges,

impurities, functional groups and folds. The changes in electronic states introduced by the defects [125] have fostered rich experimental and theoretical endeavors for targeted catalysis by material design.

Various routes have been considered to tailor the electronic structure in view of promoting reactivity. The two-dimensional aspect of the catalyst significantly increases the surface area available for reactions [138]. Beyond the dimensional aspect, introducing doping elements in the 2D layers by physical or chemical treatment can also modify their electronic structure [89,150] to favor catalysis. Intercalation or substitutions are not the only mechanisms reported to introduce changes in the electronic structure. Defects including vacancies, edges, grain boundaries, ripples, ridges and wrinkles offer manifold of sites with distinct electronic structures of potential interest for catalysis [71]. The zigzag or armchair nature of edge defects in graphene have been shown to have an effect in the reactivity [151,152]. Similarly, vacancies and dislocations [153-155], as well as wrinkles, ripples and crumpled regions [156,157] introduce additional electronic states and modify the properties of the pristine flat material. Catalytic reactions at these different defect sites are under vigorous scrutiny. Deng et al. reported that edge defects in graphene promote oxygen reduction reaction in alkaline conditions [145] while Wang et al. found that structural defects promote triiodine reduction in dye-sensitized solar cells [146]. In metal dichalcogenides, it has been shown both theoretically and experimentally that the edges constitute active sites for electrochemical H_2 evolution [139,158-163]. Enhancement of desulfurization activity in Molybdenum disulfide (MoS_2) has been demonstrated by decorating the edge of MoS_2 with Cobalt (Co) [138]. The effect of wrinkles in MoS_2 has not yet been explored for catalytic reactions. Interestingly, catalytic properties of hexagonal Boron Nitride (*h*-BN) have not been explored to the same extent as those of graphene [145,146] and MoS_2 [139,147]. This is likely due to the wide bandgap of the

material. However, two studies by Grant et al. [73] and Nash et al. [71] recognized the catalytic reactivity of defects in *h*-BN, making *h*-BN an emerging candidate as noble metal-free 2D catalyst. Grant et al. reported that oxygen-terminated armchair BN edge defects are catalytic active sites for oxidative dehydrogenation [73]. Nash et al., on the other hand, demonstrated the role of defect laden *h*-BN for heterogeneous hydrogenation and computational modeling described nitrogen vacancies (V_N) as the most potent catalytically active sites [71]. In these studies, the wide bandgap of *h*-BN compared to graphene or MoS_2 did not seem to constitute a limitation. To our knowledge, the changes in properties induced by wrinkles in *h*-BN and their potential on catalytic reactivity of the material have not yet been explored.

In chapter 3, we investigated the effectiveness of mechanical ball milling and heat treatment processes in tailoring physical and chemical properties of free-standing *h*-BN powders for better catalytic performances. Traditional spectroscopic characterization methods including Raman spectroscopy, X-ray diffraction and scanning electron microscopy were used to gain a better understanding of defect creation, strain introduction; change in crystalline order and agglomeration of *dh*-BN. Time-dependent fluorescence spectroscopy was used to study the catalytic traits during defect-molecule reactions. However the nature of the defect induced and of the chemistry taking place at the defect sites could not yet be resolved.

In this chapter, AFM based nanoscale spectroscopic methods evaluated to determine whether they can resolve changes in morphology and physical properties originating from treatments to produce *dh*-BN, and the chemistry taking place at defect sites. Our work in presented in the form of two case studies, as described below.

In **case study one**, we investigate defect engineering in mechanically exfoliated *h*-BN via heat treatment using a combination of AFM-based characterization methods. Specifically, we

carefully compare the microstructure, physical, chemical and catalytic properties of *h*-BN flake samples before and after heat treatment at the scale which is not accessible via conventional spectroscopic methods.

In **case study two**, we investigate laser-assisted local defect engineering in *h*-BN flake samples and *in-situ* characterization to study the effect of localized defect creation on material property changes.

4.2 Case Study One: Heat treatment-assisted defect engineering in h-BN flake samples and subsequent characterization for catalytic applications

4.2.1 Background and Motivation

Catalytic properties of *h*-BN have not been explored to the level of graphene [145,146] and MoS_2 [139,147]. This is likely due to the absence of metal atom in the flake and the wide bandgap of the material. However, two recent studies by Grant et al. [73] and Nash et al. [71] recognized the catalytic reactivity of defects in *h*-BN, making *h*-BN an emerging candidate as metal-free 2D catalyst. Grant et al. reported that oxygen-terminated armchair BN edge defects are catalytic active sites for oxidative dehydrogenation [73]. Nash et al., on the other hand, demonstrated the role of defect laden *h*-BN for heterogeneous hydrogenation and computational modeling described nitrogen vacancies (V_N) as the most potent catalytically active sites [71]. In these studies, the wide bandgap of *h*-BN compared to graphene or MoS_2 did not seem to constitute a limitation. To our knowledge, the changes in properties induced by wrinkles in *h*-BN and their potential on catalytic reactivity of the material have not yet been explored.

Heat treatment and quenching are heavily used in material science to create point defects. We compare the behavior of MoS_2, graphene and *h*-BN following this treatment. Changes in structure and properties induced are probed with spectroscopy and nanoscale functional imaging. At selected temperatures, we observe the formation of wrinkles with distinct characteristics. We explore the origin of these features and their effect on the optical, mechanical, electronic and chemical properties of the pristine layers. Lastly, using a novel functional nanoscale imaging approach combining atomic force microscopy (AFM) and infrared spectroscopy, we demonstrate that wrinkles formed by heat treated on the *h*-BN layer act as a reactive site for carbohydrate molecules.

4.2.2 Methods

4.2.2.1 Mechanical Exfoliation

Few-layer *h*-BN flakes were mechanically exfoliated from bulk high purity *h*-BN single crystals (HQ Graphene) using conventional tape cleavage method before being transferred onto clean oxidized Si substrate (250 nm thermal grown SiO_2 layer on top of Si wafer). Similar procedure was used to exfoliate graphene and MoS_2.

4.2.2.2 Heat treatment

Heat-treatment of the exfoliated flakes was carried out in a Thermolyne Small Benchtop Muffle Furnace (Type 1400, Thermo Scientific). The *h*-BN flakes on the SiO_2/Si substrate were placed in the furnace stabilized at a temperature of 1073 K (800 ˚C) and heat treated in air for 30 min, after which the samples were immediately quenched to room temperature in air. The graphene flakes on the SiO_2/Si substrate were placed in the furnace stabilized at a temperature of 873 K (600 ˚C) and heat treated in air. After 30 min, the samples were quenched to room temperature in

air. Finally, the MoS_2 flakes on the SiO_2/Si substrate were placed in the furnace stabilized at a temperature of 733 K (460 ˚C). After 30 min of heat treatment, the samples were quenched to room temperature in air.

4.2.2.3 Structural characterization

Optical microscopy: Optical images of the exfoliated BN layers on SiO_2/Si substrates were acquired using Olympus BX51 optical microscope.

Atomic force microscopy (AFM): Tapping mode AFM was used to confirm the thickness and number of layers of exfoliated flakes. All measurements were carried out in air on an AFM system (WITec Alpha 300RA). Cantilevers (MikroMasch, HQ:XSC11/Al BS; Cantilever B with resonance frequency 80 kHz and force constant 2.7 N/m) were used for AFM morphology measurements.

4.2.2.4 Composition and optical properties characterization

Raman spectroscopy and Photoluminescence (PL): A confocal Raman microscope (WITec Alpha 300RA) equipped with a 532 nm excitation laser was used to collect Raman spectra using a 100X objective lens (Zeiss, N.A = 0.7). The spectrometer was set to the 1800 lines/mm grating for Raman measurements and to the 600 lines/mm grating for PL measurements (performed only on MoS_2 flakes). The integration time was set to 1 s for a laser power of ~5 mW for *h*-BN and below 1 mW for graphene and MoS_2 to avoid laser induced degradation of the samples.

4.2.2.5 Mechanical property characterization

Pulsed force microscopy (PFM): Pulsed Force Microscopy (PFM) measurements were used to study the effect of heat treatment on the mechanical property of the material. The measurements

were carried out with the same platform (WITec Alpha 300RA) used for tapping mode AFM. Cantilevers (MikroMasch, HQ:XSC11/Al BS; Cantilever B with resonance frequency 80 kHz and force constant 2.7 N/m) were used for PFM.

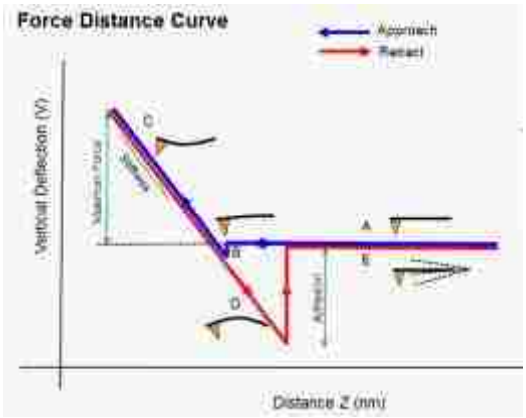

Figure 4–1 Schematic of PFM force-distance curve showing how stiffness and adhesion properties can be accessed in the force curve [164]

In PFM, a sinusoidal modulation is applied to the cantilever through a piezo component at a frequency (1 kHz) much lower than the resonance frequency of the cantilever. During each modulation cycle, the amplitude is controlled by the AFM controller so that the tip-sample distance ranges from a position where there is no tip-sample interaction to a position where the tip makes a small indentation in the sample. The resulting force-time curve is simultaneously acquired by monitoring the deflection of the cantilever at each step of the “approach” and “retract” motion. A force-time curve can be converted to a force-distance curve, which can be analyzed to estimate the tip-sample adhesion and stiffness of the material. Stiffness is obtained by calculating the slope of the retract curve when the cantilever is in contact with the sample. The tip-sample adhesion corresponds to the difference between the lowest point of the “retract” curve immediately before the “jump-out-of–contact” point, and the baseline after the tip breaks free from the surface. .

Lorentz contact resonance AFM (LCR): LCR measurements were performed on a NanoIR2 platform (Anasys Instrument, Inc., Santra Barbara, CA) using a special U-shaped conductive cantilever (ThermaLever PR-EX-AN2-200-5).

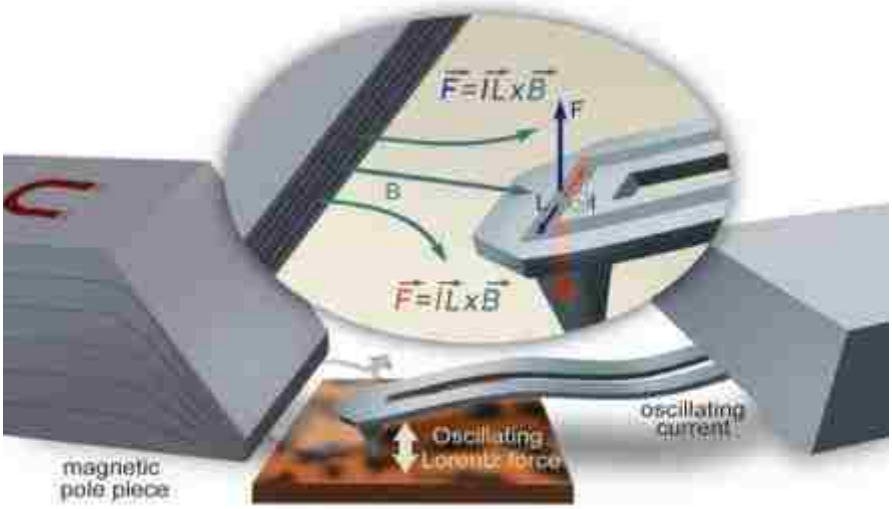

Figure 4–2 Schematic of LCR[165]

In LCR AFM, an alternating current (AC) is sent to the cantilever, while applying a magnetic field using a strong permanent magnet in a direction which is normal to the current applied to the cantilever. As a result, a Lorentz force is induced in the direction which is perpendicular to both the current and the magnetic field applied. When the AC is supplied to the cantilever, the Lorentz force engenders an oscillation to the cantilever. LCR spectra are recorded at selected points on the sample surface by sweeping the cantilever within a user-specified frequency range. The driving frequency is used as the reference of the lock-in amplifier. Shifts in contact resonance correspond to a change in mechanical property in the material [166]. Hence, by collecting contact resonances across a region of interest, changes in mechanical properties of sample can be recorded. This is often done by monitoring amplitude and/or frequency of the contact resonant peak.

4.2.2.6 Electrical property characterization

Electrostatic force microscopy (EFM): EFM measurements were carried out on a MultiMode AFM operated in lift mode (Veeco Metrology LLC, Santa Barbara, CA, USA) using conductive cantilevers (MikroMasch, HQ:XSC11/Pt; Cantilever B with resonance frequency 80 kHz and force constant 2.7 N/m).

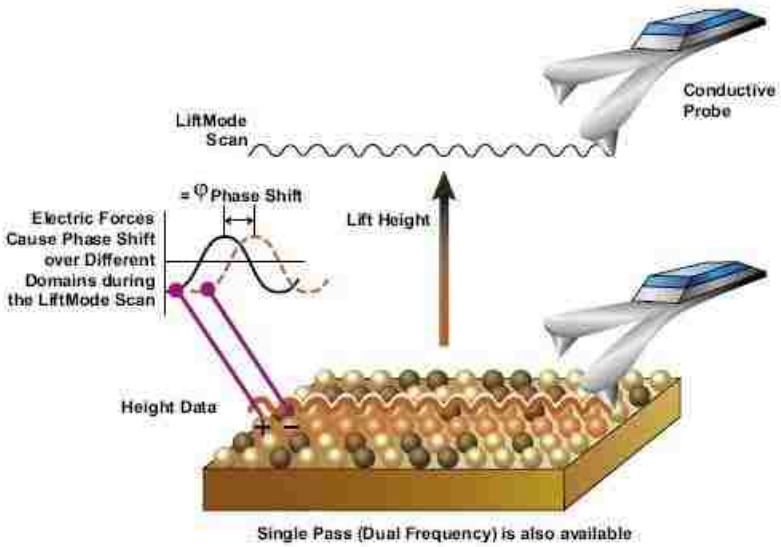

Figure 4–3 Schematic of electrostatic force microscopy [167]

As shown in Figure 4-3, in EFM the electrostatic force between the tip and the sample are measured. This involves a two-pass method: on the first pass, the conductive cantilever actuated at its resonant frequency to collect the topography of the sample surface. Next, on the second pass, the tip is lifted from the surface (interleave) by a specified distance (25 nm in this case) to detect the bias-induced (capacitive-induced) long range electrostatic force without the interference of short range van der Waals forces. Electrostatic forces cause the cantilever resonance to shift, which is recorded by monitoring the phase shift. In this study, the phase shifts resulting from a +/-3V bias applied to the tip were recorded.

Kelvin Probe Microscopy (KPFM): Detailed description of KPFM can be found in section 2.2. KPFM was conducted on the AFM NanoIR2 platform (Anasys Instrument, Inc., Santra Barbara, CA) equipped with a KPFM module. KPFM probes (PR-EX-KPFM-5; typical resonant frequency ~55 kHz; Anasys Instrument, Inc.) were used. The sample was grounded on a sample stage and a bias (ΔV) was applied to a conductive AFM cantilever.

4.2.2.7 Catalytic activity characterization of the material after exposure to molecules

Time-of-flight secondary ion mass spectroscopy (ToF-SIMS): ToF-SIMS measurements were conducted at The Center for Nanophase Materials Sciences at the Oak Ridge National Laboratory. ToF-SIMS spectra for BN flakes before and after heat treatment were performed in positive ions detection mode using a TOF-SIMS 5 instrument (ION-TOF GmbH, Germany) equipped with a Bi liquid metal ion gun (LMIG) as the primary ion source delivering Bi^{3+} ion clusters onto sample surfaces. The vacuum level of the chamber was maintained at ~ 5×10^{-9} mbar during the measurements. The primary ion clusters bombarded sample surfaces at an accident angel of 45˚ with a kinetic energy of 30 keV. Secondary ions were accelerated and collected though a time-of-flight analyser. A low energy electron flood gun was employed to neutralize sample surface charges. The images were collected in positive ion mode across an area of 100×100 μm^2 scan size through a raster scan mode with a resolution of 256×256 points. During scanning, the sample stage was continually moved in a saw-tooth mode to allow the rastering of the primary ion beam at each pixel. The properties of the selected region of interest were displayed as a map, reconstructed by filter out any data not directly related to BN. For pristine BN flake and heat treated BN flake, the selected regions of interest were the same size to improve the comparability of the data.

Sample preparation for ToF-SIMS measurements: pristine BN and heat treated BN sitting on SiO_2/Si substrate were directly glued to ToF-SIMS sample holder using silver paste. Sample holder was loaded in to ToF-SIMS chamber after the silver paste was dried.

4.2.3 Results and Discussion

Mono- or few-layers of 2D materials such as *h*-BN can be identified using optical microscopy despite their high bandgap (~5.9-6.1 eV) [168] causing high opacity (inset in Figure 4-4 (g)).

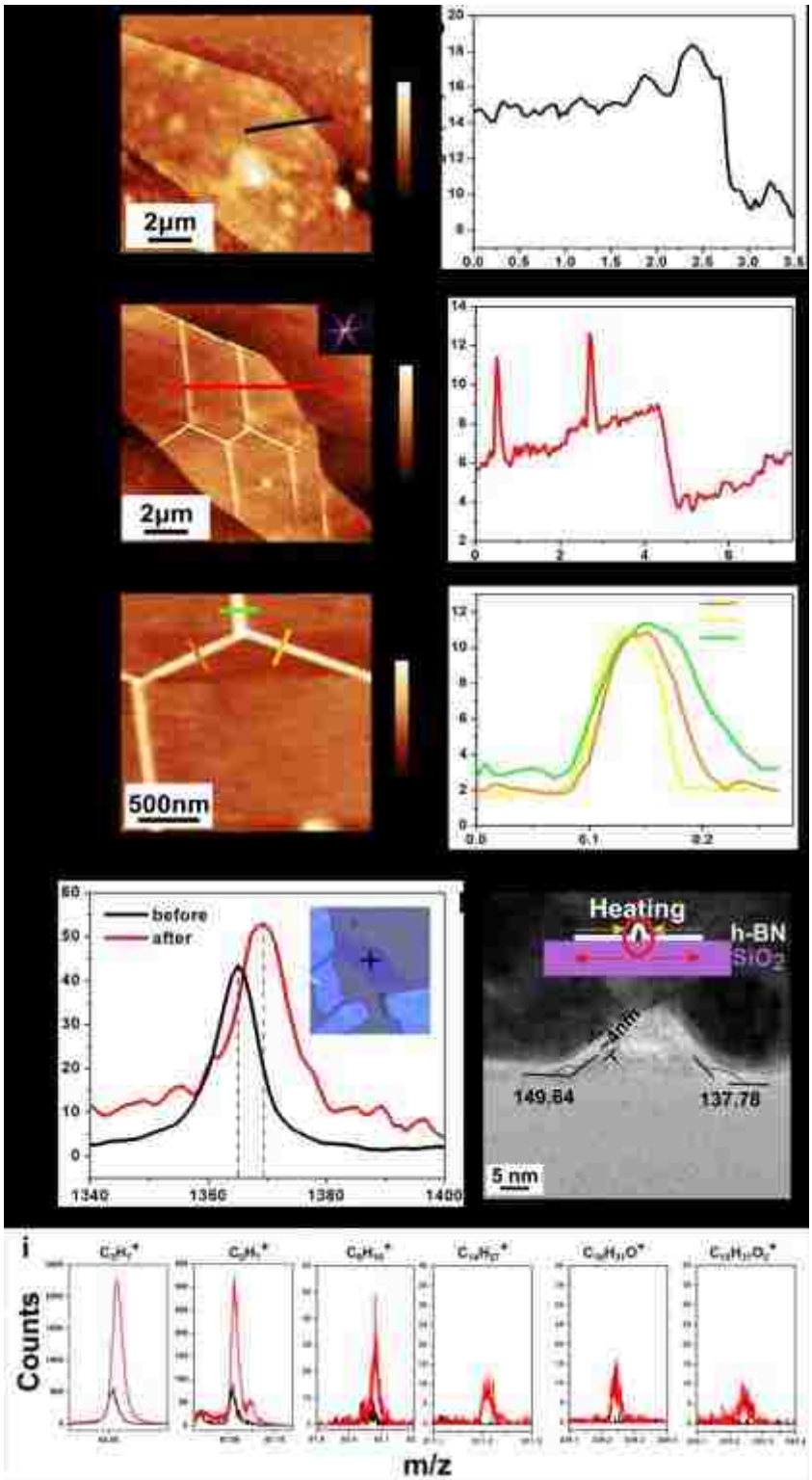

Figure 4–4 AFM morphology image of BN flake (a) before heat treatment and (c,e) after heat treatment; (b,d,f) cross section profiles for lines indicated in (a,(c,e), respectively; (g) single

Raman spectra for BN flake before and after heat treatment; (h) TEM image of wrinkle cross-section with a schematic illustration of heat treatment and subsequent quenching for wrinkle formation; (i) Selected from ToF-SIMS spectra spectra showing the presence of hydrocarbon chains on the heat treated flakes.

Figure 4-4 (a) represents the topography of a mechanically exfoliated *h*-BN flake of the thinnest flake present in the region of the optical image (appearing in purple in the optical image). Figure 4-4 (b) represents the profile of the pristine thin flake height, estimated at ~4 nm, suggesting a flake of 10 layers [169]. After heat treatment at 800 ˚C for 30 min (see Methods), the topography of the flake (Figure 4-4 (c)) exhibits clear changes. Glue residues are no longer present and more importantly, wrinkles with a well-defined geometric pattern are present across the flake. Fast Fourier transform (FFT) of Figure 4-4 (c) (inset in the upper right corner) reveals a threefold rotational periodicity for the orientation of the wrinkles, corresponding to an angle of about 120˚ between two adjacent wrinkle arms. This special rotational orientation suggests that the formation of the three arms in *h*-BN may follow the crystallography of the lattice, i.e. zigzag or armchair [170]. Oliveira et. al. studied the correlation between the *h*-BN lattice and the orientation of similar so-called origami features experimentally and theoretically and reported that the features were oriented along the armchair crystallographic direction of *h*-BN lattice [170]. Figure 4-4 (e), presents a higher resolution image of wrinkle arms. The cross section profiles for these arms are plotted in Figure 4-4 (f). As indicated by the section profiles in Figure 4-4 (f) the three wrinkles are about 5-6 nm in height though the flake remains 4 nm in thickness after the heat treatment. The mismatch between the thermal properties of *h*-BN and its substrate SiO_2 seem to be the main contributor of wrinkles formation. *h*-BN is anisotropic with a thermal expansion coefficient (TEC) that is negative in the a-axis direction (-2.83×10^{-6} K^{-1} at 298K) and remains

negative even at elevated temperature while the TEC is positive in the c-axis direction (40.5×10^{-6} K^{-1} in the range of 273-800 K)[171,172]. On the other hand, the TEC of SiO_2 is positive above room temperature [173]. Hence, the TEC mismatch between the substrate and the sample is likely to cause *h*-BN sheets to contract (expand) as SiO_2 substrate expands (contracts) during the heating (cooling) processes. As a result, the *h*-BN sheets are under increasing tensile (compressive) stress/strain as temperature increases (decreases) (Figure 4-4 (h)). For thin flakes, as temperature increases further, the tensile stress can reach a level such that it forms cracks in the *h*-BN.

The catalytic property of *h*-BN flakes before and after heat treatment was evaluated by ToF-SIMS measurement. Spectra obtained from pristine and heat treated *h*-BN flakes were compared and only those peaks which only appeared on heat treated *h*-BN flakes were extracted and plotted as shown in Figure 4-4 (i), molecular fragments which come from hydrocarbon molecules were identified only on heat treated flakes, indicating that most likely *h*-BN became catalytic active after heat treated defect creation.

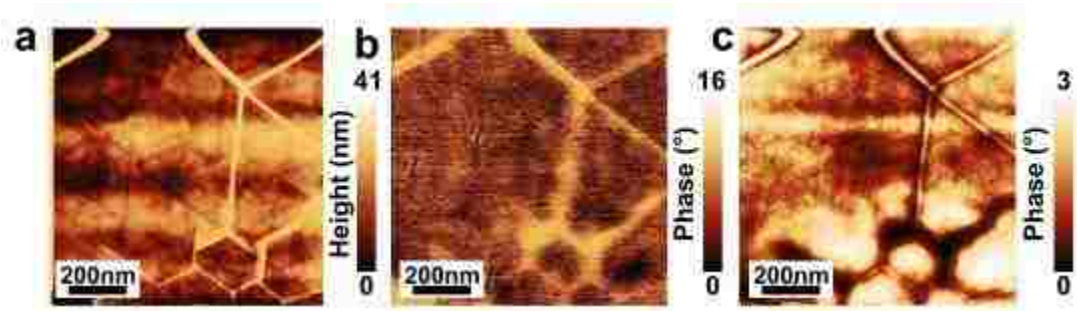

Figure 4–5 Nanoscale functional imaging to of heated-treated h-BN (a) AFM morphology and corresponding (b) EFM phase image with +3V tip bias, (c) EFM phase image with -3V tip bias

It has already been demonstrated that electronic properties of 2D materials can be changed by introducing folds, ripples or wrinkles [174-176]. For example, Zhu, et al. reported that wrinkles in graphene can lead to the changes in its band gap and local chemical potential. Kim et al.[177]

theoretically studied the effect of ripples. The ripples were found to induce electrochemical potential change in graphene. EFM has been widely employed to investigate surface electrical properties of 2D materials. In EFM, it is capable to get high special resolution maps over 2D flakes, revealing material morphology and distribution of electrical charges/potentials across the scanned region simultaneously [178].

The EFM maps of heat treated *h*-BN are presented in Figure 4-5. The topography indicating the position of the folds is provided in Figure 4-5(a). Figure 4-5 (b) corresponds to the EFM map captured while applying a +3V bias to the tip while Figure 4-5(c) correspond to the EFM at a -3V bias. The maps indicate a variation in the electrostatic force around the wrinkle. In Figure 4-5 (b), the phase shift of less than 5° was fairly uniform in the flat region of the flake, while the phase shift increased of up to 16° along the wrinkle. The phase shift corresponds to a change in the electrostatic force between the tip and the sample. It has previously been demonstrated that, when a positive bias is applied, a large positive phase shift ($+\theta$) (brighter color) corresponds to a repulsive force between the tip and the sample, which suggests that the origami-like features are more positively charged than the flat regions. Interestingly, the phase image acquired for -3V bias, shows a negative phase shift in most regions, consistent with the previous results, but the top of the wrinkle exhibited a positive phase shift. We note that EFM measurements can be highly sensitive to sharp variations in topography such at the wrinkles, because the configuration of the tip-sample distance changes, as demonstrated in the schematics. Thus the EFM images alone cannot be used to conclude on the charges distribution around the wrinkles. However, in conjunction with the TEM cross section as shown in Figure 4-5 (h), it seems plausible for the wrinkles to experience charge redistribution from the arrangement in the pristine *h*-BN and flat regions of the heat treated BN. In our case, the angles, lengths and curvature of the B-N bonds

around the wrinkle are quite different from those in the pristine flake, as shown in our TEM images (Figure 4-4 (h)), which is likely to shift the electronic cloud around the atoms and the bonds.[179]. Our observations of wrinkle induced charge re-distribution are in good agreement with previous reports demonstrating that the localized strain around ripples in graphene could introduce inhomogeneous charge distributions [177]. In fact, Kim et al. reported their theoretical findings that ripples introduced charge redistribution which in turn stabilized ripple structure [177]. Our measurements suggest that local strain remains in the flake after heat treatment and quenching of *h*-BN on a SiO_2 substrate.

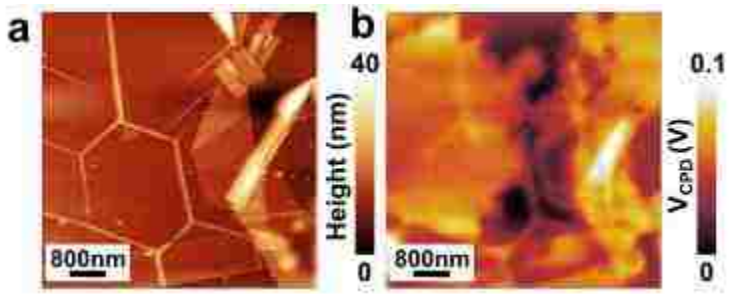

Figure 4–6 (a) AFM morphology and corresponding (b) KPFM image

In addition to charge distribution, we studied the effect of the folds on the work function of the material using KPFM [180] (see methods). In Figure 4-6, we measured the contact potential difference (V_{CPD}) between a metallic coated AFM tip and a selected region of the *h*-BN flake (see Methods). KPFM has been used to measure the work function on many low dimension materials including graphene [181] and MoS_2 [182] to assess the electrical property distributions across region of interest. For example, for both graphene and MoS_2, surface potential or work function of the materials is strongly dependent on structural properties such as thickness, KPFM was applied to map the work function at the monolayer-multilayer conjunction and clear distinction could be resolved between interface layers due to the different V_{CPD} values The KPFM map

(Figure 4-6 (b)) reveals that the work function along the folds is lower than that in the flat regions. Interestingly, the V_{CPD} measured at the wrinkle sites was similar to the V_{CDP} measured at edges introduced because of cracks in the material. Edges of *h*-BN have previously been shown to be the sites for interesting reactions [183]. Hence the data is a good indication that folds have potential as active sites for reactions. We note that wrinkle induced work function difference has also been reported by Samaddar et al. [184] when studying the change in work function on graphene wrinkles. Moreover, as already evidenced by EFM results, the changes were not only on the wrinkles but also on the flat regions, likely due to inhomogeneities and defects introduced by heating/quenching.

To better understand these variations in mechanical properties of the heat-treated *h*-BN, we investigated mechanical property characterization. The presence of wrinkles is expected to affect the mechanical properties of the pristine 2D layers [185], however this has not been investigated theoretically or experimentally in *h*-BN as conducting conventional tensile/compress tests is impractical due the flakes dimensions. Taking in consideration of the nanoscale special resolution requirements, such high resolution characterization of mechanical properties could only be achieved through nanomechanical measurements. Nanoindentation is one of the methods that have been developed for nanoscale mechanical property characterization. The few reported measurements by nanoindentation [186,187] required for the 2D layer to be suspended which can be challenging, and may not allow from the wrinkles to form. In essence, local strain and stiffness, which can play important role in the design of functional materials, are not readily accessible. AFM based platforms methods are emerging with great promise as tools for nanoscale mechanical property characterization. AFM phase imaging is the most common way of differentiating material mechanical properties. In AFM phase imaging, the phase difference

between cantilever driving and response is monitored. However other mechanical traits such as adhesion and stiffness can affect AFM phase imaging contrast simultaneously, making it difficult to study individual mechanical property. AFM based contact resonance microscopy such as Lorentz contact resonance microscopy have emerged as promising candidates to measure localized mechanical properties.

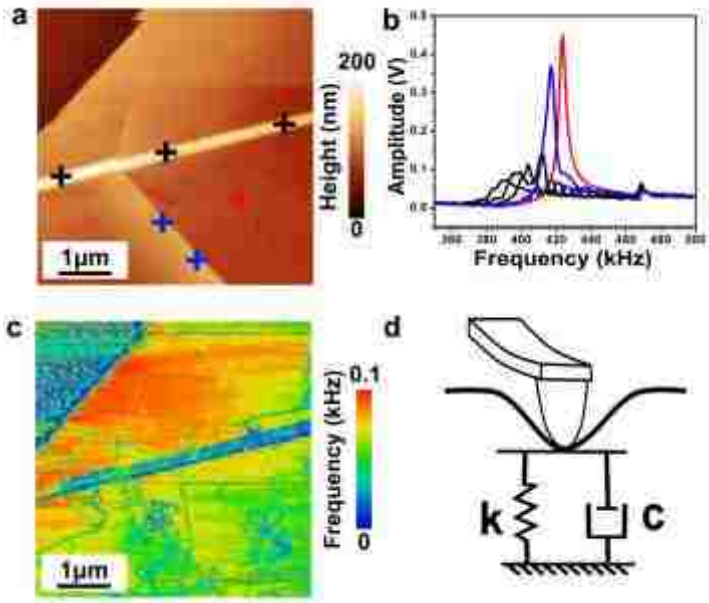

Figure 4–7 Nanoscale mechanical imaging of heat-treated h-BN (a) AFM morphology of BN flake (b) LCR spectra for point selected from different regions (c) LCR frequency mapping (d) Kelvin–Voigt mechanical equivalent model for LCR

We used here Lorentz contact resonance (LCR) to study the local mechanical properties. The data is shown Figure 4-7 (a-c). LCR is advantageous over nano-indentation as it circumvents the substrate interference and hard tip-sample damages by measuring the changes in contact resonance of the cantilever with minimal or no indentation [188]. Our high resolution image of the

wrinkle shows a significant shift in contact resonance of the cantilever revealing nanoscale spatial inhomogeneous distribution of stiffness and viscoelasticity.

In LCR, as illustrated in Figure 4-7 (d), sample-probe interaction can be described by the Voigt-Kelvin model [189] consisting of an ideal elastic spring coupled with an ideal viscous sample in parallel. The position shift of the contact resonance frequency is dependent on stiffness variation: typically, contact resonance frequency increases as tip-sample contact stiffness increases [190, 189]. However, other parameters including applied force (setpoint) can affect the measured resonance frequency. Figure 4-7 (b) shows the nanomechanical spectra obtained from different regions on the *h*-BN sample surface. Compared to the contact resonance frequency from flat region (blue color), the frequency shift to the left on wrinkle arms indicates the decreased stiffness [190,191]. Fan et al.[192] studied the effect of wrinkles on the mechanical properties of graphene nanoribbions by molecular dynamics simulation and similarly reported a decreased in contact stiffness at the wrinkle [192]. Frequency mapping (Figure 4-7 (c)) around 420 kHz (i.e. contact resonance frequency at flat BN region as indicated by the red peak in Figure 4-7 (b)) reveals inhomogeneous stiffness distribution of the imaged flake.

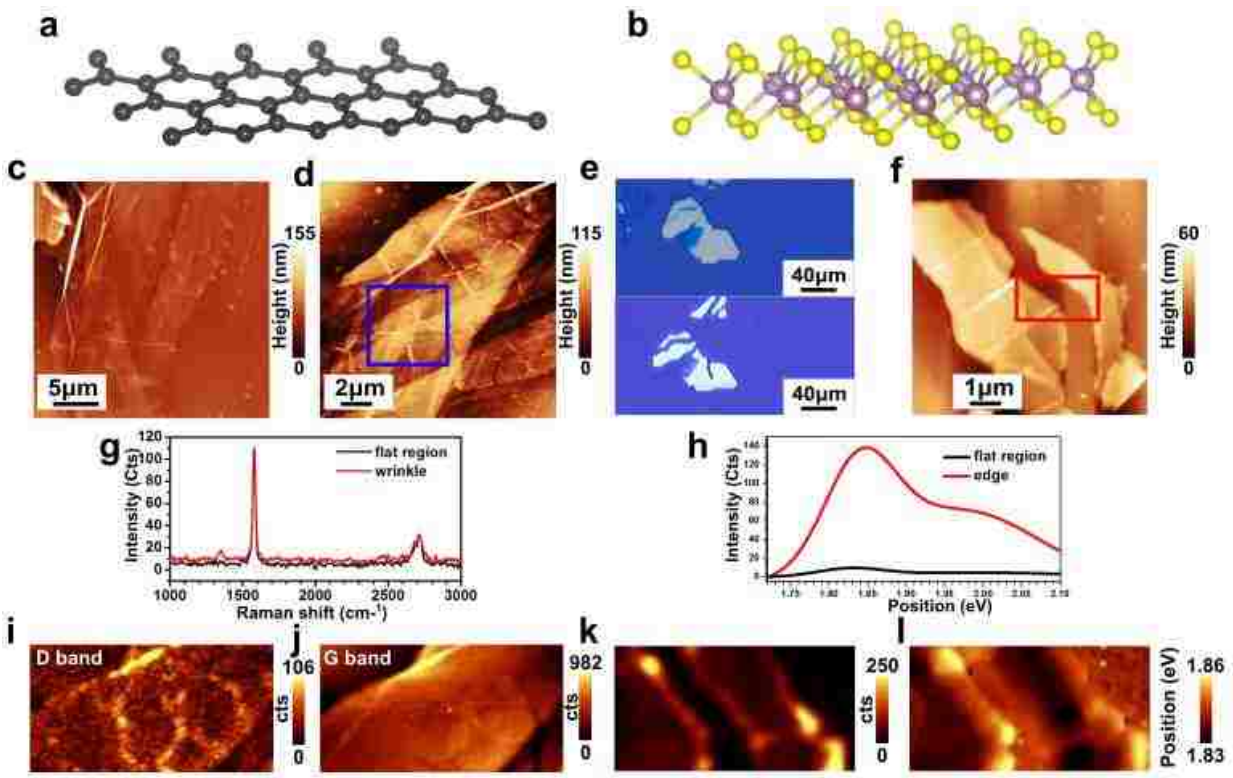

Figure 4–8 Crystal structure of (a) graphite and (b) MoS_2; (c) and (d) AFM morphology image for heat treated few layer graphite flakes; (e) Optical images for MoS_2 flakes before (upper) and after (lower) heat treatment; (f) AFM image for heat treated MoS_2 flakes; (g) Raman spectra of heat treated HOPG flake (h) PL spectra for heat treated MoS_2; (i) D band and (j) G band Raman mapping for heat treated HOPG flakes; (k) PL intensity and (l) PL position maps for heat treated MoS_2 flakes

As shown in Figure 4-8 (c) and (d), the thick graphene flakes (i.e. graphite) before and after heat treatment were characterized by AFM. Similar to the observations on *h*-BN, after heat treatment, all glue and water residues were gone leaving a clean and flat graphene flake. Since graphene also has negative thermal expansion coefficient, heat treatment induced wrinkles can also be observed. However, compared to the wrinkles formed on *h*-BN, the geometric pattern on graphite flakes are not as well-defined as those on *h*-BN.

A typical Raman spectrum from graphene or graphite includes G band (~1580 cm^{-1}), 2D band (~2670 cm^{-1} also known as G' band) and D band (~1350 cm^{-1}). The G band Raman peak originates from the in-plane vibration of the sp^2 carbon atoms (E_{2g} symmetry) and the 2D band originates from a two phonon double resonance Raman process. D band is known as defect-induced Raman band. Thus Raman can serve as a useful tool to characterize structural defects on graphene or graphite. As shown in Figure 4-8 (i), D band Raman map clearly shows high D band peak intensity on wrinkle regions and this further confirms that large density of structural defects are accumulated on wrinkle regions.

We repeated the measurements with MoS_2. Though thermal expansion coefficient of MoS_2 is positive [193,194], we still observed the heat treatment induced changes in the morphology of MoS_2 flakes. As shown by Figure 4-8 (e) and (f), after quenching the MoS_2 flakes developed cracks in regions where pre-cut cracks existed before heat treatment.. Further inspection of the flake by AFM reveals that heat treatment and quenching introduced wrinkles. Figure 4-8 (f) shows one representative flake with heat treatment induced wrinkles. Among all flakes we checked, we found that the wrinkles on MoS_2 exhibited different morphology as they did not seem to follow any crystallographic structure of the lattice. The reason for the wrinkle formation is likely due to the large TEC mismatch between MoS_2 and SiO_2. The TEC for MoS_2 is ~3.1721×10^{-7} K^{-1} along a direction and ~12.3×10^{-7} K^{-1} along c direction at 733K while as the TEC for SiO_2 is ~0.56×10^{-7} K^{-1}, thus during fast heating, the flake would be in global compression strain while during the quenching phase, the flake will be in global tensile strain. Cracks become the stress concentration center during cooling and as a result flakes crack to release the accumulated tensile stress. Figure 4-8 depicts the PL intensity (k) and position (i) mappings of a MoS_2 flake in which both formed wrinkles and cut edges are included. Increased PL intensity can be observed at

wrinkles though the increased PL is not as high as that from the edges. Interestingly, as can be seen on the PL position mapping corresponding to the A exciton, with respect to the PL position from the flat region on the flake, there is a blue-shift of PL peak along the edges of the flake while there is a red-shift of the PL peak near wrinkle regions at the same flake. It has been widely recognized that PL intensity and position can be correlated to parameters including crystal structure and strain. The PL position red-shift at wrinkles indicates the band structure around the K point at wrinkles has been changed so that the direct band gap transition energy is reduced [195]. And the direct band gap transition energy is increased along the cut edges. We propose that the opposite shift of the PL position at edges and wrinkles was because the MoS_2 flake was under different strain conditions, that is, MoS_2 was under tensile strain at edge regions and it was under compression strain at wrinkles. This is consistent with our predicted formation mechanisms for edges and wrinkles during a full cycle of heat treatment (fast heating and quenching). Combining with what we have observed from Raman characterization of wrinkles on graphene, we propose that the heat treatment induced wrinkles not only introduce defects (as indicated by the D band of graphene) but also have accumulated strain (as indicated by PL of MoS_2 flakes).

4.2.4 Conclusions

Our results revealed that the interaction between 2D materials and a substrate can induce defects that were not present in free powder form. Based on our literature review, it is now understood that changes in electronic structure of 2D materials can introduce reactive sites in the material. Hence, we infer that the folds studied in this Case Study exhibit electronic properties that are favorable for reactivity. The specificity of the reactions likely to take place will be further

investigated. In addition the results highlight the potential of strain engineering for MoS_2 to optimize its optoelectronic properties for photocatalytic applications.

Understanding the fundamental properties of folds or point defect formation will help reaching a better control of their production for catalysis. A multi-functional view of how optical, mechanical, electronic and chemical properties at the nanoscale can be affected may reveal new applications for 2D material. Although beyond the scope of this dissertation, a detailed and more comprehensive study of how defects can be used to tune the electronic structure of 2D materials may find exciting applications in rational design for catalysis.

4.3 Case Study Two: Laser-assisted defect engineering in *h*-BN flake samples and subsequent property characterization for catalytic applications

4.3.1 Background and Motivation

The ability to monitor structural and molecular alterations occurring at the different steps of the reactions at the surface of a catalyst, under conditions that are similar to those of the real application, is highly sought after [138]. Evaluating the reactivity of new catalysts using standard analytical methods such as optical spectroscopy (infrared, UV-Vis, fluorescence), x-ray photoelectron spectroscopy (XPS) or mass spectrometry provides important information on the chemical changes, chemical bonds and electronic transitions taking place in the system, under various conditions. However, the readings correspond to the average of the particles present in the micrometer-size volume probed by each instrument. With this, the mechanistic pathways at the surface of a catalyst can hardly be refined for selected defect sites. On the other hand, while transmission electron microscopy (TEM) provides a high resolution view of the structural changes and lattice structure of the materials, its application for *in-situ* analysis [196] and chemical analysis have been rather sparse for 2D materials. Similarly, functional studies at the nanoscale

using scanning probe microscopy (SPM) have been limited outside of Scanning Tunneling Microscopy (STM), carried out under vacuum conditions. Advances in chemical recognition at the nanoscale using recently implemented modules nanomechanical, nanothermal, and nanochemical (IR) of Atomic Force Microscopy (AFM) hold great potential for catalysis, which has not be fully explored.

In this section we report the first time utilization of nanoIR to monitor defect formation and subsequent oxidation on exfoliated sheets of *h*-BN. We first investigate the effect of incoming light power and time of exposure on the dimension of the affected *h*-BN area. We show that spatially localized IR spectra can be acquired with nanoIR with lateral dimensions beyond what can be resolved with optical spectroscopy. With excitation ranging from 1000 to 1800cm^{-1}, we capture the fingerprint of the material that allows us to identify the molecules binding to the defect sites. Lastly we evaluate changes in the morphology and chemical signature of the light-induced defect within the first few minutes of its creation.

4.3.2 Methods

4.3.2.1 Mechanical exfoliation

Few-layer BN flakes were mechanically exfoliated from bulk high purity *h*-BN single crystals (HQ Graphene) using conventional tape cleavage method before being transferred onto clean oxidized Si substrate (250 nm thermal grown SiO_2 layer on top of Si wafer). Initial screening of the *h*-BN layers was performed with optical microscopy (Olympus BX51, 100 x objectives).

4.3.2.2 Defect formation and chemical analysis

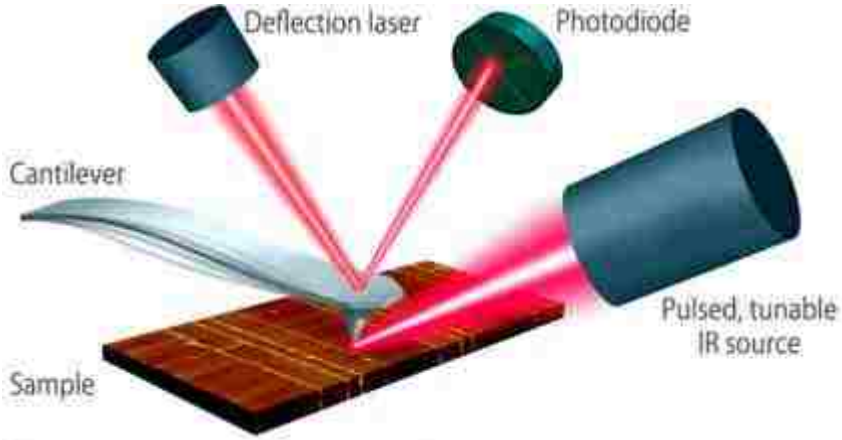

Figure 4–9 Schematic of the AFM-IR configuration on the NanoIR2 platform[197]

Nanoscale measurements were performed on a commercial NanoIR2 platform (Anasys Instrument, Inc., Santra Barbara, CA – now Bruker). The IR source was an OPO laser pulsed at ~1 kHz (~10 ns width) emitting between 1800 and 1000 cm^{-1}. As shown in Figure 4-9, the alignment of the laser, obtained through top-side illumination, was optimized for the focal spot to be aligned with the cantilever tip (App Nano SICONGG-50, spring constant k in the 0.1-0.6 N/m range). Optimization of the alignment indicated a beam size of about 50 nm of the IR laser. Despite the large laser spot, the cantilever tip makes it possible to detect local variations below 100 nm, as discussed in previous studies [198]. The IR spectra were collected at a fixed point by measuring the amplitude of the contact resonance of the cantilever as the illumination wavelength spans from 1000 cm^{-1} to 1500 cm^{-1} in 2 cm^{-1} step. All measurements were performed in air and ambient conditions.

4.3.3 Results and Discussion

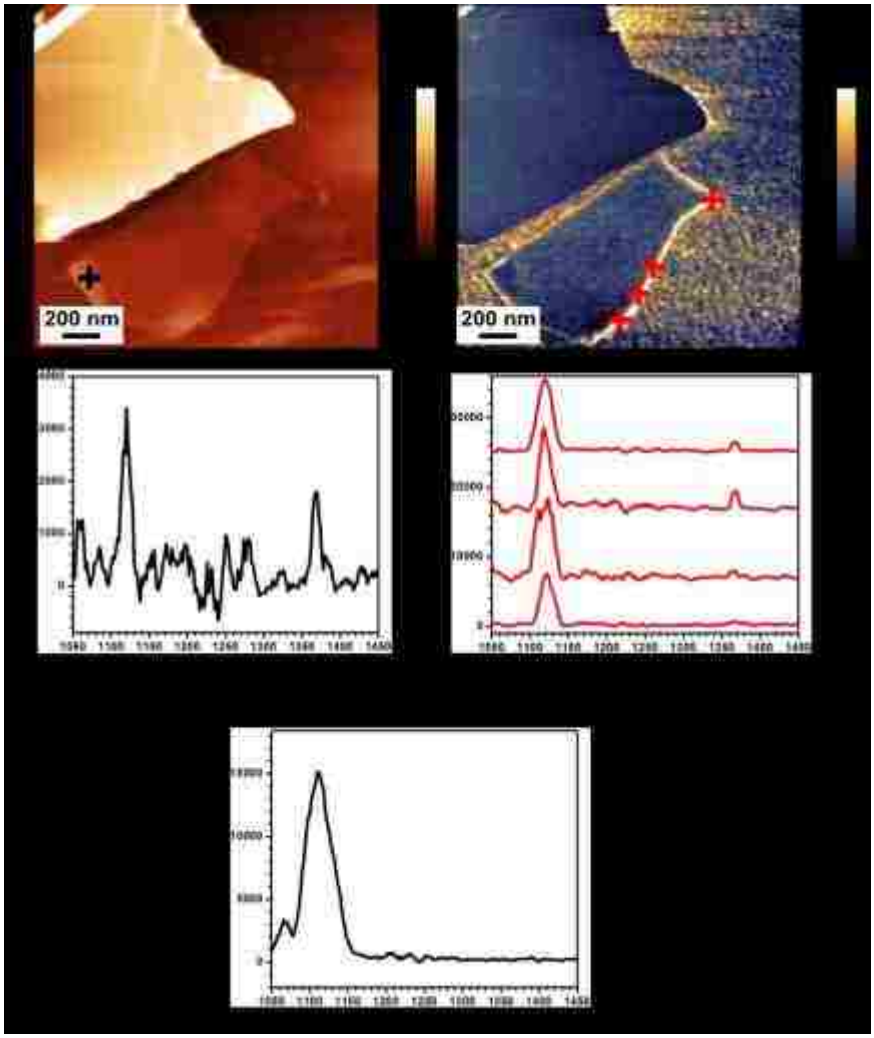

Figure 4–10 (a) AFM topography image of two exfoliated h-BN flakes with different thicknesses; (b) NanoIR spectrum from center region on pristine h-BN flake with the single point indicated by the black cross in (a); c) Nano IR amplitude image recorded at 1365 cm-1; (d) Four NanoIR spectra obtained from edge region on pristine h-BN flakes, their positions are indicated by the red crossed in (b); (e) NanoIR spectra obtained from SiO_2 substrate

Pristine *h*-BN exfoliated on a SiO_2/Si wafer were characterized with nanoscale functional AFM. The morphology of two flakes was captured (Figure 4-10 (a)). One flake was selected for its high

thickness (~ 24 nm) and the other one was selected because of its thickness indicating thin layers (~ 4nm). Initially the IR spectra of the flakes were collected at low power (0.49 % of the full laser power). Details about the experimental settings are provided in the Methods section. To acquire a nanoIR spectrum, the *h*-BN were excited using a pulsed infrared laser (OPO) that is steered to the vicinity of the AFM tip using a succession of flat and curved Au-coated mirrors. The cantilever tip is engaged in contact mode, set for constant force feedback. Using the OPO laser, the pulse is set to 1 kHz, which is well below the resonance of the cantilever ~20 kHz. Each incoming pulse leads to a ringing effect of the cantilever. A representative profile of ringing events was recorded by the position sensitive detector (PSD), is displayed in Figure 4-9. It was previously shown that the amplitude of the ringing captured is directly related to the photothermal expansion of the excited volume of material underneath the tip [199]. The heat then dissipates to the rest of the material or the environment. When analyzing the frequency content of the cantilever ringing using Fast Fourier Transform (FFT), several frequencies corresponding to the contact resonances of the cantilever are identified. The amplitude and the position of the first contact resonance of the cantilever were monitored in this study.

The representative spectrum is presented in Figure 4-10 (b). In the case of pristine flat *h*-BN, at the center of the flake, away from the outer edges the fingerprint exhibited a single IR band at 1365 cm^{-1}. This band corresponds to the transverse optical phonon modes of *h*-BN, as reported in previous studies on *h*-BN [200-202]. For pristine regions of the flake, the FWHM of the peak was ~ 20 cm^{-1}. A careful analysis of the flake revealed another large band in the 1100-1150 cm^{-1} (Figure 4-10 (d)) indicative of an organic contamination of the pristine lattice. This region of the IR spectrum corresponds to the single bond stretching and bending vibrations. To get a clearer idea of the distribution of this signature, we fixed the illumination wavelength at 1120 cm^{-1}. The

map presented in Figure 4-10 (c) indicates a strong signal at the edges and corners of the flake. The reference spectrum of the substrate was collected for reference (Figure 4-10 (e)) and indicates that although the substrate exhibit a band in this region, the fingerprint at the edges of the *h*-BN pristine flake is significantly stronger and exhibits a different pattern. Our results are in fact indicative of edge passivation at the edges of the flake. To the best of our knowledge, this is the first report of nanoscale chemical analysis of local defects on 2D materials.

Next, we investigate the formation of local defects in the flat region of the pristine flakes upon increasing the laser power. Figure 4-11 (i) indicates the IR spectra collected at six successive locations of the *h*-BN flake at increasing laser power. All other parameters remained constant. The spectra indicate the clear dependence of the changes in the *h*-BN band ~ 1365 cm^{-1} and in the 1050-1150 cm^{-1} region.

We note that upon increasing laser power, a shift in the cantilever contact resonance of a few kHz could be resolved. This is of interest for chemical mapping application as nanoIR can use frequency shift to monitor changes in the material, which may enable faster data acquisition in the future. The topography image of the region of the flake affected by the laser treatment revealed a few damaged locations. We note that the defects created are localized to the vicinity of the tip. This indicates that the confinement of the light at the tip of the cantilever and the force applied onto the sample may play a significant role in the defect formation. The laser effect alone would create a defect of ~ 50 nm. Next we obtained chemical maps at selected wavenumbers (Figure 4-11 (b)-(h)), corresponding to the different bands identified after deconvolution of the spectra. The chemical images indicate differences between the local defects.

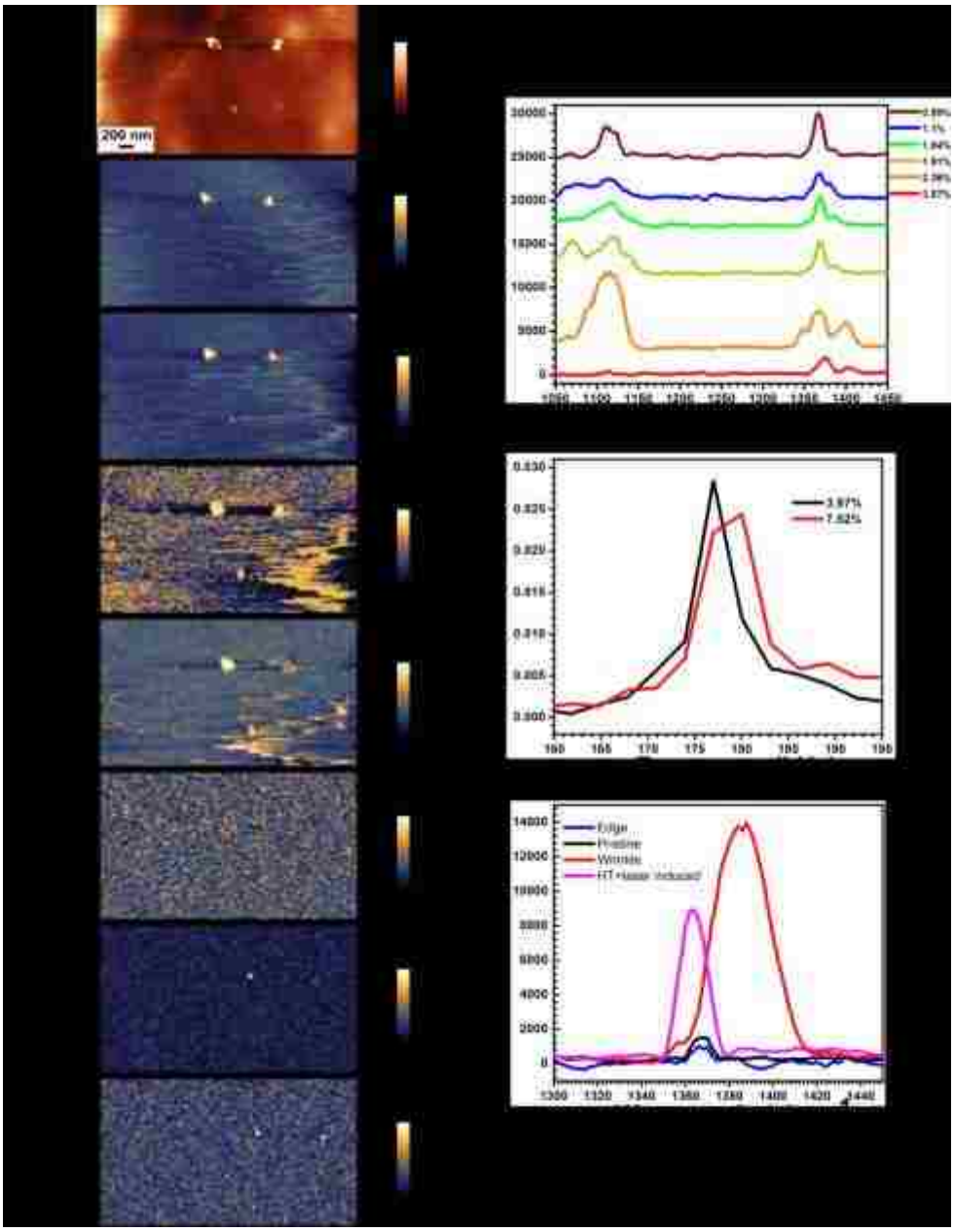

Figure 4–11 Laser-induced defect formation on *h*-BN flake. (a) AFM topography image of *h*-BN flake surface after laser induced defect creation (b-h) NanoIR amplitude maps obtained at wavenumbers; (i) NanoIR spectra acquired with laser power 3.97% (red), 2.36% (orange), 1.91% (yellow), 1.84% (green), 1.1% (blue), 0.99% (wine); (j) Frequency spectra acquired after laser was on for 30 sec at laser power 3.97% and 7.52%; (k) NanoIR spectra from flat region, edge region, wrinkle region and laser-induced defect region

Lastly, we investigated changes in the chemical signature detected at the defect site as a function of time. We first acquired a spectrum with illumination power below the threshold for defect creation (Figure 4-12). Next we acquired the spectrum at the same location with a high laser power. The signature indicates several bands. As the laser step by step data acquisition takes a few minutes to complete, the next spectrum was acquired a few minutes after the initial defect creation. The spectrum evolved significantly. We also note that the defected region exhibits a slightly higher contact resonance frequency than the pristine layer.

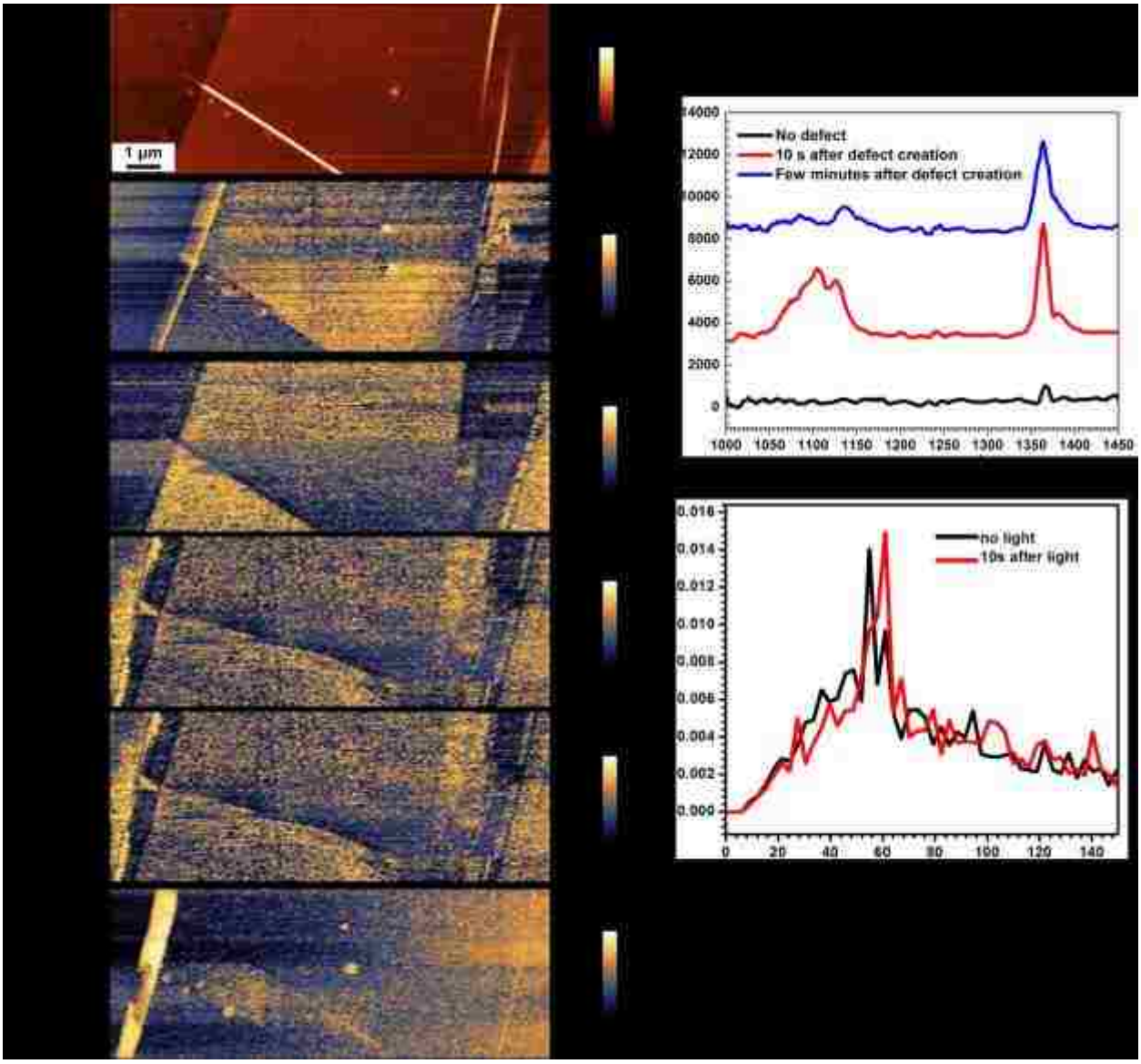

Figure 4–12 Reactions over laser induced defect sites. (a) AFM topography image of BN flake with laser induced defect sites; (b-f) NanoIR amplitude maps obtained at different wavenumbers; (g) NanoIR spectra acquired from the same position at two different time points; (f) Contact resonant frequency of the AFM cantilever showing the frequency shift

4.3.4 Conclusions

We have demonstrated the employment of NanoIR for monitoring localized defect creation and subsequent defect-molecule interactions on h-BN flakes. We have established the protocol of creating defects with different lateral dimensions by localized laser irradiation with different laser powers. We showed that the IR mode indicative of the lattice vibration in h-BN widens which is due to the structural imperfection. We also report the emergence of new bands in the range of 1000 to 1800 cm^{-1} which is most likely from the organic molecule binding to and reacting with the defect sites. By capturing the spectra evolution after defect creation, we monitored the defect induced chemical signature changes on *h*-BN after laser illumination.

4.4 Summary and Future Perspectives

In case study one, nanoscale spectroscopy and functional imaging techniques have been shown to be very powerful methods of studying localized material properties in order to identify the underlying mechanism(s) for their catalytic properties. The correlative AFM and ToF-SIMS characterization results support our hypothesis that defects become active sites for selected chemical reaction and long hydrocarbon chains form on the active defects. We would like to emphasize that advanced AFM-based platforms correlative with ToF-SIMS constitute a new experimental approach to understand the catalytic mechanisms at the nanoscale, thus bridging the gap between molecular-level theoretical modelling and reactor-scale studies of the reactions. In case study two, we demonstrate further the application of an advanced AFM-based nanospectroscopic technique, i.e., NanoIR, to enable the localized defect creation in a controlled way and subsequent localized spectral acquisition revealing the changes of *h*-BN flakes as the reactions are happening at defect sites. We note that the installation of environmental control chamber which will allow us to send selected gas molecules inside the chamber in a controlled

way to better understand defect-molecule interactions as different gas molecules interact with defect laden *h*-BN flakes. Secondly, in order to better understand the reactions themselves and capture the intermediate reaction steps, the installation of fast lasers and detection schemes will be necessary.

5 ADDING TO EXISTING AFM MODULES FOR ENERGY AND CATALYTIC STUDIES

5.1 Background

Nanoscale capabilities to explore structures and functional properties of complex systems both at their surface and in their volume are defining the type of systems or processes that can be studied. For energy devices and catalysis, features such as time resolution or subsurface functional imaging would be appealing. However, great strides in instrumentation will be required to deliver such platforms.

For instance, subsurface developments have been reported for AFM[9] but mostly for detecting heterogeneities, cracks and defects below the surface. Approaches that would enable more advanced explorations of chemical or electrical properties for heterogeneous functional materials such as active layers of solar cells would open new avenues for the fundamental understanding of the nano-to-device connections.

For catalysis, the ability to locate and identify few organic molecules on the 2D material flakes, as well as monitoring the reactions taking place at various defects site would be powerful. However, it would require high resolution and high sensitivity measurements, with the need for a recognition mechanism such as infrared or force spectroscopy.

Although reaching such a level of instrumentation is clearly out of the scope of the present work, in this chapter, we will present some of the attempts we have made in developing proof-of-concept measurements that will constitute the basis for future lines of research in these areas of instrumentation. First we will report on a light-assisted AFM-based nanomechanical spectroscopy platform for monitoring minute changes in metallic nanostructures. Next, we will

describe our initial steps toward introducing multifrequency AFM to synthesize new operational modes in the AFM-tip dynamics, for used in imaging and nanoscale infrared spectroscopy. Lastly, we will provide a perspective of the developments, their advantages and limitations, and the remaining goals for nanoscale instrumentation.

5.2 The development of light-assisted AFM-based nanomechanical spectroscopy with a case study of light-matter interaction of nanoparticles

5.2.1 Background and Motivation

The ability to explore light-matter interactions with nanoscale spatial resolution holds great promises to advance material sciences, optoelectronic device optimization, and fundamental understanding of nonlinear dynamic processes at submicrometer scales. As AFM has recently been used to overcome the inherent diffraction limits associated with conventional optical spectroscopy, we demonstrate here the advantages and limitations of several AFM modes including contact mode, PFM and nanothermal analysis (nanoTA) to study light-matter interactions locally in gold (Au) nanostructures under continuous illumination. We show that photothermal expansion resulting from photon absorption in Au can be detected by PFM, but not with simple topography. The onset of Au softening was detected by PFM while increasing laser illumination power. Based on one dimensional diffusive heat flow calculations, the spectral changes recorded could be related to the average temperature of a single nanoisland. Our analytical predictions were confirmed by nanoscale thermal analysis. Nanoparticles and plasmonic nanostructures exhibit unique properties in photo-catalysis [203,204], material sciences [205], device engineering [206-208] and biology [204,209-212]. Nano-systems have also been engineered based on their mechanisms of light absorption and plasmonic excitation in metallic nanoparticles (NPs) so as to absorb in selected regions of the visible or near-infrared ranges [213]. Light

absorption in a plasmonic nanostructure often leads to high light-to-heat conversion efficiency [214], a property that can be exploited to develop functional systems such as nano-heaters for photothermal therapy [215,216].

Although heat transfer considerations cannot always be used to explain the local heating emanating from individual nanoparticles, fundamental studies of photo-induced temperature variations have been reported [217], in part due to an evolving desire to control the function of NPs in cells for medical applications or plasmonic devices. However, *in-situ* measurements of photothermal expansion of NPs and dynamic processes resulting from temperature increase with nanoscale spatial resolution remains challenging. Few reports suggest that optical measurements such as scattering spectroscopy can be used to detect changes in temperature in gold (Au) NPs [218,219]. Using white light scattering, Hashimoto et al. monitored spectral shifts of NPs response, which could, in turn, be correlated to temperature changes. The onset of nanoparticle softening was observed by investigating light scattering as a function of laser power [220].

Atomic Force Microscopy (AFM) is another possible approach used to characterize metallic NPs and nanostructures. Until recently, AFM studies were mainly considered to determine morphology. Few dynamic measurements were reported, such as the dynamic Au nanostructures assembly using thermal treatment [221]. Scanning probe microscopy-based platforms, including scanning near-field optical spectroscopy (SNOM) [222], were also used to study plasmonic structures and their behavior in the excited state. However, one of the limitations of SNOM is the development of tips suitable for light collection and the modeling usually required to interpret sample-tip and light-tip interactions. Most recently, photothermal-induced resonance (PTIR) [223] was employed to probe the photothermal expansion of activated plasmonic structures with nanoscale resolution indicating “hot spots” in the structures, which were found to correspond to

the predicted regions with high field enhancement, corresponding to resonances and hybridization of different collective modes in the structures designed [223]. The emergence of nanoscale infrared spectroscopy based on photothermal detection [197,224-227] has drawn some interest for a more detailed understanding of photo-induced response in materials. As a result, various approaches including cantilever resonance tracking [197] or multi-frequency actuation [227] have been reported. However, a comprehensive comparison of the sensitivity of the different detection schemes that can be used to study photo-induced processes remains mostly unchallenged. This is of prime importance given the need to adapt capabilities to the requirements and conditions of the systems of interest in materials or life sciences.

In this section, we study the performance and sensitivity of static (Figure 5-1 (a)) and dynamic AFM detection schemes (Figure 5-4 (a)) for monitoring the power-dependent behaviour of plasmonically active Au nanostructures at the nanoscale. Au nanoislands were deposited using thermal evaporation followed by a thermal treatment to tune the absorption profile by affecting the size of the nanostructures, while maintaining a structure with finite volume. The characteristics of the Au structures make quantitative interpretation of the AFM data acquired more accessible. The results unveil a laser power dependence of the photothermal response, which could be quantified using the diffusive heat equation. The results highlight the wealth of information that can be extracted from AFM measurements and point out interesting differences between the static and dynamic detection modes.

5.2.2 Methods

5.2.2.1 Sample preparation

Au nanoislands with diameters and thicknesses in the nanometer range were prepared by thermal evaporation. Thermal evaporation was performed in vacuum environment ($1.2x10^{-6}$ Torr). The nanostructures were deposited on glass slides that were freshly cleaned using acetone and isopropanol under sonication for 20 min. A nominal thickness of around 5 nm was deposited. After evaporation, the samples were annealed for 30 min in a furnace at 473.15 K (200˚C), 573.15 K (300˚C) and 673.15 K (400 ˚C) to reach a more monodispersed size and improve the roundness of the nanostructures. The samples were then cooled to room temperature in ambient conditions. UV-VIS spectroscopy (Varian Cary 100 scanning UV-VIS spectrometer) was performed to determine the absorption range of the nanoislands (Figure 5-1 (b)).

5.2.2.2 AFM-based platform for photo-induced measurements

A custom AFM platform was adapted on a WITEC Confocal Raman-AFM system to measure local light-matter interactions. The sample illumination was set up using a 20X objective (Zeiss, NA=0.4) to focus a continuous wave (CW) 532 nm laser onto the sample at the tip of the AFM cantilever. The laser spot diameter after the objective was around 0.8 μm.

Laser illumination on the nanoislands induced a significant thermal expansion, which was monitored using AFM. AFM cantilever deflection was measured by engaging the tip in contact mode. Force curves representing the mechanical response of the sample were captured with PFM [228]. As discussed in Chapter 2, PFM is a mode of AFM specially designed to apply a sinusoidal modulation of the z-direction of the cantilever piezo-component at a frequency that is much lower than the resonance frequency of the cantilever (~1 kHz) with an amplitude in the 10-500 nm range [228]. The amplitude is controlled so that the displacement of the tip ranges from a

position where the cantilever is free to a position where the tip applies a small indentation on the sample. A force-time curve is acquired for each cycle (Figure 5-4 (a)). By capturing a force curve at selected points and by performing post-processing calculation of the slope, indentation and integration of the retract curve, it is possible to map the stiffness and adhesion maps corresponding to the topography, as shown in Figure 5-4.

5.2.2.3 Nanoscale thermal analysis (nanoTA) measurements

Nanoscale thermal analysis measurements were performed using the nanoTA module of AFM NanoIR2 (Anasys Instrument, Inc., Santa Barbara, CA). A typical AFM contact mode height image was first acquired to identify the areas of interest. NanoTA profiles were obtained by monitoring the cantilever deflection while heating the thermalever probes by increasing the applied voltage. Thermalevers are designed to heat the material in the vicinity of the tip-sample contact. As softening takes place, a change in the slope of the deflection vs. voltage curve can be observed. Calibration of the temperature was performed using three polymers with known melting points: polycaprolactone (PCL, T_m = 328 K), polyethylene (PE, T_m = 389 K), polyethylene terephthalate (PET, T_m = 508 K). After recording the nanoTA profiles of PCL, PE and PET, the curve representing deflection as a function of melting points is used to convert the heating voltage axis into a temperature axis.

5.2.2.4 Cantilever probes

ACCESS-C cantilevers (AppNano) were used for the contact mode study while ACCESS-FM (AppNano) were used for PFM and PR-EX-AN2-200 thermalever probes (Anasys Instrument, Inc.) were used for the nanoTA measurements.

5.2.3 Results and Discussion

The Au nanoislands used for our photothermal measurements were obtained by thermal deposition and annealing at 673 K (400 ˚C) (blue curve in Figure 5-1 (b)). This sample was chosen because of its narrower absorption peak, indicative of a more monodispersed size distribution compared the samples annealed at 573 K and 473 K. In addition, the absorption peak was centred at 530 nm, which is optimal for the 532 nm illumination source of our setup. AFM topography images (Figure 5-1 (c)) showed nanoisland diameters varying from ten to two hundred nanometres despite our effort to reduce the variations. However, the stability of the sample in air allowed us to carry out all the light-induced measurements without changes in the morphology of the sample.

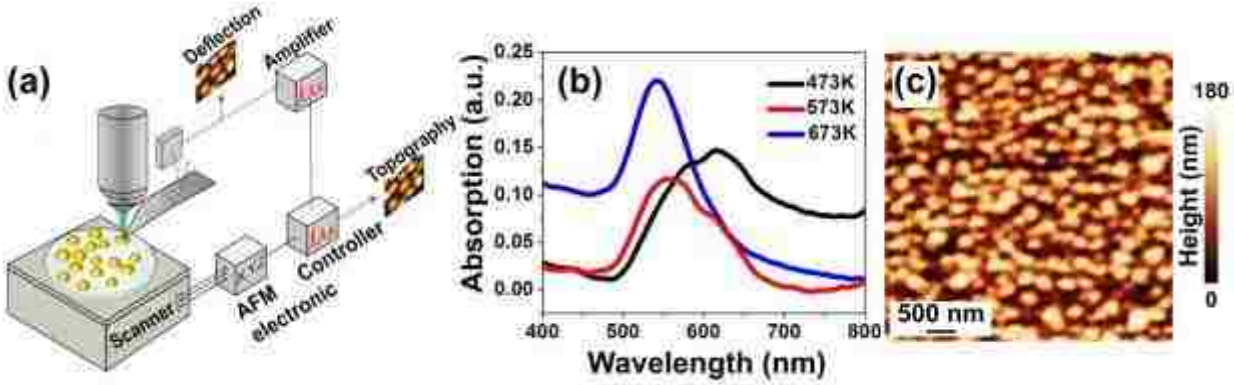

Figure 5–1(a) Custom AFM platform for photo-induced nanoscale measurement with 532 nm laser illumination, (b) UV-Vis absorption spectra of Au nanoislands annealed at 473 K (black), 573 K (red) and 673 K (blue), (c) AFM topography image of the nanoislands annealed at 673 K.

5.2.3.1 Photothermal expansion detection in contact mode

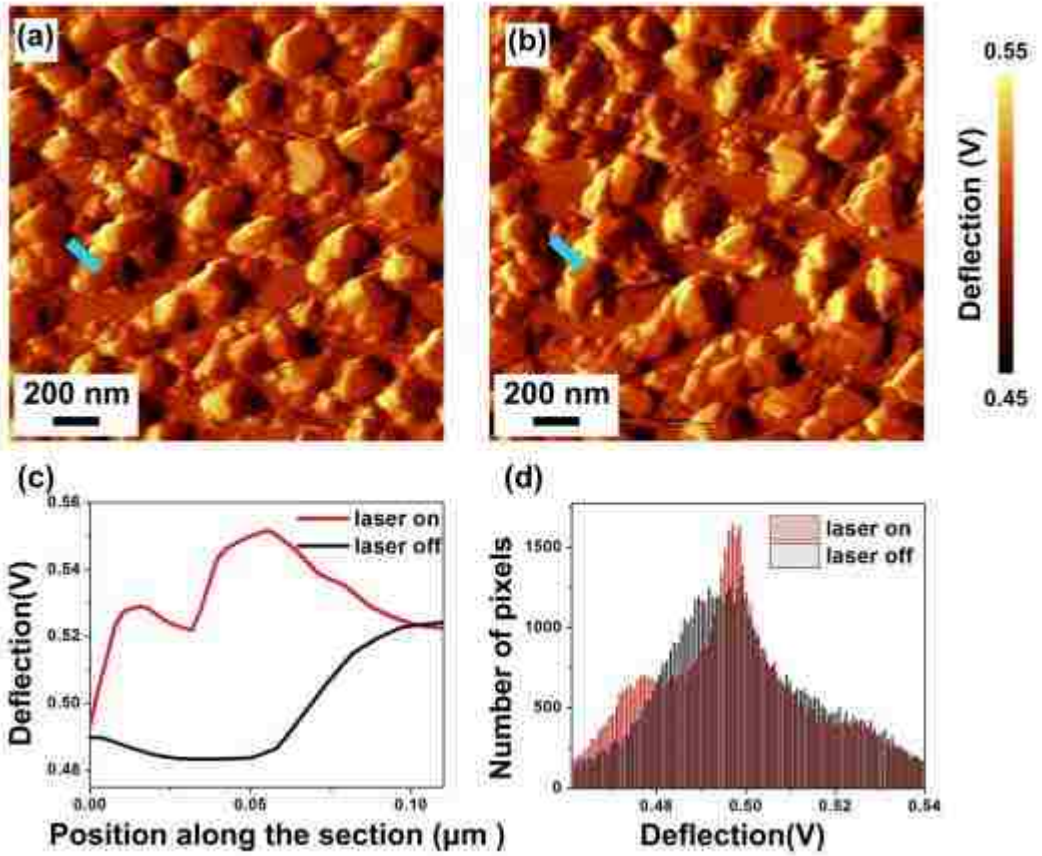

Figure 5–2 Photothermal expansion of the nanoislands detected in contact mode. (a,b) Deflection map with laser off (a) and on (b). (c) Deflection profile of the nanoislands indicated by the light blue mark in (a) and (b). (d) Histogram representing the deflection measured across the image with laser off (black) and on (red).

We first carried out measurements in static mode, with the cantilever engaged in contact mode. The setup is presented in Figure 5-1 (a). The static deflection of the cantilever in the Z direction (perpendicular to sample surface) was monitored by recording the “Top-Bottom” signal of the AFM position sensitive detector (PSD), without and with laser illuminating the nanoislands. The deflection images captured before illumination and as the sample was illuminated are presented

in Figure 5-2 (a) and (b), respectively. Laser power was slowly increased before capturing the image presented in Figure 5-2 (b) in order to visualize changes in the nanoislands while avoiding any permanent damage in the sample. Powers of 1.03 mW was used for the measurements presented in Figure 5-2 and Figure 5-3. Although the variations observed between the two deflection maps was initially attributed to the photothermal expansion of the Au nanoislands, further analysis of the data using a quiver (or velocity) plot indicated that the changes are more likely originating from drift in the system. As a result of the photothermal expansion, a force is exerted on the tip in contact with the surface, thus deflecting the cantilever.

Nonetheless, a careful analysis of the maps suggested that large expansions could be observed at specific locations of the sample: as represented by the profile extracted at one such region in Figure 5-2 (c), the deflection across a single island without illumination (black) and with illumination on the particle (red) can be recorded to calculate the local expansion of the nanoislands. A histogram representation of the height measured (Figure 5-2 (d)) shows that the absolute values of deflections shifted to higher values as a result of the illumination. This is in agreement with the broader areas of the contours as marked in Figure 5-3, which represents the topography/height of the nanoislands, acquired simultaneously.

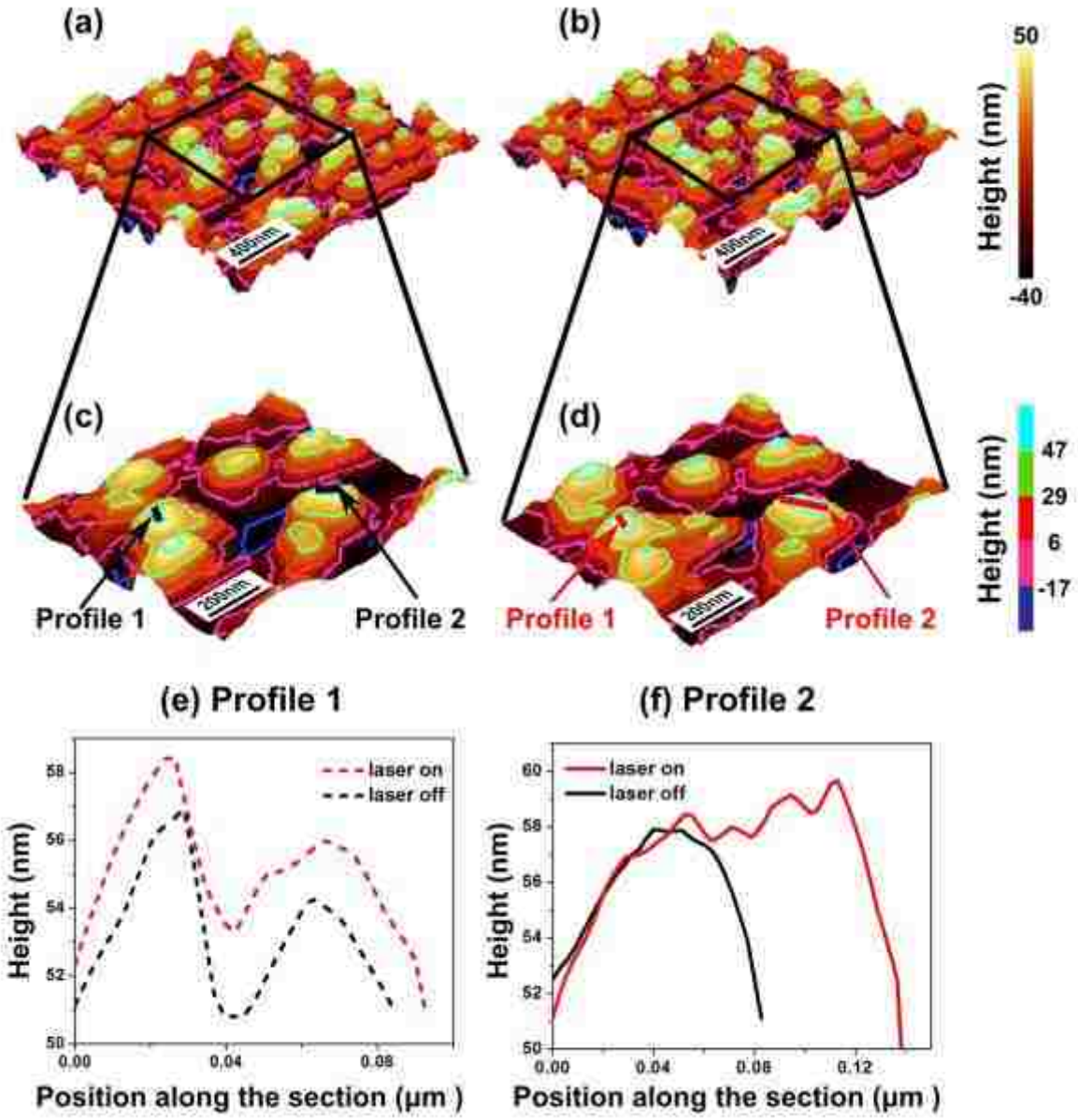

Figure 5–3 3D representation of Au nanoislands topography for laser off (a, c) and on (b, d). The area at the center in (a) and (b) corresponds to the Au islands with the largest photothermal expansion. (c) and (d) show the respective high resolution morphology in (a) and (b) with selected height contours. (e) and (f) are the profiles for the two selected contours with laser off (black) and laser on (red).

Figure 5-3 (a) and (b) are 3D representations of Au nanoislands topography for laser off and laser on, respectively. Figure 5-3 (c) and (d) are high resolution morphology images for Figure 5-3 (a) and (b), respectively. Contour analysis of the height images was performed, as shown in Figure 5-3. The isolines were selected in increasing order: purple blue (-40.12—17.03 V), fuchsia (-17.03-6.07 V), red (6.07-29.16 V), green (29.16-47 V), light blue (47-50.25 V). The contours illustrate the illumination-induced expansion measured across the sample's nanoislands. Similar to what is observed in deflection images (Figure 5-2 (a) and (b)), the photo-thermal expansion across the sample was non-uniform. These variations in photothermal expansion may be explained by the variations in shape and dimensions of the nanoislands that is dependent on the size and angles of the structures, thus exhibit varying response for our fixed 532 nm excitation.

For Figure 5- 3(c) and (d), two contour regions in the light blue isoline were selected for quantitative profile comparison. The extracted profiles are plotted in Figure 5-3 (e) and (f). As shown in Figure 5-3 (e), the diameter and the height of the nanoislands on the left (profile 1) increased with laser on. For the nanoislands on the right side (profile 2), the broadening is more dominant compared to the height increase and this is confirmed by the profile in Figure 5-3 (f). Nonetheless, these results indicate that it is possible to detect local photo-induced response of Au nanoislands using contact mode AFM in selected places, although overall drift may interfere with the readings. The spatial resolution of this measurement was found to be similar to that of the AFM system.

5.2.3.2 Photo-induced change in mechanical property

Next we evaluated the sensitivity of PFM measurements. PFM has been most commonly used for studying local deformation and adhesion resulting from interactions at varying tip-sample

distances. As shown in Figure 5-4 (a), stiffness of the material can be calculated by extracting from the slope of a PFM curve. Adhesion between the tip and the surface of the sample can be measured by the absolute value of the difference between the lowest point of a PFM curve and the baseline, as indicated in Figure 5-4 (a). No obvious photo-induced variation in adhesion could be observed in our measurements.

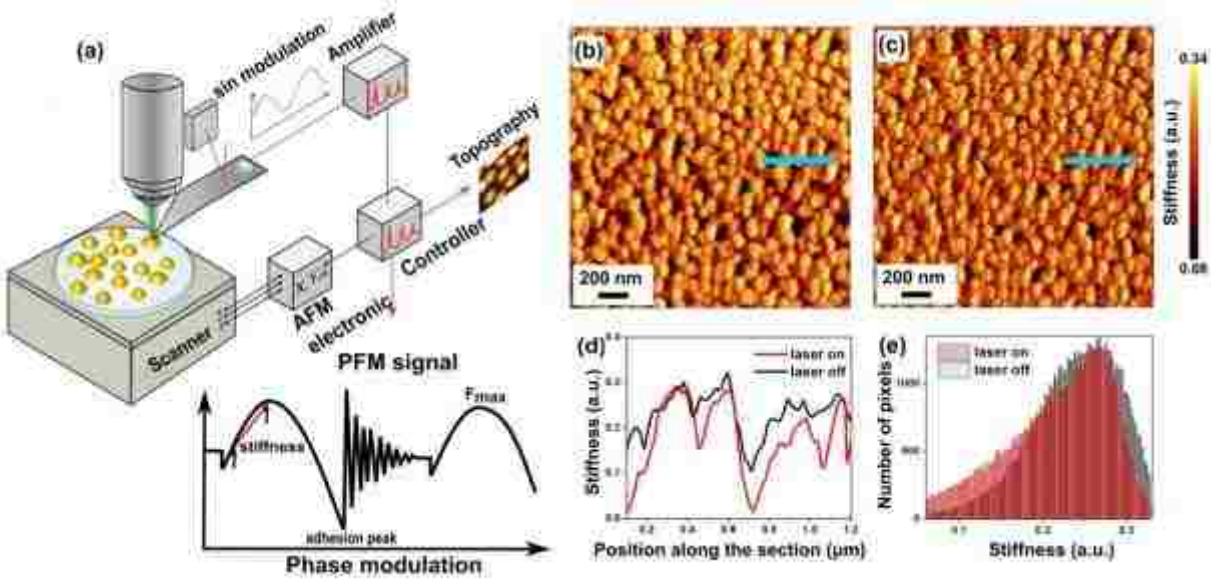

Figure 5–4 Photo-induced change in mechanical property measured with PFM. (a) PFM platform customized for photo-induced laser at 532 nm. Standard PFM force curve is depicted. (b, c) represent the maps reconstructed by calculating the slope of the PFM curve at each point of the image, with laser is off (b) and on (c). (d) PFM profiles extracted from maps in (a) and (b), respectively. (e) Histogram of the stiffness distribution for laser off (black) and on (red)

In the following section, we focus on the variations in mechanical response of the nanoislands as a result of illumination. The PFM data acquired on the nanoislands without and with illumination is presented in Figure 5-4. The maps presented in Figure 5-4 (b) and (c) were obtained by

analysing the 3D array of data points. The image was constructed by calculating the slope of each approach force curve. The cross-section in Figure 5-4 (d) represents the variation in slope measured across the sample along the light blue section line indicated in Figure 5-4 (b, c). Direct comparison of the PFM profiles indicates a significant change of the slope upon illumination (laser power 1.03 mW) of the samples. Such a change suggests a softening of the material upon illumination. This was confirmed by the histogram representing the variation in slope measured across the sample (Figure 5-4 (e)), with a decrease of the number of pixels with the highest slope and an increase in the number of pixels with the lowest slope. Similar to the deflection measurements obtained in contact mode, the study reveals that the changes are not uniformly distributed, which is consistent with the inherent morphology heterogeneities in the Au nanoislands.

5.2.3.3 Laser power dependence of the Au nanostructure softening

The softening of the material was further investigated by considering the laser power dependence of the Au nanoislands softening. Successive PFM curves were acquired at a single point while increasing the power of the incoming laser illumination. Nanoislands exhibiting strong photo-induced variations in the PFM images were selected for this measurement. We first ensured that the expansion detected is purely from the sample and not from incoming light interacting with the AFM cantilever. For this, PFM curves were acquired on glass, using identical setup and parameters as the ones used for the nanoislands measurements. Glass was selected due to its low absorption at 532 nm and its low photothermal response. The curves obtained on the glass slide are presented in the Supplementary Material. No change in the force curve slope was observed despite the increase in laser power.

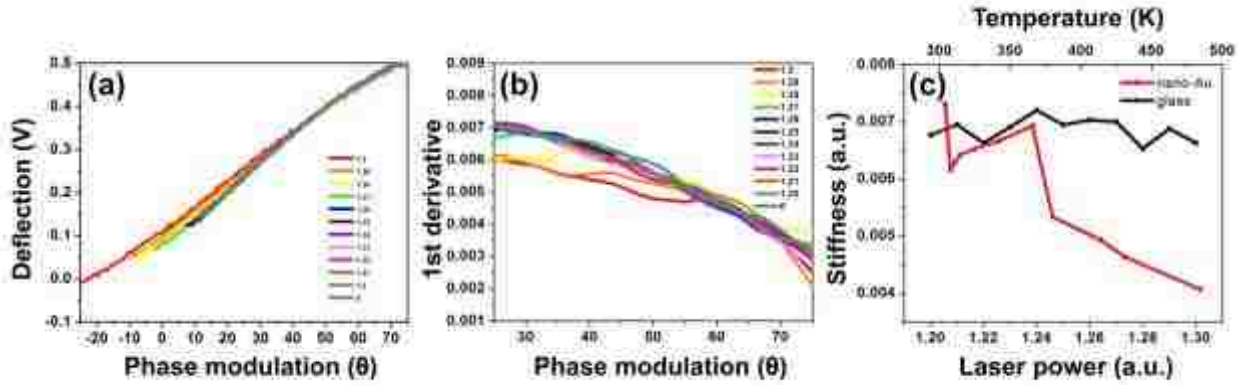

Figure 5–5 Laser power-dependent PFM measurements on Au. (a) Slope of the approach curve measured with PFM at increasing laser power. (b) First-derivative of the curves presented in (a). (c) Temperature dependent stiffness of glass substrate (black) and Au (red).

On the other hand, an important variation of the slope was observed in the force curves as a result of increasing laser power (Figure 5-5 (a)). The first derivative of the curves (Figure 5-5 (b)) highlights the differences in the material response at different temperatures. The highest slope was found at low laser power while the lowest slope was measured for the highest laser power. The slope of the approach curves within the range (phase modulation 10 to 25 ˚) was plotted in Figure 5-5 (c). While no change in the slope was found for the measurements performed on the glass slide (black curve), a significant decrease in the slope was observed on the nanoislands (red curve). A large decrease in the slope can be observed around power 1.03 mW. Based on previous reports such as Hashimoto et al. [220], we attribute this change to a softening of the nanoislands suggesting a significant temperature increase resulting in a melting-like behaviour of the islands.

The temperature of the nanoislands associated with each laser power could be estimated using the one dimensional diffusive heat flow equation for a homogenous medium (Au):

$$k\nabla^2 T(x,t) + \frac{dq}{dt} = c\frac{\partial T}{\partial t} \quad (4)$$

where k is the thermal conductivity, $T(x,t)$ is the temperature field, c is the heat capacity per unit volume and $\frac{dq}{dt}$ is the heat flux generated by heat gradient.

As per the considerations described by Keblinsky et al. [229], this equation can be used to approximate the temperature of the nanoislands. The temperatures predicted using the experimental data and the one-dimensional diffusive heat flow equation are presented in Table 5-1.

Table 5-1 Summary of calculated laser power density P, laser peak power density I_p and particle temperature T_p

Laser power (a.u.)	**Laser power (mW)**	**Laser power density (mW/μm^2)**	**Laser peak power density (mW/μm^2)**	**Particle temperature (K)**
1.2	0.24	0.117874132	0.212264245	304.1
1.21	0.38	0.18800178	0.338548036	307.8
1.22	0.51	0.254150554	0.45766679	311.2
1.23	0.63	0.314828377	0.566933616	314.3
1.24	1.0	0.512279982	0.922498617	324.6
1.25	1.7	0.830589873	1.495701641	341.2
1.26	2.6	1.303081119	2.346549881	365.7
1.27	3.2	1.576628682	2.83914623	379.9
1.28	4. 5	2.223195649	4.003464873	413.5
1.29	5.1	2.556426317	4.603536789	430.9
1.3	7.2	3.580986281	6.448534023	484.1

Based on our calculations, we found that the sharp deviation of the slope occurs around 375 K, which is in agreement with the order of magnitude reported by Hashimoto et al. In the aforementioned study, a sharp change of scattering spectral shifts was measured around 550 K for nanoparticles about 150 nm in diameter [220]. The phenomenon has been attributed to the initiation of surface melting in the nanostructure. While our estimated 375 K is lower than the melting temperature of bulk gold (1337 K [220,230]), it is consistent with previous demonstrations that conventional melting mechanism for bulk gold is no longer valid when the dimensional scale decreases to nanoscale. Different melting mechanisms have been proposed. Here we consider the liquid skin melting (LSM) model [231] to interpret our data, as illustrated in Figure 5-6. LSM, also known as surface pre-melting, assumes a nanoparticle to exhibit a core-shell structure. Under this assumption, a liquid-like layer (shell) can be formed when the system is heated at temperatures T_i much lower than the bulk melting temperature T_m, while the core remains solid. The entire particle finally melts at higher temperature, which could be observed in our study when high laser powers were used.

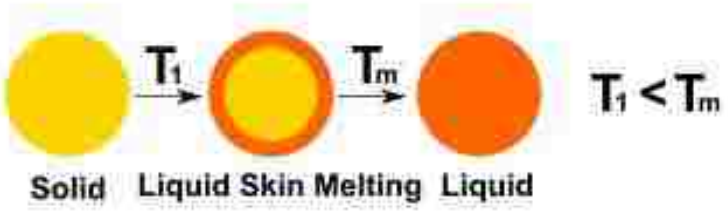

Figure 5–6 Liquid skin melting mechanism model illustrating the temperature dependent softening of Au nanoparticles shell at $T_1<T_m$ before complete melting of the structures at or above T_m.

5.2.3.4 Nanoscale thermal analysis of Au nanostructure softening

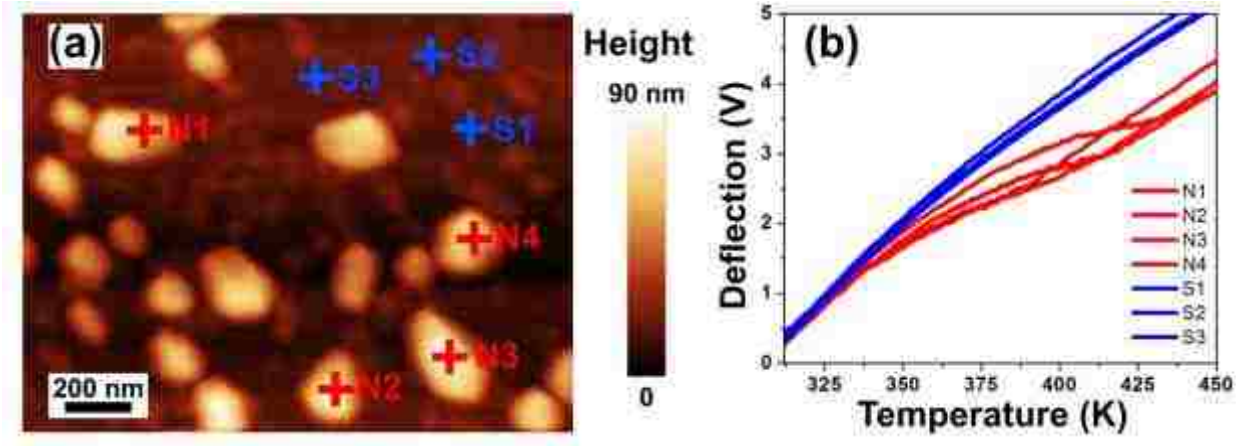

Figure 5–7 Nanoscale thermal analysis of Au nanostructure softening. (a) AFM height image of Au nanoparticles deposited on glass substrate. (b) Deflection vs temperature plots at positions marked in (a).

Nanoscale thermal analysis (nanoTA) was employed to locally heat the nanostructure in order to measure the subsequent softening of the material at the point of contact. The temperatures indicating a softening of the material were compared to the theoretical values calculated for the PFM measurement. Spectra N1 to N4, in red in Figure 5-7, were obtained on Au nanostructures whereas spectra S1 to S3, in blue in Figure 5-7, were acquired on the glass substrate for reference. The increasing deflection of the cantilever in contact with the Au corresponds to the increasing thermal expansion of the sample. The change in behaviour in the range 350-400 K is in good agreement with the changes observed with PFM. The nearly linear spectrum acquired on the glass substrate confirms that no softening was detected within the same temperature range.

After the nanoTA spectrum acquisition, the same area was imaged and no obvious morphology change was observed. The results indicate that the softening events detected constitute a reversible process that differs from the melting of the material, in which long range order of

atoms would no longer exist. This is also in agreement with the temperature differences observed between bulk (1337 K) and nanoscale systems (much lower than 1337 K).

5.2.4 Conclusions

Our study shows that static and dynamic AFM modes can be used to locally study photo-induced processes in plasmonic nanostructures. Deflection measurements indicated that the local response of nanoislands prepared by thermal evaporation and annealing at 673 K was heterogeneous, with selected regions exhibiting large expansion (deflection increase) upon illumination while leaving others barely affected by the light. Overall photothermal expansion could not be confirmed from our velocity plots, which constitute a limitation of the approach.

On the other hand, force microscopy revealed a softening of the nanoislands at temperatures below the melting temperature of bulk gold whereas no change in adhesion could be detected. Note that mathematically, the first derivative calculation associated with the slope can contribute to increasing the sensitivity of the technique. The softening observed around 375 K was attributed to the nanoscale nature of the system, and could be modelled by the liquid skin melting of a core-shell particle, in agreement with previous reports. The findings were confirmed by nanoscale thermal analysis.

5.3 Multifrequency AFM and its combination with NanoIR spectroscopy

5.3.1 Background and Motivation

The development and implementation of multi-frequency AFM, such as bi-modal AFM, intermodulation AFM or mode-synthesizing atomic force microscopy (MSAFM), have paved the way to further advances toward improved spatial resolution, faster data acquisition and more precise measurements of material properties at nanoscale [232]. In MSAFM, an AFM cantilever is

vibrated at a frequency f_p when it is in contact with the sample surface, while as the sample is vibrated at a frequency f_s [8]. New modes can be generated in the tip-sample dynamics due to the nonlinearity of the interaction. It has been established that the new synthesized mode can be used to obtain a range of surface and subsurface information about the scanned sample[8,232] However a direct comparison of their performance with well-established commercial capabilities has not yet been fully considered.

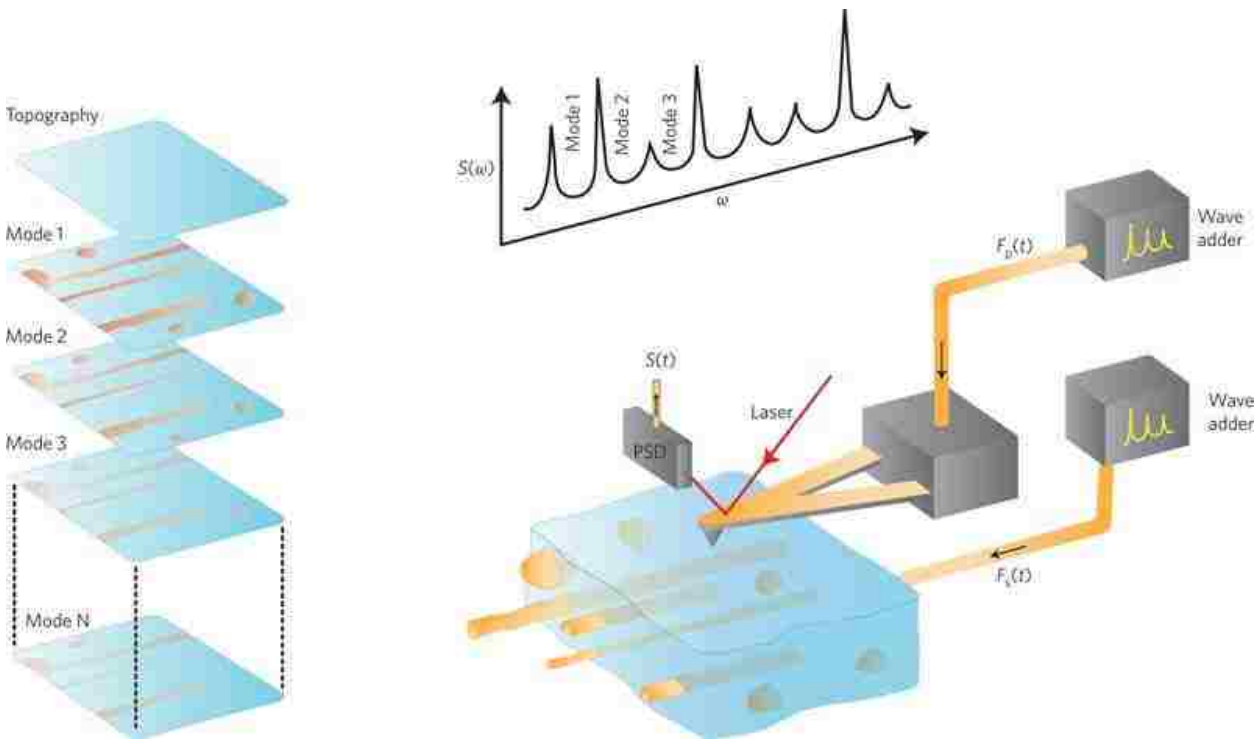

Figure 5–8 Schematic of one configuration of multi-frequency AFM, called mode-synthesizing AFM principles [233]. By applying multiple excitations to the tip-sample system, it is possible to synthesize new modes (difference and sum frequencies) operational for imaging and spectroscopy measurements. These are yet to be fully evaluated to determine the benefits and limitations of the approach.

In this section, we present the first development of MSAFM on the same platform as the nanoIR system and present the first comparison of the performance of MSFAM images to the images produced using two mechanical actuations or one mechanical actuation and one photothermally induced actuation.

5.3.2 Methods

We implemented two methods to evaluate MSAFM on the NanoIR2 (Anasys Instrument) platform.

The sample actuation was obtained by placing a piezoceramic component underneath the sample using a glue compatible for acoustic wave propagation. The piezo was connected to a function generator (Tektronix MDO 3012) to control the frequency and amplitude of the vibration.

The second actuation was made on the cantilever. In the case of the mechanical actuation, we used a U-shaped cantilever in which a AC signal can be applied using the internal function generator of the instrument. By placing a magnet close to the extremity of the cantilever, a Lorentz force was induced, as is described in the literature of Lorentz contact resonance modes[166]. The driving frequency of the cantilever was controlled by changing the frequency of the AC current through the sample. For these measurements, a carbon fiber-epoxy composite film was used to evaluate the system.

For the photothermal actuation, the infrared quantum cascade laser (QCL) of the system was used. The wavelength of the laser was kept constant at 1730 cm^{-1}, which corresponds to the maximal absorption of the PMMA region of the calibration sample used for the measurements. Following standard optimization protocol for nanoscale infrared spectroscopy measurements, we aligned the laser focal point at the location where the tip interacts with the sample surface. By

tuning the frequency of the QCL laser, the force resulting from the photothermal expansion of the sample was used as an actuation. For these measurements, a 200-400 nm thick film of epoxy in which polystyrene (PS) (1 μm diameter) and PMMA (3 μm diameter) beads are embedded.

In all cases, the dynamics of the cantilever was monitored using a read-out laser aligned at the back of the cantilever. The signal from the detector was accessed from the hardware of the controller and rerouted to an oscilloscope, the spectrum analyzer and a lockin amplifier. The signal was analyzed in time and frequency domains to study the contribution of the actuation of the system. For image formation, the data collection was limited by the option encoded in the NanoIR software.

5.3.3 Results and Discussion

5.3.3.1 All mechanical actuations

Using the LCR configuration of the AFM, the cantilever was engaged with the surface of the sample using the standard protocol. First, a topography image was collected to identify the regions of epoxy and carbon fiber samples (Figure 5-9 (left)). Next the cantilever actuation using the AC current was tuned to determine the contact resonance at ~405 kHz. The amplitude of the cantilever was recorded at each pixel of the image show in Figure 5-9 (center). In the MSAFM configuration, the probe was excited at 100 kHz and the sample was excited at 305 kHz with equal amplitude. With the tip and sample in contact, we observed the formation of a difference mode at 305 - 100 = 205 kHz and of a sum mode at 100 + 305 = 405 kHz.

The combination of frequency was selected to align the sum frequency mode with the contact resonance of the cantilever at 405 kHz. The image resulting from this configuration, monitored at frequency of 405 kHz, is shown in Figure 5-9 (right). The figure indicates that the selected mode

is more sensitive to the changes in topography than the composition of epoxy vs carbon fiber. A more comprehensive study will be continued in future studies.

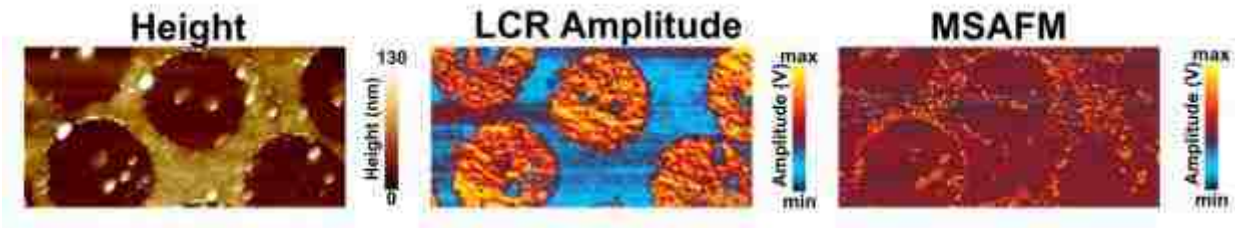

Figure 5–9 MSAFM with two mechanical actuations. (left) topography of the xx calibration sample, (center) traditional LCR amplitude map indicating a change in mechanical properties in the two regions, (right) MSAFM map obtained at f_p = 100 kHz, f_s = 305 kHz and monitoring the sum mode at 100 + 305 = 405 kHz. LCR and MSAFM images are amplitude images.

5.3.3.2 Mechanical and photothermal actuations

Using the nanoIR configuration of the AFM to apply a photothermal actuation on the tip, the cantilever was engaged with the PMMA surface using the standard protocol and nanoIR epoxy/PS/PMMA calibration sample (see Methods).

The frequency content of the signals was studied with the spectrum analyzer. The photothermal excitation was obtained by tuning the wavelength of the laser at 1730 cm^{-1}, the absorption band of PMMA, and by tuning the laser pulse frequency to the contact resonance of the cantilever. In this study, we fixed the laser pulse frequency at 178.76 kHz. Next the mechanical actuation of the sample was turned on and the frequency was swept from 200 kHz to 170 kHz.

We note that this configuration is close to intermodulation AFM, previously reported by Haviland's group[234]. This selection of frequencies was somewhat imposed by the limitations of the AFM software. Nevertheless the configuration is sufficient to carry out interesting proof of

concept measurement. In the waterfall display (Figure 5- 10) the peaks are represented by dots/rectangle in light blue to red color. For each line of the waterfall display (i.e., each frequency spectrum), one can observe that in addition to the driving frequency, at least one additional frequency was synthesized in the system, which was not present in absence of the additional actuations. Selected spectra presented in Figure 5-10 indicate that for f_p-f_s = +/-4 kHz and f_p-f_s = -2 kHz a higher number of small modes were synthesized in the system. These modes all correspond to the sum/difference mixing of | f_p-f_s | with the actuation modes. We also find that introducing a second actuation (that of the sample) in the system, engenders a decrease in the amplitude of the signal at the frequency corresponding to the photothermal excitation, which has not yet been explained.

The next step was to determine whether the new modes created were operational. We collected images using MSAFM excitations of the system. Due to the existing constraints of the instrument, we will only present in Figure 5-11 the images corresponding the image at f_p, and study the changes in the image when f_s, and thus the additional synthesized modes, change. First, a topography image was collected to identify the regions of epoxy and carbon fiber samples (Figure 5-11 (left)). Next, the photothermal actuation of the cantilever was tuned to the resonance frequency of the cantilever at 178.76 kHz. The resulting amplitude of the photothermal expansion is presented – labeled "NanoIR". This corresponds to a conventional chemical map when operating NanoIR2. After turning on the sample actuations we found that the amplitude of the mode at 178.76 kHz significantly decreased. The two MSAFM maps presented in Figure 5-11 were obtained using f_p (178.76 kHz) very close to f_s (179.8 kHz) and for using f_p (178.76 kHz) smaller than f_s (183.4 kHz). We note that in the first case, the image obtained was mainly sensitive to topography features, including sectioning marks on the films.

These marks were also present in the nanoIR image, although less noticeable, due to the high amplitude signals of the PMMA regions at 1730 cm^{-1}. Hence, the introduction of multifrequency in the system, with this set of frequencies, seemed to remove the sensitivity to the chemical information at the selected frequency. On the other hand, for $f_s > f_p$ the image recorded seemed to only be sensitive to the chemical composition, without the presence of topographical interferences. This observation is very important as it suggests that the nanoIR system could become selective to chemistry, or in other words, provide a deconvolution of the different properties measured. We note however that the signal-to-noise ratio obtained in the MSAFM channel was poorer than for nanoIR at this stage. The parameters should be optimized in the future.

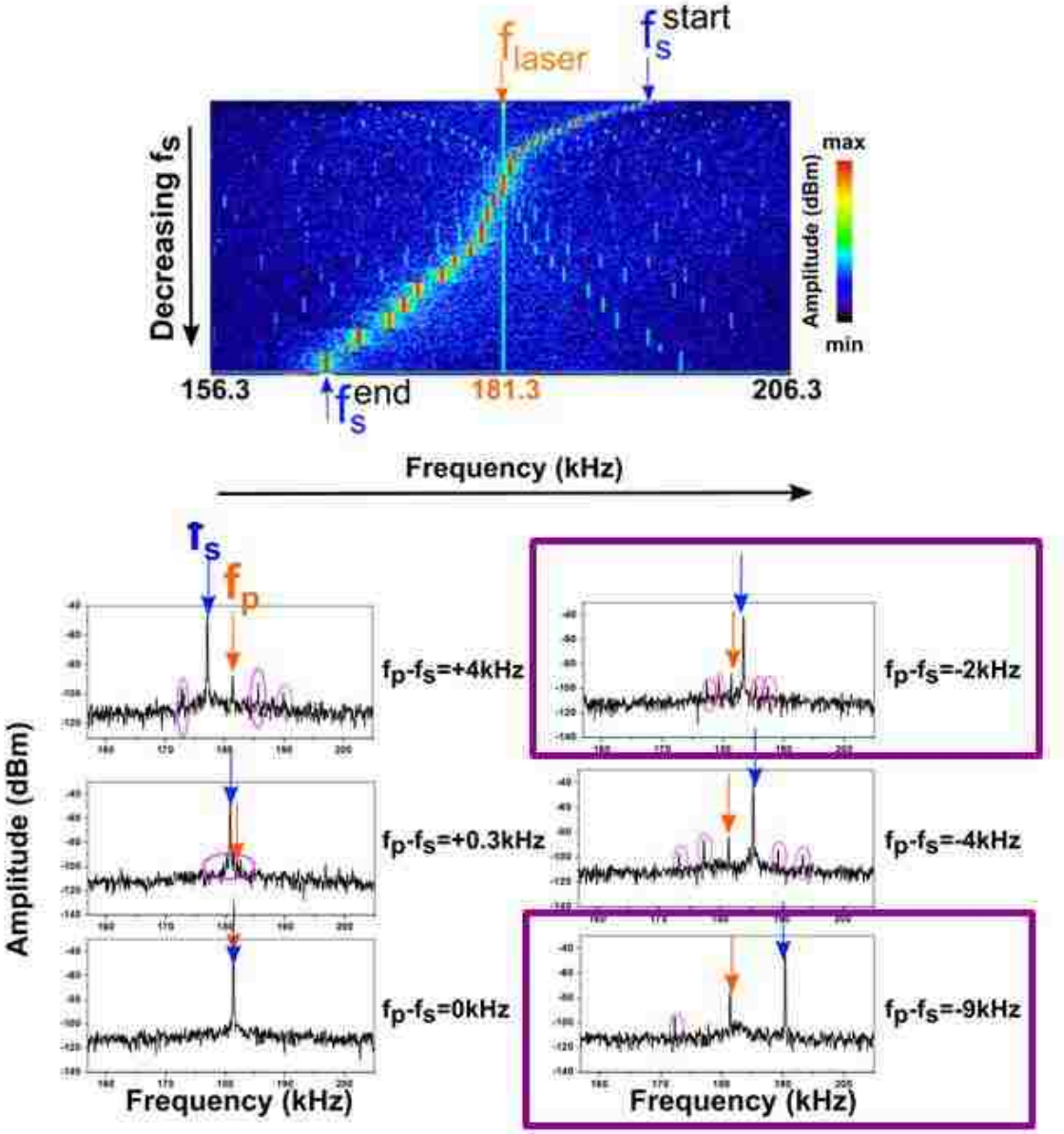

Figure 5–10 MSAFM with one mechanical actuation on the sample and one photothermal actuation on the tip using the infrared QCL laser. (Top) waterfall display of the frequency spectra generated over time as the driving frequency of the sample (f_s) is spanned from 200 kHz to 170 kHz. The laser excitation (f_p) was fixed at 178.76 kHz. (Bottom) frequency spectra of the tip-sample system for selected sample frequencies, f_p-f_s = +4 kHz, f_p-f_s = +0.3 kHz, f_p-f_s = 0 kHz, f_p-f_s = -2 kHz, f_p-f_s = -4 kHz, and f_p-f_s = -9 kHz.

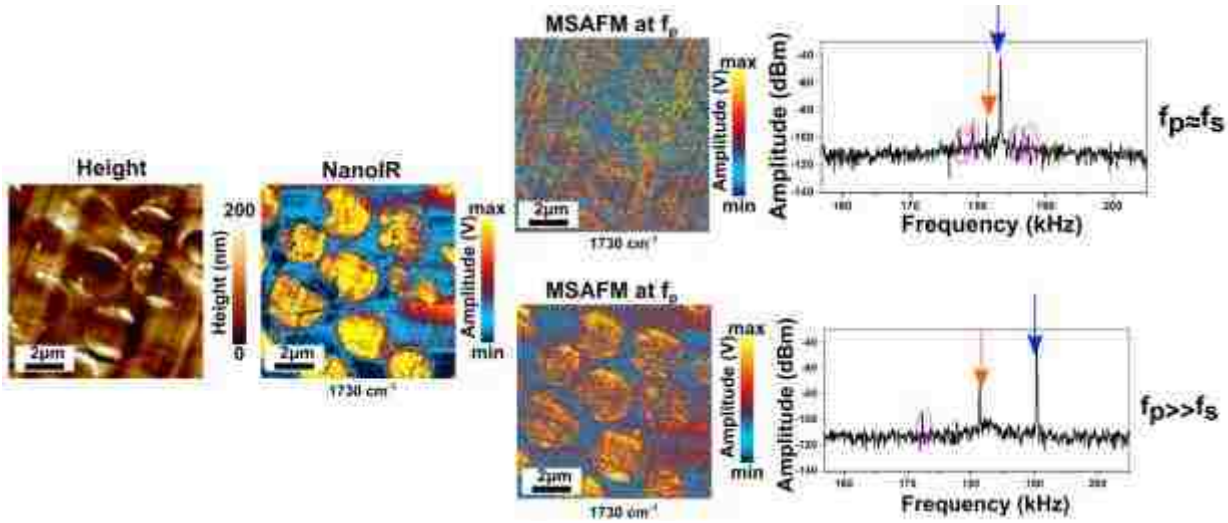

Figure 5–11MSAFM images at two different f_p resulting from one mechanical actuation on the sample and one photothermal actuation on the tip using the infrared QCL laser, and comparison to the conventional NanoIR map. (top) f_p is very close to f_s (bottom) f_p is larger than f_s.

5.3.4 Conclusions

These results, although preliminary, illustrate the rich content of the tip-sample dynamics and its potential to be exploited for functional imaging. However they also raise a number of new questions regarding the information contained in the MSAFM images at different frequencies. In the configuration of one mechanical actuation and on photothermal actuation, the images collected using different sets of frequencies for actuations suggest that multifrequency may provide the means to deconvolute the signals to isolate chemical information from background or interfering topographical signals. However, further calibration work should be implemented to deepen our understanding of the signals.

5.4 Summary and Future Perspectives

Beyond the behaviour of Au nanoislands or the proof of concept on calibration samples for MSAFM, the results are significant from the standpoint of metrology. In particular, there is a

growing interest in characterizing dynamic processes in systems such as nano-sized catalysts. A suitable platform would require high spatial and temporal resolution, high sensitivity, together with information related to chemical bonds. Our studies suggest that AFM could be an ideal platform for such studies, but indicate that contact mode and static measurements will not be sufficient. Multifrequency measurements may provide some flexibility in increasing the span of frequencies available to monitor different behaviours, however its implementation will require to better understanding the information contained in the different modes. Furthermore, although MSAFM is conceptually not restricted to any particular range of frequency, thus making is possible to access higher frequency ranges for time resolution, the limitation will be imposed by existing AFM components, such as the read-out detectors which currently cut-off at ~2 MHz in the best of cases. These developments will be explored in more details in the future.

6 CONCLUSION

6.1 Summary and Future Perspectives

In this dissertation, through different detailed case studies, we presented and discussed how advanced nanoscale spectroscopy and functional imaging can advance the current understanding of energy-related and catalytic materials. Revealing the fundamental properties of components inside complex material systems such as solar cells, supercapacitors and catalysts is of great importance to better understand the processing-structure-property-performance relationships of new emerging energy and catalytic materials is critical. The underlying nanoscale mechanisms that define the ultimate working of the device will likely boost the performance..

For energy storage materials, by using pc-AFM and MSAFM, we have identified that even the solvent used in fabricating active layers for the organic solar cells can greatly affect the morphology and structure network of the active layer with significant impact on the device performance of the solar cell device. For energy harvesting material, by using AFM and KPFM, we identified the coarsening of grain size of the material and the work function evolutions of electrode materials used in supercapacitors, which affected the electrical properties and the performance of the device over time.

For catalytic material studies, we first showed that the application of traditional imaging and spectroscopy methods such as SEM, time-dependent fluorescence spectroscopy, Raman spectroscopy and FTIR, served as useful tools, to some extent, to evaluate the effectiveness of different defect creation methods in order to identify the best catalyst fabrication protocols, to study the intrinsic properties and reactivity traits of created defects. Especially we highlighted how SEM combined with Raman spectroscopy helped us understanding flake size reduction and flake agglomeration. Time dependent fluorescence intensity spectra of *dh*-BN revealed

molecule-defect interaction kinetics. However the application of these techniques was limited by the diffraction limit and should be improved with environmental controlled studies

In addition, to overcome the diffraction limit and access information which was not accessible by traditional spectroscopic methods, a comprehensive study was conducted to understand the defect introduced changes in structural, chemical, catalytic, mechanical and electrical properties in heat treated defect laden *h*-BN flakes at the nanoscale. The application of NanoIR to monitor the localized defect formation and subsequent oxidation of exfoliated *h*-BN flakes suggests that functional nanoscale tools could provide powerful insights into the processes. We demonstrated that NanoIR enabled the acquisition of IR special with sub-100 nm spatial resolution from localized regions on the sample surface.

Our studies established some protocols to facilitate the studies of nanomaterials used in energy and catalysis. Our findings indicate that it will be important to set up controlled environments and improve time-resolution to reach a more complete understanding of the systems *in operando*.

APPENDIX A: BACKGROUND FOR AFM, FORCE CURVE MEASUREMENT AND PFM

Atomic Force Microscopy (AFM)

Since its invention in the 1980s, AFM has been regarded as the milestone instrument in the development of nanoscience and nanotechnology[235] as well as for material sciences. The basic working principle of AFM can be found in Chapter 2.

There are two basic topography imaging modes in AFM:

Contact mode: Contact mode is also known as static mode. The tip is in contact (short tip-sample distance) with sample surface. A repulsive interatomic force between the tip and the sample causes the cantilever to bend. The bending of the cantilever is used as the feedback parameter, which is kept constant during the scanning to maintain a constant force. The movement of the piezoelectric (PZT) scanner is recorded and the data is converted by the software to a 2D mapping for the sample surface topography.

Repulsive van der Waals force is usually dominant in contact mode. A capillary force is usually from the thin water film on the sample surface and is naturally attractive force[236].

Tapping mode: Tapping (AC) emerged to overcome the limitations of contact mode in soft material study (i.e., destructive). In tapping mode AFM, the cantilever is oscillated at or near its resonant frequency by a piezoelectric actuator with a free vibration amplitude A_0 (typically 20-100 nm)[236]. As the vibrating cantilever approaches and starts to tap slightly the sample surface, the amplitude damps due to the energy losses in the intermittent contact region. The oscillation amplitude of the cantilever is kept constant by the feedback loop, so that the interatomic force between the tip and the sample is constant. An error signal is generated to form a topography image and as a feedback parameter to keep the amplitude constant by adjusting the Z position of the PZT.

In addition to the amplitude variation, the phase shift between the free and damped oscillation is recorded. This is of interest because phase shifts are essentially caused by energy dissipation during the tip-sample interaction. This energy dissipation is usually related to the viscoelastic properties of the sample or the adhesion between the tip and the sample.

Force-Curve Measurement with an AFM

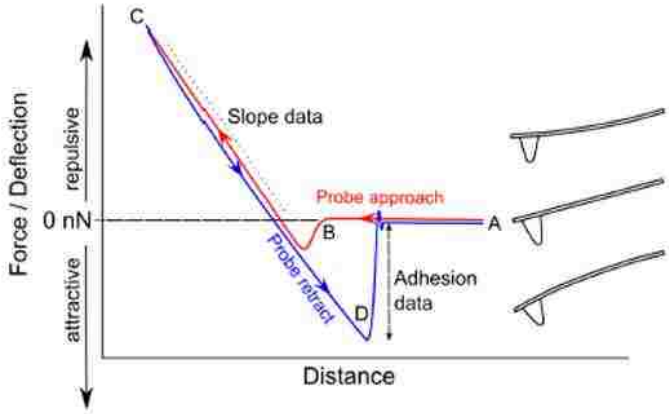

Figure A-1 Typical force vs. distance between the tip and sample surface[237]

AFM can also be used to acquire single point force curves by moving an AFM probe along Z direction. When the tip of the cantilever approaches the sample surface, a weak interatomic attractive force from the attraction between tip and the sample leads to bending of the cantilever 'downward'. As the separation decreases, the interatomic attractive force keeps increasing until the repulsive force from the electron clouds of the tip and the sample takes over and leads to the cantilever bending 'upward'. By plotting the binding force as a function of tip-sample separation, a force-curve is obtained, as shown in Figure A-1. Force-separation curves (separation corresponds to the movement of the Z piezo, not the actual tip-sample distance) should be converted to a force-distance curve to quantify the properties of the tip-sample interaction. The process has been well reported in the literature. The curves can be used to quantify the energy

dissipated in the tip-sample interaction, as well as the tip-sample adhesion force and when the tip indents the material, the Young's modulus (or stiffness) of the material.

Mechanical spectroscopy with Pulsed Force Mode Atomic Force Microscopy (termed as PFM-AFM or PFM)

It was early demonstrated that force curves and nano-indentation can be used to study the local mechanical properties of a material. Pulsed force AFM (PFM)[238] was developed to overcome the limitations identified in CM and AC modes. PFM constitutes a measurement of force curves at each pixel of an image.

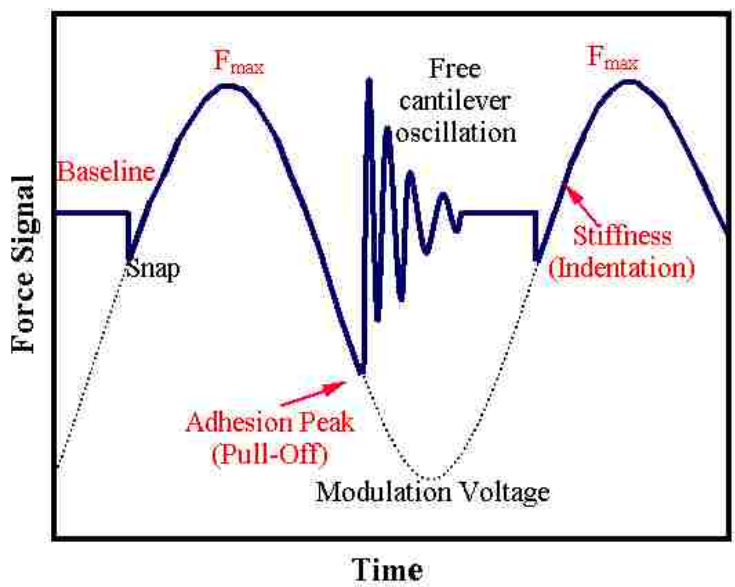

Figure A-2 Representative PFM curve (purple bold line) with sinusoidal modulation (dotted line), attributes related to stiffness, adhesion peak and F_{max} indicated on the curve

In PFM, a sinusoidal modulation is applied on the z-direction of the PZT at a frequency which is much lower than the resonant frequency of the cantilever (~1 kHz) with an amplitude 10-500 nm[228]. As shown in Figure A-2, the amplitude is controlled so that the range of displacement of the tip covers the region above the sample to a small indentation and back to out of contact for

each cycle. A force-time (that should be converted to distance) curve can be obtained for each cycle as shown in Figure A-2. By capturing a force curve at each point in the selected region of the sample, it is possible to reconstruct the adhesion, stiffness, and topography maps of the sample, as shown in Figure A-3.

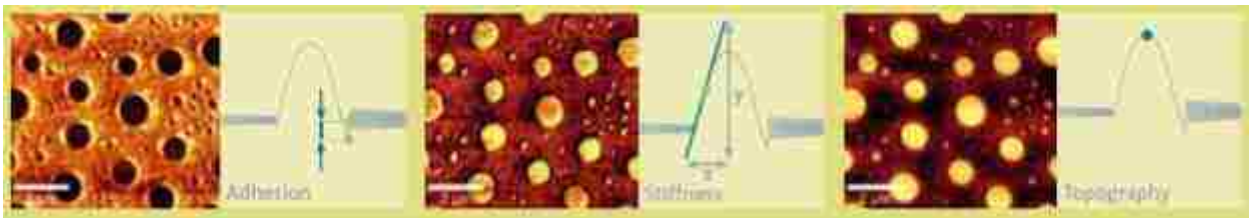

Figure A-3 Images reconstructed from PFM measurements on poly-methylmethacrylate/Polystyrene (PMMA/PS) blend: adhesion (left), stiffness (middle) and topography (right)

APPENDIX B: BACKGROUND FOR MODE SYNTHESIZING AFM (MSAFM)

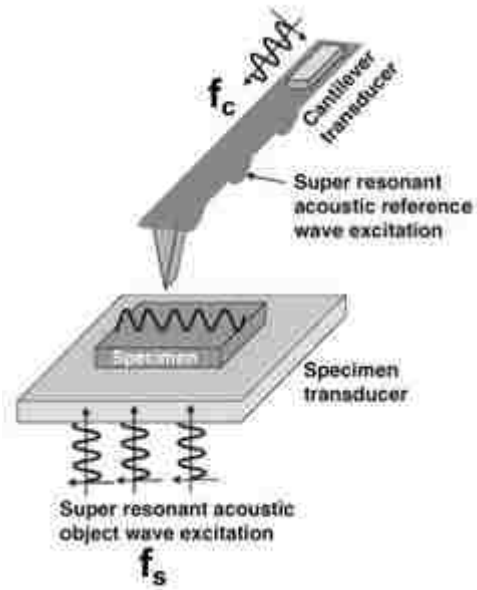

Figure B-1. Schematic illustration of the principle for mode-synthesizing AFM [239]

Multifrequency AFM is a method that extends the ability for conventional AFM to sense embedded structures/subsurface in biological or synthetic polymer materials nondestructively. The simplest model, as shown in Figure B-1, two excitations at frequencies which are much higher than the resonance frequency of the cantilever (f_0) are used to actuate the specimen (f_s) and the cantilever (f_c), respectively. Due to the existence of nonlinear nanomechaical coupling, the two excitation waves interfere with each other and generate new modes –the difference and sum modes-, which can be monitored by the cantilever[8,240]. One interpretation of this approach is that the sample wave propagates through the specimen from bottom to surface, any buried features can alter either phase or amplitude of the wave f_s, resulting on a change in the amplitude and phase of the difference and sum modes monitored. The images generated from the difference and sum signal have been shown to reveals subsurface features, which can be reconstructed together with 3D images [241].

In this work we consider this multifrequency approach to improve the sensitivity and time-resolution of our measurements, as described in Chapter 5.

APPENDIX C: COPYRIGHT PERSIMISSIONS FOR FIGURE 2-5, 2-6

Copyright Clearance Center RightsLink®

Home | Account Info | Help

ACS Publications
Most Trusted. Most Cited. Most Read.

Title: Probing Ternary Solvent Effect in High Voc Polymer Solar Cells Using Advanced AFM Techniques

Author: Chao Li, Yi Ding, Mikhael Soliman, et al

Publication: Applied Materials

Publisher: American Chemical Society

Date: Feb 1, 2016

Copyright © 2016, American Chemical Society

Logged in as:
Yi Ding
Account #: 3001055282
LOGOUT

PERMISSION/LICENSE IS GRANTED FOR YOUR ORDER AT NO CHARGE

This type of permission/license, instead of the standard Terms & Conditions, is sent to you because no fee is being charged for your order. Please note the following:

- Permission is granted for your request in both print and electronic formats, and translations.
- If figures and/or tables were requested, they may be adapted or used in part.
- Please print this page for your records and send a copy of it to your publisher/graduate school.
- Appropriate credit for the requested material should be given as follows: "Reprinted (adapted) with permission from (COMPLETE REFERENCE CITATION). Copyright (YEAR) American Chemical Society." Insert appropriate information in place of the capitalized words.
- One-time permission is granted only for the use specified in your request. No additional uses are granted (such as derivative works or other editions). For any other uses, please submit a new request.

If credit is given to another source for the material you requested, permission must be obtained from that source.

BACK | CLOSE WINDOW

Copyright © 2018 Copyright Clearance Center, Inc. All Rights Reserved. Privacy statement. Terms and Conditions.
Comments? We would like to hear from you. E-mail us at customercare@copyright.com

APPENDIX D: COPYRIGHT PERMISSION FOR FIGURE 3-1

Challenges in the Greener Production of Formates/Formic Acid, Methanol, and DME by Heterogeneously Catalyzed CO_2 Hydrogenation Processes

Andrea Álvarez[†], Atul Bansode[†], Atsushi Urakawa[*†], Anastasiya V. Bavykina[‡], Tim A. Wezendonk[‡], Michiel Makkee[‡], Jorge Gascon[*‡], and Freek Kapteijn[*‡]

[†] Institute of Chemical Research of Catalonia (ICIQ), The Barcelona Institute of Science and Technology, Avinguda dels Paisos Catalans 16, 43007 Tarragona, Spain

[‡] Catalysis Engineering, Chemical Engineering Department, Delft University of Technology, Van der Maasweg 9, 2629 HZ Delft, The Netherlands

Chem. Rev., **2017**, *117* (14), pp 9804–9838
DOI: 10.1021/acs.chemrev.6b00816
Publication Date (Web): June 28, 2017
Copyright © 2017 American Chemical Society
Get Full Text

*E-mail: f.kapteijn@tudelft.nl, *E-mail: aurakawa@iciq.es, *E-mail: j.gascon@tudelft.nl.

ACS AuthorChoice - This is an open access article published under a Creative Commons Non-Commercial No Derivative Works (CC-BY-NC-ND) Attribution License, which permits copying and redistribution of the article, and creation of adaptations, all for non-commercial purposes.

This article is part of the Carbon Capture and Separation special issue.

Cite this: *Chem. Rev.* 2017, 117, 14, 9804-9838

RIS Citation GO

APPENDIX E: COPYRIGHT PERMISSION FOR FIGURE 4-9

Copyright Clearance Center RightsLink®

Home | Create Account | Help

ACS Publications
Most Trusted. Most Cited. Most Read.

Title: AFM-IR: Technology and Applications in Nanoscale Infrared Spectroscopy and Chemical Imaging

Author: Alexandre Dazzi, Craig B. Prater

Publication: Chemical Reviews

Publisher: American Chemical Society

Date: Apr 1, 2017

Copyright © 2017, American Chemical Society

LOGIN

If you're a copyright.com user, you can login to RightsLink using your copyright.com credentials.

Already **a RightsLink user** or want to learn more?

PERMISSION/LICENSE IS GRANTED FOR YOUR ORDER AT NO CHARGE

This type of permission/license, instead of the standard Terms & Conditions, is sent to you because no fee is being charged for your order. Please note the following:

- Permission is granted for your request in both print and electronic formats, and translations.
- If figures and/or tables were requested, they may be adapted or used in part.
- Please print this page for your records and send a copy of it to your publisher/graduate school.
- Appropriate credit for the requested material should be given as follows: "Reprinted (adapted) with permission from (COMPLETE REFERENCE CITATION). Copyright (YEAR) American Chemical Society." Insert appropriate information in place of the capitalized words.
- One-time permission is granted only for the use specified in your request. No additional uses are granted (such as derivative works or other editions). For any other uses, please submit a new request.

If credit is given to another source for the material you requested, permission must be obtained from that source.

LIST OF REFERENCES

1 Binnig, G., Quate, C. F. & Gerber, C. Atomic Force Microscope. *Physical Review Letters* **56**, 930-933 (1986).

2 Gerber, C. & Lang, H. P. How the doors to the nanoworld were opened. *Nature nanotechnology* **1**, 3 (2006).

3 Tennyson, E. M., Howard, J. M. & Leite, M. S. Mesoscale functional imaging of materials for photovoltaics. *ACS Energy Letters* **2**, 1825-1834 (2017).

4 Green, M. A. & Bremner, S. P. Energy conversion approaches and materials for high-efficiency photovoltaics. *Nature materials* **16**, 23 (2017).

5 Ulvestad, A. *et al.* Topological defect dynamics in operando battery nanoparticles. *Science* **348**, 1344-1347 (2015).

6 Coffey, D. C., Reid, O. G., Rodovsky, D. B., Bartholomew, G. P. & Ginger, D. S. Mapping local photocurrents in polymer/fullerene solar cells with photoconductive atomic force microscopy. *Nano letters* **7**, 738-744 (2007).

7 Tennyson, E. M., Gong, C. & Leite, M. S. Imaging Energy Harvesting and Storage Systems at the Nanoscale. *ACS Energy Letters* **2**, 2761-2777 (2017).

8 Tetard, L., Passian, A. & Thundat, T. New modes for subsurface atomic force microscopy through nanomechanical coupling. *Nature Nanotechnology* **5**, 105-109 (2010).

9 Soliman, M., Ding, Y. & Tetard, L. Nanoscale subsurface imaging. *Journal of Physics: Condensed Matter* **29**, 173001 (2017).

10 Dazzi, A. & Prater, C. B. AFM-IR: technology and applications in nanoscale infrared spectroscopy and chemical imaging. *Chemical reviews* **117**, 5146-5173 (2016).

11 Lewis, N. S. & Crabtree, G. (US Department of Energy, Office of Basic Energy Science, 2005).

12 Krebs, F. C. Fabrication and processing of polymer solar cells: a review of printing and coating techniques. *Solar energy materials and solar cells* **93**, 394-412 (2009).

13 Niu, G., Guo, X. & Wang, L. Review of recent progress in chemical stability of perovskite solar cells. *Journal of Materials Chemistry A* **3**, 8970-8980 (2015).

14 Kim, B. J. *et al.* Highly efficient and bending durable perovskite solar cells: toward a wearable power source. *Energy & Environmental Science* **8**, 916-921 (2015).

15 Laquai, F., Andrienko, D., Deibel, C. & Neher, D. in *Elementary Processes in Organic Photovoltaics* 267-291 (Springer, 2017).

16 Yang, Y., Mielczarek, K., Aryal, M., Zakhidov, A. & Hu, W. Effects of nanostructure geometry on nanoimprinted polymer photovoltaics. *Nanoscale* **6**, 7576-7584 (2014).

17 Dutta, P. *et al.* Connecting physical properties of spin-casting solvents with morphology, nanoscale charge transport, and device performance of poly(3-hexylthiophene):phenyl-C61-butyric acid methyl ester bulk heterojunction solar cells. *Journal of Photonics for Energy* **1**, 011124-011124-011117 (2011).

18 Yu, G., Gao, J., Hummelen, J. C., Wudl, F. & Heeger, A. J. Polymer photovoltaic cells: enhanced efficiencies via a network of internal donor-acceptor heterojunctions. *Science* **270**, 1789-1791 (1995).

19 Siddiki, M. K., Li, J., Galipeau, D. & Qiao, Q. A review of polymer multijunction solar cells. *Energy & Environmental Science* **3**, 867-883 (2010).

20 Dante, M., Peet, J. & Nguyen, T.-Q. Nanoscale charge transport and internal structure of bulk heterojunction conjugated polymer/fullerene solar cells by scanning probe microscopy. *The Journal of Physical Chemistry C* **112**, 7241-7249 (2008).

21 Ma, W. *et al.* Quantification of Nano- and Mesoscale Phase Separation and Relation to Donor and Acceptor Quantum Efficiency, Jsc, and FF in Polymer:Fullerene Solar Cells. *Advanced Materials* **26**, 4234-4241 (2014).

22 Markov, D. E., Amsterdam, E., Blom, P. W. M., Sieval, A. B. & Hummelen, J. C. Accurate Measurement of the Exciton Diffusion Length in a Conjugated Polymer Using a Heterostructure with a Side-Chain Cross-Linked Fullerene Layer. *The Journal of Physical Chemistry A* **109**, 5266-5274 (2005).

23 Terao, Y., Sasabe, H. & Adachi, C. Correlation of hole mobility, exciton diffusion length, and solar cell characteristics in phthalocyanine/fullerene organic solar cells. *Applied Physics Letters* **90**, 103515 (2007).

24 Stranks, S. D. *et al.* Electron-Hole Diffusion Lengths Exceeding 1 Micrometer in an Organometal Trihalide Perovskite Absorber. *Science* **342**, 341-344 (2013).

25 Xing, G. *et al.* Long-Range Balanced Electron- and Hole-Transport Lengths in Organic-Inorganic CH3NH3PbI3. *Science* **342**, 344-347 (2013).

26 Jiang, C.-S. *et al.* Carrier separation and transport in perovskite solar cells studied by nanometre-scale profiling of electrical potential. *Nature Communications* **6**, 8397 (2015).

27 Kutes, Y. *et al.* Mapping the Photoresponse of CH3NH3PbI3 Hybrid Perovskite Thin Films at the Nanoscale. *Nano Letters* **16**, 3434-3441 (2016).

28 Leblebici, S. Y. *et al.* Facet-dependent photovoltaic efficiency variations in single grains of hybrid halide perovskite. *Nature Energy* **1**, 16093 (2016).

29 Giridharagopal, R., Cox, P. A. & Ginger, D. S. Functional Scanning Probe Imaging of Nanostructured Solar Energy Materials. *Accounts of Chemical Research* **49**, 1769-1776 (2016).

30 Li, C. *et al.* Probing ternary solvent effect in high Voc polymer solar cells using advanced AFM techniques. *ACS Applied Materials and Interfaces* **8**, Probing ternary solvent effect in high Voc polymer solar cells using advanced AFM techniques (2016).

31 Cox, P. A., Flagg, L. Q., Giridharagopal, R. & Ginger, D. S. Cantilever Ringdown Dissipation Imaging for the Study of Loss Processes in Polymer/Fullerene Solar Cells. *The Journal of Physical Chemistry C* **120**, 12369-12376 (2016).

32 Grosso, G. *et al.* Tunable and high-purity room temperature single-photon emission from atomic defects in hexagonal boron nitride. *Nature communications* **8**, 705 (2017).

33 Bergmann, V. W. *et al.* Real-space observation of unbalanced charge distribution inside a perovskite-sensitized solar cell. *Nature Communications* **5**, 5001 (2014).

34 Yuan, Y. *et al.* Anomalous photovoltaic effect in organic-inorganic hybrid perovskite solar cells. *Science Advances* **3** (2017).

35 Yuan, Y. *et al.* Photovoltaic Switching Mechanism in Lateral Structure Hybrid Perovskite Solar Cells. *Advanced Energy Materials* **5**, 1500615 (2015).

36 Chae, J., Dong, Q., Huang, J. & Centrone, A. Chloride Incorporation Process in CH3NH3PbI3–xClx Perovskites via Nanoscale Bandgap Maps. *Nano Letters* **15**, 8114-8121 (2015).

37 Takihara, M., Takahashi, T. & Ujihara, T. Minority carrier lifetime in polycrystalline silicon solar cells studied by photoassisted Kelvin probe force microscopy. *Applied Physics Letters* **93**, 021902 (2008).

38 Shao, G., Glaz, M. S., Ma, F., Ju, H. & Ginger, D. S. Intensity-Modulated Scanning Kelvin Probe Microscopy for Probing Recombination in Organic Photovoltaics. *ACS Nano* **8**, 10799-10807 (2014).

39 Coffey, D. C. & Ginger, D. S. Time-resolved electrostatic force microscopy of polymer solar cells. *Nat Mater* **5**, 735-740 (2006).

40 Li, Y. Molecular design of photovoltaic materials for polymer solar cells: toward suitable electronic energy levels and broad absorption. *Accounts of Chemical Research* **45**, 723-733 (2012).

41 Dutta, P. *et al.* Connecting physical properties of spin-casting solvents with morphology, nanoscale charge transport, and device performance of poly (3-hexylthiophene): phenyl-C 61-butyric acid methyl ester bulk heterojunction solar cells. *Journal of Photonics for Energy* **1**, 011124 (2011).

42 Markov, D. E., Amsterdam, E., Blom, P. W., Sieval, A. B. & Hummelen, J. C. Accurate measurement of the exciton diffusion length in a conjugated polymer using a heterostructure with a side-chain cross-linked fullerene layer. *The Journal of Physical Chemistry A* **109**, 5266-5274 (2005).

43 Green, M. A. *et al.* Solar cell efficiency tables (version 52). *Progress in Photovoltaics* **26** (2018).

44 Cowan, S. R., Roy, A. & Heeger, A. J. Recombination in polymer-fullerene bulk heterojunction solar cells. *Physical Review B* **82**, 245207 (2010).

45 Tetard, L. *et al.* Nanometrology of delignified Populus using mode synthesizing atomic force microscopy. *Nanotechnology* **22**, 465702 (2011).

46 Vitry, P. *et al.* Advances in quantitative nanoscale subsurface imaging by mode-synthesizing atomic force microscopy. *Applied Physics Letters* **105**, 053110 (2014).

47 McLean, R. S. & Sauer, B. B. Tapping-mode AFM studies using phase detection for resolution of nanophases in segmented polyurethanes and other block copolymers. *Macromolecules* **30**, 8314-8317 (1997).

48 Unger, E. *et al.* Hysteresis and transient behavior in current–voltage measurements of hybrid-perovskite absorber solar cells. *Energy & Environmental Science* **7**, 3690-3698 (2014).

49 Cojocaru, L. *et al.* Origin of the Hysteresis in I–V Curves for Planar Structure Perovskite Solar Cells Rationalized with a Surface Boundary-induced Capacitance Model. *Chemistry Letters* **44**, 1750-1752 (2015).

50 González, A., Goikolea, E., Barrena, J. A. & Mysyk, R. Review on supercapacitors: technologies and materials. *Renewable and Sustainable Energy Reviews* **58**, 1189-1206 (2016).

51 Simon, P. & Gogotsi, Y. in *Nanoscience And Technology: A Collection of Reviews from Nature Journals* 320-329 (World Scientific, 2010).

52 Wang, F. *et al.* Electrode materials for aqueous asymmetric supercapacitors. *Rsc Advances* **3**, 13059-13084 (2013).

53 Zhang, J. & Zhao, X. On the configuration of supercapacitors for maximizing electrochemical performance. *ChemSusChem* **5**, 818-841 (2012).

54 Miller, J. R. & Simon, P. Electrochemical capacitors for energy management. *Science Magazine* **321**, 651-652 (2008).

55 Yuan, C. *et al.* Hierarchically structured carbon-based composites: design, synthesis and their application in electrochemical capacitors. *Nanoscale* **3**, 529-545 (2011).

56 Huang, Y., Liang, J. & Chen, Y. An overview of the applications of graphene‐based materials in supercapacitors. *Small* **8**, 1805-1834 (2012).

57 Yang, S. *et al.* Electrodeposition of porous graphene networks on nickel foams as supercapacitor electrodes with high capacitance and remarkable cyclic stability. *Nanoscale research letters* **9**, 672 (2014).

58 Kumar, K. S., Choudhary, N., Jung, Y. & Thomas, J. Recent advances in two-dimensional nanomaterials for supercapacitor electrode applications. *ACS Energy Letters* **3**, 482-495 (2018).

59 Choudhary, N. *et al.* Asymmetric supercapacitor electrodes and devices. *Advanced Materials* **29**, 1605336 (2017).

60 Slater, M. D., Kim, D., Lee, E. & Johnson, C. S. Sodium‐ion batteries. *Advanced Functional Materials* **23**, 947-958 (2013).

61 Choudhary, N. *et al.* High-performance one-body core/shell nanowire supercapacitor enabled by conformal growth of capacitive 2D WS2 layers. *ACS nano* **10**, 10726-10735 (2016).

62 Zhang, Y. *et al.* Sensing the charge state of single gold nanoparticles via work function measurements. *Nano letters* **15**, 51-55 (2014).

63 *Kelvin Probe Force Microscopy* <http://www.spm.iis.u-tokyo.ac.jp/takihara/Kelvin%20probe%20force%20microscopy_e.html>

64 Huang, J., Jia, X., Yasuda, H. & Mori, H. Stacking disordering in hexagonal BN induced by shearing under ball milling. *Philosophical magazine letters* **79**, 217-224 (1999).

65 Hsu, A., Moffat, A. S., Weinfurter, A. J. & Schwartz, J. D. Towards a new climate diplomacy. *Nature Climate Change* **5**, 501 (2015).

66 Álvarez, A. *et al.* Challenges in the greener production of formates/formic acid, methanol, and DME by heterogeneously catalyzed CO2 hydrogenation processes. *Chemical reviews* **117**, 9804-9838 (2017).

67 Li, Y. & Somorjai, G. A. Nanoscale advances in catalysis and energy applications. *Nano letters* **10**, 2289-2295 (2010).

68 Somorjai, G. A. & Park, J. Y. Molecular factors of catalytic selectivity. *Angewandte Chemie International Edition* **47**, 9212-9228 (2008).

69 Solozhenko, V., Lazarenko, A., Petitet, J.-P. & Kanaev, A. Bandgap energy of graphite-like hexagonal boron nitride. *Journal of Physics and Chemistry of Solids* **62**, 1331-1334 (2001).

70 Tian, J. *et al.* Hexagonal boron nitride catalyst in a fixed-bed reactor for exothermic propane oxidation dehydrogenation. *Chemical Engineering Science* **186**, 142-151 (2018).

71 Nash, D. J. *et al.* Heterogeneous Metal-Free Hydrogenation over Defect-Laden Hexagonal Boron Nitride. *ACS Omega* **1**, 1343-1354 (2016).

72 Li, L. *et al.* Ambient carbon dioxide capture using boron-rich porous boron nitride: a theoretical study. *ACS Applied Materials & Interfaces* **9**, 15399-15407 (2017).

73 Grant, J. T. *et al.* Selective oxidative dehydrogenation of propane to propene using boron nitride catalysts. *Science* **354**, 1570-1573 (2016).

74 Venegas, J. M. *et al.* Selective Oxidation of n‐Butane and Isobutane Catalyzed by Boron Nitride. *ChemCatChem* **9**, 2118-2127 (2017).

75 Grant, J. T. *et al.* Boron and Boron‐Containing Catalysts for the Oxidative Dehydrogenation of Propane. *ChemCatChem* **9**, 3623-3626 (2017).

76 Fomichev, V., Rudnev, A. & Nemnonov, S. X-Ray emission bands of transition metals of the first long period *Soviet Physics Solid State* **13**, 1031-1033 (1971).

77 Carpenter, L. & Kirby, P. The electrical resistivity of boron nitride over the temperature range 700 degrees C to 1400 degrees C. *Journal of Physics D: Applied Physics* **15**, 1143 (1982).

78 Akinwande, D., Petrone, N. & Hone, J. Two-dimensional flexible nanoelectronics. *Nature communications* **5**, 5678 (2014).

79 Watanabe, K., Taniguchi, T., Niiyama, T., Miya, K. & Taniguchi, M. Far-ultraviolet plane-emission handheld device based on hexagonal boron nitride. *Nature Photonics* **3**, 591 (2009).

80 Zhong, L. *et al.* Defect engineering of two-dimensional transition metal dichalcogenides. *2D Materials* **3**, 022002 (2016).

81 Peng, Q. *et al.* Defect Engineering of 2D monoatomic-layer materials *Modern Physics Letters B* **27**, 1330017 (2013).

82 Sajid, A., Reimers, J. R. & Ford, M. J. Defect states in hexagonal boron nitride: Assignments of observed properties and prediction of properties relevant to quantum computation. *Physical Review B* **97**, 064101 (2018).

83 McDougall, N. L., Partridge, J. G., Nicholls, R. J., Russo, S. P. & McCulloch, D. G. Influence of point defects on the near edge structure of hexagonal boron nitride. *Physical Review B* **96**, 144106 (2017).

84 Henck, H. *et al.* Stacking fault and defects in single domain multilayered hexagonal boron nitride. *Applied Physics Letters* **110**, 023101 (2017).

85 Berzina, B. *et al.* Defect-induced blue luminescence of hexagonal boron nitride. *Diamond and Related Materials* **68**, 131-137 (2016).

86 Kroes, J., Fasolino, A. & Katsnelson, M. Energetics, barriers and vibrational spectra of partially and fully hydrogenated hexagonal boron nitride. *Physical Chemistry Chemical Physics* **18**, 19359-19367 (2016).

87 Graf, D. *et al.* Spatially resolved Raman spectroscopy of single-and few-layer graphene. *Nano letters* **7**, 238-242 (2007).

88 Mignuzzi, S. *et al.* Effect of disorder on Raman scattering of single-layer MoS2. *Physical Review B* **91**, 195411 (2015).

89 Kang, N., Paudel, H. P., Leuenberger, M. N., Tetard, L. & Khondaker, S. I. Photoluminescence quenching in single-layer MoS2 via oxygen plasma treatment. *The Journal of Physical Chemistry C* **118**, 21258-21263 (2014).

90 Li, L. H. & Chen, Y. Atomically thin boron nitride: unique properties and applications. *Advanced Functional Materials* **26**, 2594-2608 (2016).

91 Kobayashi, Y., Fukui, K.-i., Enoki, T., Kusakabe, K. & Kaburagi, Y. Observation of zigzag and armchair edges of graphite using scanning tunneling microscopy and spectroscopy. *Physical Review B* **71**, 193406 (2005).

92 Hashimoto, A., Suenaga, K., Gloter, A., Urita, K. & Iijima, S. Direct evidence for atomic defects in graphene layers. *Nature* **430**, 870-873 (2004).

93 Immohr, S., Felderhoff, M., Weidenthaler, C. & Schüth, F. An orders of magnitude increase in the rate of the solid‐catalyzed CO oxidation by in situ ball milling. *Angewandte Chemie International Edition* **52**, 12688-12691 (2013).

94 Rodriguez, B., Bruckmann, A., Rantanen, T. & Bolm, C. Solvent-free carbon-carbon bond formations in ball mills. *Advanced Synthesis & Catalysis* **349**, 2213-2233 (2007).

95 Eckert, R., Felderhoff, M. & Schüth, F. Preferential carbon monoxide oxidation over copper‐based catalysts under in situ ball milling. *Angewandte Chemie* **129**, 2485-2488 (2017).

96 Molchanov, V., Byanov, R. & Goidin, V. Use of mechanochemical methods in preparation of supported catalysts. *Kinetics and catalysis* **39**, 434-439 (1998).

97 Zazhigalov, V., Haber, J., Stoch, J., Bogutskaya, L. & Bacherikova, I. Mechanochemistry as activation method of the VPO catalysts for n-butane partial oxidation. *Applied Catalysis A: General* **135**, 155-161 (1996).

98 Ghosh, J., Mazumdar, S., Das, M., Ghatak, S. & Basu, A. Microstructural characterization of amorphous and nanocrystalline boron nitride prepared by high-energy ball milling. *Materials Research Bulletin* **43**, 1023-1031 (2008).

99 Tongay, S. *et al.* Defects activated photoluminescence in two-dimensional semiconductors: interplay between bound, charged, and free excitons. *Scientific reports* **3**, 2657 (2013).

100 Nan, H. *et al.* Strong photoluminescence enhancement of MoS2 through defect engineering and oxygen bonding. *ACS nano* **8**, 5738-5745 (2014).

101 Wei, X. *et al.* Mo-O bond doping and related-defect assisted enhancement of photoluminescence in monolayer MoS2. *Aip Advances* **4**, 123004 (2014).

102 Torii, S., Jimura, K., Hayashi, S., Kikuchi, R. & Takagaki, A. Utilization of hexagonal boron nitride as a solid acid–base bifunctional catalyst. *Journal of Catalysis* **355**, 176-184 (2017).

103 Fakrach, B. *et al.* Infrared spectrum of single-walled boron nitride nanotubes. *Physical Review B* **85**, 115437 (2012).

104 Aradi, E. *et al.* Ion beam modification of the structure and properties of hexagonal boron nitride: An infrared and X-ray diffraction study. *Nuclear Instruments and Methods in Physics Research Section B: Beam Interactions with Materials and Atoms* **331**, 140-143 (2014).

105 Nithya, J. S. M. & Pandurangan, A. Efficient mixed metal oxide routed synthesis of boron nitride nanotubes. *RSC Advances* **4**, 26697-26705 (2014).

106 Baraton, M. I., Merle, T., Quintard, P. & Lorenzelli, V. Surface activity of a boron nitride powder: a vibrational study. *Langmuir* **9**, 1486-1491 (1993).

107 Li, J. *et al.* Activated boron nitride as an effective adsorbent for metal ions and organic pollutants. *Scientific reports* **3**, 3208 (2013).

108 Tang, C., Bando, Y., Huang, Y., Zhi, C. & Golberg, D. Synthetic routes and formation mechanisms of spherical boron nitride nanoparticles. *Advanced Functional Materials* **18**, 3653-3661 (2008).

109 Li, L. H., Cervenka, J., Watanabe, K., Taniguchi, T. & Chen, Y. Strong Oxidation Resistance of Atomically Thin Boron Nitride Nanosheets. *ACS Nano* **8**, 1457-1462 (2014).

110 Liao, Y. *et al.* Oxidative etching of hexagonal boron nitride toward nanosheets with defined edges and holes. *Scientific reports* **5**, 14510 (2015).

111 Yang, Q. *et al.* Crystalline boron oxide nanowires on silicon substrate. *Physica E: Low-dimensional Systems and Nanostructures* **27**, 319-324 (2005).

112 Ding, Y. *et al.* Defect engineering in Boron Nitride for catalysis. *MRS Communications*, 1-8 (2018).

113 *MSE Supplies* <[https://www.msesupplies.com/>

114 Komsa, H.-P. *et al.* Two-dimensional transition metal dichalcogenides under electron irradiation: defect production and doping. *Physical review letters* **109**, 035503 (2012).

115 Ugeda, M. *et al.* Point defects on graphene on metals. *Physical review letters* **107**, 116803 (2011).

116 Lahiri, J., Lin, Y., Bozkurt, P., Oleynik, I. I. & Batzill, M. An extended defect in graphene as a metallic wire. *Nature nanotechnology* **5**, 326 (2010).

117 Museur, L., Anglos, D., Petitet, J.-P., Michel, J.-P. & Kanaev, A. V. Photoluminescence of hexagonal boron nitride: effect of surface oxidation under UV-laser irradiation. *Journal of luminescence* **127**, 595-600 (2007).

118 Museur, L., Feldbach, E. & Kanaev, A. Defect-related photoluminescence of hexagonal boron nitride. *Physical Review B* **78**, 155204 (2008).

119 Kanaev, A. V. *et al.* Femtosecond and ultraviolet laser irradiation of graphitelike hexagonal boron nitride. *Journal of Applied Physics* **96**, 4483-4489 (2004).

120 Museur, L. & Kanaev, A. Near band-gap photoluminescence properties of hexagonal boron nitride. *Journal of Applied Physics* **103**, 103520 (2008).

121 Katzir, A., Suss, J., Zunger, A. & Halperin, A. Point defects in hexagonal boron nitride. I. EPR, thermoluminescence, and thermally-stimulated-current measurements. *Physical Review B* **11**, 2370 (1975).

122 Taniguchi, T. & Watanabe, K. Synthesis of high-purity boron nitride single crystals under high pressure by using Ba–BN solvent. *Journal of crystal growth* **303**, 525-529 (2007).

123 Baraton, M., Merle, T., Quintard, P. & Lorenzelli, V. Surface activity of a boron nitride powder: a vibrational study. *Langmuir* **9**, 1486-1491 (1993).

124 Sudeep, P. M. *et al.* Functionalized boron nitride porous solids. *RSC Advances* **5**, 93964-93968 (2015).

125 Deng, D. H. *et al.* Catalysis with two-dimensional materials and their heterostructures. *Nature Nanotechnology* **11**, 218-230 (2016).

126 Novoselov, K. S. *et al.* Two-dimensional gas of massless Dirac fermions in graphene. *Nature* **438**, 197 (2005).

127 Castro Neto, A. H., Guinea, F., Peres, N. M. R., Novoselov, K. S. & Geim, A. K. The electronic properties of graphene. *Reviews of Modern Physics* **81**, 109-162 (2009).

128 Mak, K. F., Lee, C., Hone, J., Shan, J. & Heinz, T. F. Atomically Thin ${\mathrm{MoS}}_{2}$: A New Direct-Gap Semiconductor. *Physical Review Letters* **105**, 136805 (2010).

129 Wang, Q. H., Kalantar-Zadeh, K., Kis, A., Coleman, J. N. & Strano, M. S. Electronics and optoelectronics of two-dimensional transition metal dichalcogenides. *Nature Nanotechnology* **7**, 699 (2012).

130 Zhong, L. *et al.* 2D materials advances: from large scale synthesis and controlled heterostructures to improved characterization techniques, defects and applications. *2D Materials* **3**, 042001 (2016).

131 Zou, X. & Yakobson, B. I. An Open Canvas—2D Materials with Defects, Disorder, and Functionality. *Accounts of Chemical Research* **48**, 73-80 (2015).

132 Du, X., Skachko, I., Barker, A. & Andrei, E. Y. Approaching ballistic transport in suspended graphene. *Nature Nanotechnology* **3**, 491 (2008).

133 Kakavelakis, G., Kymakis, E. & Petridis, K. 2D Materials Beyond Graphene for Metal Halide Perovskite Solar Cells. *Advanced Materials Interfaces* **0**, 1800339 (2018)

134 Huang, Y.-J., Chen, H.-C., Lin, H.-K. & Wei, K.-H. Doping ZnO Electron Transport Layers with MoS2 Nanosheets Enhances the Efficiency of Polymer Solar Cells. *ACS Applied Materials & Interfaces* **10**, 20196-20204 (2018).

135 Yu, Z., Tetard, L., Zhai, L. & Thomas, J. Supercapacitor electrode materials: nanostructures from 0 to 3 dimensions. *Energy & Environmental Science* **8**, 702-730 (2015).

136 Li, X. & Zhi, L. Graphene hybridization for energy storage applications. *Chemical Society Reviews* **47**, 3189-3216 (2018).

137 Yi, F. *et al.* Wearable energy sources based on 2D materials. *Chemical Society Reviews* **47**, 3152-3188 (2018).

138 Bell, A. T. The Impact of Nanoscience on Heterogeneous Catalysis. *Science* **299**, 1688 (2003).

139 Jaramillo, T. F. *et al.* Identification of active edge sites for electrochemical H-2 evolution from MoS2 nanocatalysts. *Science* **317**, 100-102 (2007).

140 Wang, H., Yuan, H., Hong, S. S., Li, Y. & Cui, Y. Physical and chemical tuning of two-dimensional transition metal dichalcogenides. *Chemical Society Reviews* **44**, 2664-2680 (2015).

141 Antolini, E. Graphene as a new carbon support for low-temperature fuel cell catalysts. *Applied Catalysis B-Environmental* **123**, 52-68 (2012).

142 Hur, S. H. & Park, J.-N. Graphene and its application in fuel cell catalysis: a review. *Asia-Pacific Journal of Chemical Engineering* **8**, 218-233 (2013).

143 An, X. & Yu, J. C. Graphene-based photocatalytic composites. *Rsc Advances* **1**, 1426-1434 (2011).

144 Machado, B. F. & Serp, P. Graphene-based materials for catalysis. *Catalysis Science & Technology* **2**, 54-75 (2012).

145 Deng, D. *et al.* Size effect of graphene on electrocatalytic activation of oxygen. *Chemical Communications* **47**, 10016-10018 (2011).

146 Wang, H., Sun, K., Tao, F., Stacchiola, D. J. & Hu, Y. H. 3D Honeycomb-Like Structured Graphene and Its High Efficiency as a Counter-Electrode Catalyst for Dye-Sensitized Solar Cells. *Angewandte Chemie-International Edition* **52**, 9210-9214 (2013).

147 Deng, J. *et al.* Triggering the electrocatalytic hydrogen evolution activity of the inert two-dimensional MoS2 surface via single-atom metal doping. *Energy & Environmental Science* **8**, 1594-1601 (2015).

148 Voiry, D. *et al.* Enhanced catalytic activity in strained chemically exfoliated WS2 nanosheets for hydrogen evolution. *Nature Materials* **12**, 850-855 (2013).

149 Chen, X., Zhang, J., Fu, X., Antonietti, M. & Wang, X. Fe-g-C3N4-Catalyzed Oxidation of Benzene to Phenol Using Hydrogen Peroxide and Visible Light. *Journal of the American Chemical Society* **131**, 11658, (2009).

150 Islam, M. R. *et al.* Tuning the electrical property via defect engineering of single layer MoS2 by oxygen plasma. *Nanoscale* **6**, 10033-10039 (2014).

151 Nakada, K., Fujita, M., Dresselhaus, G. & Dresselhaus, M. S. Edge state in graphene ribbons: Nanometer size effect and edge shape dependence. *Physical Review B* **54**, 17954-17961 (1996).

152 Girit, C. O. *et al.* Graphene at the Edge: Stability and Dynamics. *Science* **323**, 1705-1708 (2009).

153 Banhart, F., Kotakoski, J. & Krasheninnikov, A. V. Structural Defects in Graphene. *Acs Nano* **5**, 26-41 (2011).

154 Li, L., Reich, S. & Robertson, J. Defect energies of graphite: Density-functional calculations. *Physical Review B* **72** (2005).

155 Zhong, J.-H. *et al.* Quantitative Correlation between Defect Density and Heterogeneous Electron Transfer Rate of Single Layer Graphene. *Journal of the American Chemical Society* **136**, 16609-16617 (2014).

156 Chae, S. J. *et al.* Synthesis of Large-Area Graphene Layers on Poly-Nickel Substrate by Chemical Vapor Deposition: Wrinkle Formation. *Advanced Materials* **21** (2009).

157 Li, Z., Cheng, Z., Wang, R., Li, Q. & Fang, Y. Spontaneous Formation of Nanostructures in Graphene. *Nano Letters* **9**, 3599-3602 (2009).

158 Benck, J. D., Hellstern, T. R., Kibsgaard, J., Chakthranont, P. & Jaramillo, T. F. Catalyzing the Hydrogen Evolution Reaction (HER) with Molybdenum Sulfide Nanomaterials. *Acs Catalysis* **4**, 3957-3971 (2014).

159 Benck, J. D., Chen, Z., Kuritzky, L. Y., Forman, A. J. & Jaramillo, T. F. Amorphous Molybdenum Sulfide Catalysts for Electrochemical Hydrogen Production: Insights into the Origin of their Catalytic Activity. *Acs Catalysis* **2**, 1916-1923 (2012).

160 Gopalakrishnan, D., Damien, D. & Shaijumon, M. M. MoS2 Quantum Dot-Interspersed Exfoliated MoS2 Nanosheets. *Acs Nano* **8**, 5297-5303 (2014).

161 Chang, K. *et al.* MoS2/Graphene Cocatalyst for Efficient Photocatalytic H-2 Evolution under Visible Light Irradiation. *Acs Nano* **8**, 7078-7087 (2014).

162 Kibsgaard, J., Jaramillo, T. F. & Besenbacher, F. Building an appropriate active-site motif into a hydrogen-evolution catalyst with thiomolybdate Mo3S13 (2-) clusters. *Nature Chemistry* **6**, 248-253 (2014).

163 Kibsgaard, J., Chen, Z., Reinecke, B. N. & Jaramillo, T. F. Engineering the surface structure of MoS2 to preferentially expose active edge sites for electrocatalysis. *Nature Materials* **11**, 963-969 (2012).

164 Eaton, P. & West, P. *Atomic force microscopy*. (Oxford University Press, 2010).

165 Materials, A. *Using Lorentz Contact Resonance to Determine the Viscoelastic Behaviour of Blended Polymers*, <https://www.azom.com/article.aspx?ArticleID=14047>

166 Lee, B., Prater, C. B. & King, W. P. Lorentz force actuation of a heated atomic force microscope cantilever. *Nanotechnology* **23**, 055709 (2012).

167 Bruker. *Electrostatic Force Microscopy – EFM*, <https://blog.brukerafmprobes.com/guide-to-spm-and-afm-modes/electrostatic-force-microscopy-efm/>

168 Watanabe, K., Taniguchi, T. & Kanda, H. Direct-bandgap properties and evidence for ultraviolet lasing of hexagonal boron nitride single crystal. *Nature materials* **3**, 404-409 (2004).

169 Cho, Y. J. *et al.* Hexagonal Boron Nitride Tunnel Barriers Grown on Graphite by High Temperature Molecular Beam Epitaxy. *Scientific Reports* **6** (2016).

170 Oliveira, C. K. *et al.* Crystal-oriented wrinkles with origami-type junctions in few-layer hexagonal boron nitride. *Nano Research* **8**, 1680-1688 (2015).

171 Paszkowicz, W., Pelka, J., Knapp, M., Kamler, G. & Podsiadlo, S. Thermal expansion of hexagonal boron nitride. *a [A]* **2**, 2.5055.

172 Yates, B., Overy, M. & Pirgon, O. The anisotropic thermal expansion of boron nitride: I. experimental results and their analysis. *Philosophical Magazine* **32**, 847-857 (1975).

173 White, G. Thermal expansion of reference materials: copper, silica and silicon. *Journal of Physics D: Applied Physics* **6**, 2070 (1973).

174 Jiang, T. *et al.* Valley and band structure engineering of folded MoS 2 bilayers. *Nature nanotechnology* **9**, 825 (2014).

175 Deng, S. & Berry, V. Wrinkled, rippled and crumpled graphene: an overview of formation mechanism, electronic properties, and applications. *Materials Today* **19**, 197-212 (2016).

176 Zhu, W. *et al.* Structure and electronic transport in graphene wrinkles. *Nano letters* **12**, 3431-3436 (2012).

177 Kim, E.-A. & Neto, A. C. Graphene as an electronic membrane. *EPL (Europhysics Letters)* **84**, 57007 (2008).

178 Musumeci, C. Advanced Scanning Probe Microscopy of Graphene and Other 2D Materials. *Crystals* **7**, 216 (2017).

179 Luo, S. *et al.* Formation of ripples in atomically thin MoS2 and local strain engineering of electrostatic properties. *Nanotechnology* **26**, 105705 (2015).

180 Long, F. *et al.* Characteristic work function variations of graphene line defects. *ACS Applied Materials & Interfaces* **8**, 18360-18366 (2016).

181 Filleter, T., Emtsev, K., Seyller, T. & Bennewitz, R. Local work function measurements of epitaxial graphene. *Applied Physics Letters* **93**, 133117 (2008).

182 Tosun, M. *et al.* MoS2 Heterojunctions by Thickness Modulation. *Scientific Reports* **5** (2015).

183 Wu, P. *et al.* Tailoring N‐Terminated Defective Edges of Porous Boron Nitride for Enhanced Aerobic Catalysis. *Small* **13**, 1701857 (2017).

184 Samaddar, S. *et al.* Equal variations of the Fermi level and work function in graphene at the nanoscale. *Nanoscale* **8**, 15162-15166 (2016).

185 Nicholl, R. J. T. *et al.* The effect of intrinsic crumpling on the mechanics of free-standing graphene. *Nature Communications* **6** (2015).

186 Lee, C., Wei, X., Kysar, J. W. & Hone, J. Measurement of the elastic properties and intrinsic strength of monolayer graphene. *science* **321**, 385-388 (2008).

187 Osváth, Z., Gergely-Fülöp, E., Deák, A., Hwang, C. & Biró, L. P. Mapping the nanomechanical properties of graphene suspended on silica nanoparticles. *Journal of Experimental Nanoscience* **11**, 1011-1018 (2016).

188 Zhou, X., Fu, J. & Li, F. Contact resonance force microscopy for nanomechanical characterization: accuracy and sensitivity. *Journal of Applied Physics* **114**, 064301 (2013).

189 Stan, G., King, S. W. & Cook, R. F. Nanoscale mapping of contact stiffness and damping by contact resonance atomic force microscopy. *Nanotechnology* **23** (2012).

190 Rosenberger, M. R., Chen, S. H., Prater, C. B. & King, W. P. Micromechanical contact stiffness devices and application for calibrating contact resonance atomic force microscopy. *Nanotechnology* **28** (2017).

191 Khanal, D. *et al.* Lorentz contact resonance spectroscopy for nanoscale characterisation of structural and mechanical properties of biological, dental and pharmaceutical materials. *Journal of Materials Science-Materials in Medicine* **26** (2015).

192 Fan, Y. C., Fang, T. H., Huang, C. C. & Chen, T. H. Atomic simulation of wrinkling and deformation in curved graphene nanoribbons under boundary confinement. *Materials & Design* **89**, 470-475 (2016).

193 Gan, C. K. & Liu, Y. Y. F. Direct calculation of the linear thermal expansion coefficients of MoS2 via symmetry-preserving deformations. *Physical Review B* **94** (2016).

194 El-Mahalawy, S. & Evans, B. The thermal expansion of 2H-MoS2, 2H-MoSe2 and 2H-WSe2 between 20 and 800° C. *Journal of Applied Crystallography* **9**, 403-406 (1976).

195 Castellanos-Gomez, A. *et al.* Local Strain Engineering in Atomically Thin MoS2. *Nano Letters* **13**, 5361-5366 (2013).

196 Kamatani, K. *et al.* Direct observation of catalytic oxidation of particulate matter using in situ TEM. *Scientific Reports* **5**, 10161 (2015).

197 Dazzi, A. *et al.* AFM–IR: combining atomic force microscopy and infrared spectroscopy for nanoscale chemical characterization. *Applied spectroscopy* **66**, 1365-1384 (2012).

198 Centrone, A. Infrared Imaging and Spectroscopy Beyond the Diffraction Limit. *Annual Review of Analytical Chemistry* **8**, 101-126 (2015).

199 Dazzi, A., Prazeres, R., Glotin, F. & Ortega, J. M. Analysis of nano-chemical mapping performed by an AFM-based (“AFMIR”) acousto-optic technique. *Ultramicroscopy* **107**, 1194-1200 (2007).

200 Geick, R., Perry, C. H. & Rupprecht, G. Normal Modes in Hexagonal Boron Nitride. *Physical Review* **146**, 543-547 (1966).

201 Dai, S. *et al.* Tunable Phonon Polaritons in Atomically Thin van der Waals Crystals of Boron Nitride. *Science* **343**, 1125-1129 (2014).

202 Caldwell, J. D. *et al.* Sub-diffractional volume-confined polaritons in the natural hyperbolic material hexagonal boron nitride. *Nature Communications* **5**, 5221(2014).

203 Kamat, P. V. Photophysical, photochemical and photocatalytic aspects of metal nanoparticles. *The Journal of Physical Chemistry B* **106**, 7729-7744 (2002).

204 Zielińska-Jurek, A., Wei, Z., Wysocka, I., Szweda, P. & Kowalska, E. The effect of nanoparticles size on photocatalytic and antimicrobial properties of Ag-Pt/TiO2 photocatalysts. *Applied Surface Science* **353**, 317-325 (2015).

205 Faure, B. *et al.* Dispersion and surface functionalization of oxide nanoparticles for transparent photocatalytic and UV-protecting coatings and sunscreens. *Science and Technology of Advanced Materials* (2016).

206 Winans, J. D., Hungerford, C., Shome, K., Rothberg, L. J. & Fauchet, P. M. Plasmonic effects in ultrathin amorphous silicon solar cells: performance improvements with Ag nanoparticles on the front, the back, and both. *Optics express* **23**, A92-A105 (2015).

207 Stratakis, E. & Kymakis, E. Nanoparticle-based plasmonic organic photovoltaic devices. *Materials Today* **16**, 133-146 (2013).

208 Ko, S.-J. *et al.* Highly efficient plasmonic organic optoelectronic devices based on a conducting polymer electrode incorporated with silver nanoparticles. *Energy & Environmental Science* **6**, 1949-1955 (2013).

209 Gamal-Eldeen, A. M. *et al.* Photothermal therapy mediated by gum Arabic-conjugated gold nanoparticles suppresses liver preneoplastic lesions in mice. *Journal of Photochemistry and Photobiology B: Biology* **163**, 47-56 (2016).

210 Banu, H. *et al.* Doxorubicin loaded polymeric gold nanoparticles targeted to human folate receptor upon laser photothermal therapy potentiates chemotherapy in breast cancer cell lines. *Journal of Photochemistry and Photobiology B: Biology* **149**, 116-128 (2015).

211 Polavarapu, L., Pérez-Juste, J., Xu, Q.-H. & Liz-Marzán, L. M. Optical sensing of biological, chemical and ionic species through aggregation of plasmonic nanoparticles. *Journal of Materials Chemistry C* **2**, 7460-7476 (2014).

212 Jain, P. K., El-Sayed, I. H. & El-Sayed, M. A. Au nanoparticles target cancer. *nano today* **2**, 18-29 (2007).

213 Chantharasupawong, P., Tetard, L. & Thomas, J. Coupling Enhancement and Giant Rabi-Splitting in Large Arrays of Tunable Plexcitonic Substrates. *The Journal of Physical Chemistry C* **118**, 23954-23962 (2014).

214 Schmid, S., Wu, K., Larsen, P. E., Rindzevicius, T. & Boisen, A. Low-Power Photothermal Probing of Single Plasmonic Nanostructures with Nanomechanical String Resonators. *Nano Letters* **14**, 2318-2321 (2014).

215 Govorov, A. O. & Richardson, H. H. Generating heat with metal nanoparticles. *Nano today* **2**, 30-38 (2007).

216 Qin, Z. & Bischof, J. C. Thermophysical and biological responses of gold nanoparticle laser heating. *Chemical Society Reviews* **41**, 1191-1217 (2012).

217 Gupta, A., Kane, R. S. & Borca-Tasciuc, D.-A. Local temperature measurement in the vicinity of electromagnetically heated magnetite and gold nanoparticles. *Journal of Applied Physics* **108**, 064901 (2010).

218 Jain, P. K., Lee, K. S., El-Sayed, I. H. & El-Sayed, M. A. Calculated absorption and scattering properties of gold nanoparticles of different size, shape, and composition:

applications in biological imaging and biomedicine. *The Journal of Physical Chemistry B* **110**, 7238-7248 (2006).

219 Setoura, K., Okada, Y. & Hashimoto, S. CW-laser-induced morphological changes of a single gold nanoparticle on glass: observation of surface evaporation. *Physical Chemistry Chemical Physics* **16**, 26938-26945 (2014).

220 Setoura, K., Werner, D. & Hashimoto, S. Optical scattering spectral thermometry and refractometry of a single gold nanoparticle under CW laser excitation. *The Journal of Physical Chemistry C* **116**, 15458-15466 (2012).

221 Nikiel, M. *et al.* Dynamics of thermally induced assembly of Au nanoislands from a thin Au layer on Ge(001). *CrystEngComm* **18**, 5674-5680 (2016).

222 Alonso-Gonzalez, P. *et al.* Real-space mapping of Fano interference in plasmonic metamolecules. *Nano letters* **11**, 3922-3926 (2011).

223 Lahiri, B., Holland, G., Aksyuk, V. & Centrone, A. Nanoscale Imaging of Plasmonic Hot Spots and Dark Modes with the Photothermal-Induced Resonance Technique. *Nano Letters* **13**, 3218-3224 (2013).

224 Jahng, J. *et al.* Ultrafast pump-probe force microscopy with nanoscale resolution. *Applied Physics Letters* **106**, 083113 (2015).

225 Nowak, D. *et al.* Nanoscale chemical imaging by photoinduced force microscopy. *Science Advances* **2** (2016).

226 Jahng, J. *et al.* Linear and Nonlinear Optical Spectroscopy at the Nanoscale with Photoinduced Force Microscopy. *Accounts of Chemical Research* **48**, 2671-2679 (2015).

227 Vitry, P. *et al.* Mode-synthesizing atomic force microscopy for 3D reconstruction of embedded low-density dielectric nanostructures. *Nano Research*, 1-7 (2015).

228 Rosa-Zeiser, A., Weilandt, E., Hild, S. & Marti, O. The simultaneous measurement of elastic, electrostatic and adhesive properties by scanning force microscopy: pulsed-force mode operation. *Measurement Science and Technology* **8**, 1333 (1997).

229 Keblinski, P., Cahill, D. G., Bodapati, A., Sullivan, C. R. & Taton, T. A. Limits of localized heating by electromagnetically excited nanoparticles. *J Appl Phys* **100**, 054305 (2006).

230 Hashimoto, S., Werner, D. & Uwada, T. Studies on the interaction of pulsed lasers with plasmonic gold nanoparticles toward light manipulation, heat management, and nanofabrication. *Journal of Photochemistry and Photobiology C: Photochemistry Reviews* **13**, 28-54 (2012).

231 Nanda, K. Size-dependent melting of nanoparticles: hundred years of thermodynamic model. *Pramana* **72**, 617-628 (2009).

232 Tetard, L., Passian, A., Farahi, R., Thundat, T. & Davison, B. H. Opto-nanomechanical spectroscopic material characterization. *Nature nanotechnology* (2015).

233 Garcia, R. & Herruzo, E. T. The emergence of multifrequency force microscopy. *Nature nanotechnology* **7**, 217 (2012).

234 Platz, D., Forchheimer, D., Tholén, E. A. & Haviland, D. B. Interpreting motion and force for narrow-band intermodulation atomic force microscopy. *Beilstein journal of nanotechnology* **4**, 45 (2013).

235 Binnig, G., Quate, C. F. & Gerber, C. Atomic force microscope. *Physical review letters* **56**, 930 (1986).

236 Jalili, N. & Laxminarayana, K. A review of atomic force microscopy imaging systems: application to molecular metrology and biological sciences. *Mechatronics* **14**, 907-945 (2004).

237 Zlatanova, J., Lindsay, S. M. & Leuba, S. H. Single molecule force spectroscopy in biology using the atomic force microscope. *Progress in biophysics and molecular biology* **74**, 37-61 (2000).

238 Krotil, H. U. *et al.* Pulsed force mode: a new method for the investigation of surface properties. *Surface and Interface Analysis* **27**, 336-340 (1999).

239 Shekhawat, G. S. & Dravid, V. P. Nanoscale imaging of buried structures via scanning near-field ultrasound holography. *Science* **310**, 89-92 (2005).

240 Tetard, L. *et al.* Elastic phase response of silica nanoparticles buried in soft matter. *Applied Physics Letters* **93**, 133113 (2008).

241 Vitry, P. *et al.* Mode-synthesizing atomic force microscopy for 3D reconstruction of embedded low-density dielectric nanostructures. *Nano Research* **8**, 2199-2205 (2015).